DISSERTATION | DOCTORAL THESIS

Titel | Title

Short-Term Metastabilities and Power Rating in Thin-Film Photovoltaic Technologies

verfasst von | submitted by

Ankit Mittal MSc

angestrebter akademischer Grad | in partial fulfilment of the requirements for the degree of

Doktor der Naturwissenschaften (Dr.rer.nat.)

Wien | Vienna, 2026

Studienkennzahl lt. Studienblatt | Degree programme code as it appears on the student record sheet:	UA 796 605 411
Dissertationsgebiet lt. Studienblatt | Field of study as it appears on the student record sheet:	Physik
Betreut von | Supervisor:	ao. Univ.-Prof. i.R. Dr. Wolfgang Lang Ass.-Prof. i. R. Dr. Viktor Schlosser

Ankit Mittal, MSc.
Short-Term Metastabilities and Power Rating in Thin-Film Photovoltaic Technologies
PhD Thesis, February, 2026
Supervisors: ao.Univ.Prof. Dr. Wolfgang Lang and Ass.Prof. Dr. Viktor Schlosser
Supervisor at AIT: Dr. Marcus Rennhofer

University of Vienna
Electronic Properties of Materials
Faculty of Physics
Boltzmanngasse 5
1090 Vienna

ABSTRACT

Thin-film photovoltaic technologies like amorphous silicon (a-Si:H), cadmium telluride (CdTe) , and $Cu_2ZnSn(S,Se)_4$ (CZTSSe) offer broad applicability. Although technologies are market-integrated, their performance is affected by effects such as short-term metastabilities. It is a charge-carrier and defect-driven, fully reversible state that causes a quasi-stable thermodynamic equilibrium triggered by external stimuli, such as light bias or temperature. This study investigated its impact on external electrical parameters and its correlation with existing international power stabilization protocols.

The research included tests on a-Si:H modules under illumination and thermal annealing. In a-Si:H, the electric parameter changes by metastability were around 3% in the maximum power P_{MPP} under illumination. Low-temperature annealing at $70\,^{\circ}\mathrm{C}$ increased the power by 17.2% by healing the dangling bonds of the a-Si:H material. The activation energies of the process were determined by Arrhenius law from annealing time constants and were found to range between 0.46 eV and 0.58 eV.

Field-aged CdTe modules used for low-light illumination exhibited a correlation between metastabilities and degradation rates, ranging from 4.62% to 22.11% below nominal power. P_{MPP} increased by up to 3.5%, then decreased with continued illumination, showing that a non-reversible material order-order relaxation superposed the reversible metastable effect. The metastable behavior broke down for degradation rates exceeding 22%. The findings demonstrated how sample history, prehandling modules, and preconditioning procedures affect the power measurement outputs.

In CZTSSe P_{MPP} showed a decrease of up to 9% during light soaking. A strong dependence on the light's spectral distribution (color) is observed, linking photon energy to defect activation. The material correlations between charge carrier concentrations between 6.50×10^{14} cm^{-3} and 1.01×10^{15} cm^{-3} could be correlated to the amplitude of metastable changes.

In conclusion, the investigations revealed that the degree of short-term metastable electric behavior is correlated with the level of initial degradation, defect density, illumination color, and operational bias. The findings highlight the need for preconditioning and controlled dark storage to ensure consistent and accurate PV characterization.

Zusammenfassung

Dünnschicht-Photovoltaiktechnologien wie amorphes Silizium (a-Si:H), Cadmiumtellurid (CdTe) und Kupfer-Zink-Zinn-Sulfid-Selenid (CZTSSe) bieten eine breite Anwendbarkeit. Obwohl diese Technologien bereits in den Markt integriert sind, wird ihre Leistung durch Effekte wie kurzzeitige Metastabilitäten beeinflusst. Diese stellen einen ladungsträger- und defektgetriebenen, vollständig reversiblen Zustand dar, ein quasistabiles, thermodynamisches Gleichgewicht, verursacht durch externe Einflüsse wie Licht- oder erhöhte Temperatur. In dieser Arbeit wurde der Einfluss auf die elektrischen Parameter sowie die Korrelation zu bestehenden internationalen Leistungsstabilisierungsprotokollen untersucht.

Die Untersuchungen umfassten Tests an (a-Si:H)-Modulen unter Beleuchtung und thermischer Ausheilung. Bei a-Si:H betrugen die durch Metastabilität induzierten Änderungen der elektrischen Parameter unter Beleuchtung etwa 3 % der maximalen abgegebenen Leistung P_{MPP}. Eine Tieftemperaturausheilung bei $70\,^{\circ}\mathrm{C}$ führte zu einer Leistungssteigerung von 17,2 % durch Heilung der a-Si:H-Dangling-Bonds. Die Aktivierungsenergien des Prozesses konnten mithilfe des Arrhenius-Gesetzes aus den Zeitkonstanten der Ausheilung bestimmt werden und diese lagen zwischen 0,46 eV und 0,58 eV.

Feldgealterte CdTe-Module, die unter schwacher Beleuchtung getestet wurden, zeigten eine Korrelation zwischen Metastabilitäten und Degradationsraten im Bereich von 4,62 % bis 22,11 % unterhalb der Nennleistung. P_{MPP} stieg zunächst um bis zu 3,5 %, fiel jedoch bei fortgesetzter Beleuchtung wieder ab, was auf eine nicht-reversible, Relaxation (Ordnungsübergang) im Material, überlagert mit dem reversiblen metastabilen Effekt, hinweist. Bei Degradationsraten über 22 % brach das metastabile Verhalten zusammen. Die Ergebnisse zeigen damit, wie Probenhistorie, Vorbehandlung und Pre-Conditioning die Messergebnisse beeinflussen können.

Bei CZTSSe wurde während der Beleuchtung ein Leistungsabfall von bis zu 9 % in P_{MPP} beobachtet. Es wurde eine starke Abhängigkeit vom Lichtspektrum (Farbe) festgestellt, was auf energiesensitive photonisch aktivierte Defekte hinweist. Die Korrelation zwischen den Ladungsträgerkonzentrationen von $6{,}50 \times 10^{14}$ cm^{-3} bis $1{,}01 \times 10^{15}$ cm^{-3} konnte mit der Amplitude der metastabilen Änderungen in Verbindung gebracht werden.

Zusammenfassend wurde gezeigt, dass die Amplitude des elektrisch kurzzeitigen metastabilen Verhaltens mit dem Grad der Anfangsdegradation, der Defektdichte, der Beleuchtungsfarbe und der Betriebsspannung korreliert ist. Die Ergebnisse unterstreichen die Notwendigkeit von Vorkonditionierung und kontrollierter Dunkellagerung zur Sicherstellung einer konsistenten und genauen Charakterisierung von Photovoltaikmodulen.

Acknowledgement

First and foremost, I would like to express my sincere gratitude to my supervisor, Dr. Marcus Rennhofer at the Austrian Institute of Technology (AIT), for his continuous support, valuable insights, and patient guidance throughout this thesis work. His encouragement and expert feedback have been instrumental in shaping both the content and direction of my research.

I am also deeply grateful to my professors, Dr. Wolfgang Lang and Dr. Viktor Schlosser, for providing a strong academic foundation and inspiring scientific curiosity through their teaching and mentorship. Their dedication and knowledge have contributed significantly to my academic development.

Furthermore, I wish to acknowledge the collaborative and stimulating environment at AIT, which provided me with the resources and motivation necessary to successfully complete this project.

Lastly, I would like to thank everyone—colleagues, friends, and family—who supported me, directly or indirectly, during the journey of this thesis.

[Ankit Mittal]
[February, 2026]

Contents

List of Figures

List of Tables

Nomenclature

α	Temperature coefficient for current
β	Temperature coefficient for Voltage
ϵ_0	Absolute permittivity
ϵ_r	Relative permittivity
μcSi	Microcrystalline silicon
σ	Electrical conductivity
τ	time constant
A	Amperes
a-Si:H	Hydrogenated amorphous silicon
A.M	Air mass
AC	Alternating current
C	Capacitance
C/cm^2	Capacitance/Area
CCD	charge coupled device
CdTe	Cadmium Telluride
CIGS	Copper Indium Gallium Sulphur (Selenium)
CZTS	Copper Zinc Tin Sulphur (Selenium)
DC	Direct current
DS	Dark storage
E_A	Activation energy
EQE	External quantum efficiency
eV	Electron-volt
FF	Fill factor
G	Irradiance

I_{SC}	Short circuit current
I_S	Reverse saturation current
IEC	International electrotechnical commission
k	Boltzmann constant
LS	Light soaking
n	Diode ideality factor
N(a)	Doping density
P_{MPP}	Maximum power point
PV	Photovoltaic
q	Electron charge
R_{SH}	Shunt resistance
R_S	Series resistance
STC	Standard test conditions
TCO	Transparent conductive oxide
V	Voltage
V_{bi}	Built-in voltage
V_{OC}	Open circuit Voltage
V_T	Thermal Voltage
W	Watts
W/m^2	Irradiance
Z	Impedance

Chapter 1

INTRODUCTION

> *The scientist is not a person who gives the right answers, he's one who asks the right questions.*
>
> **— Claude Lévi-Strauss**
> (French social anthropologist)

1.1 Current status of Photovoltaics

Nowadays the Photovoltaics (PV) market has been growing rapidly and slowly establishing its position in the global energy market [1]. The installation of 502 GW of photovoltaic energy was achieved globally at the end of 2023. Almost 109 GW of PV was installed globally in 2018, and the year-over-year growth is 17.5% predicted by Wood Mackenzie Power & Renewables. Bloomberg's NEF (New Energy Finance) predicts an expected installation of 131.9 GW by the end of 2019 [2]. Combined, the existing solar power (utility and small-scale) worldwide stands at a whopping 635 GW, as stated by Solar Power Europe. According to the adoption of the COP21 Paris Agreement to be fulfilled by 2050, a section in Article 2 states: "...holding of the global average temperature to well below 2 °C above the preindustrial levels and to pursue efforts to increase the temperature to 1.5 °C above preindustrial levels to reduce the impacts of climate change significantly." Pollution and global warming are strong drivers for renewable technologies in the market. The excessive use of fossil fuels has become the bottleneck in controlling climate change. Due to record-low prices of 0.059$ per kWh, this sector has many positive prospects. The main buyers of the photovoltaic market are the United States, China, Japan, Germany, and India, according to their investment plan in solar installation [3]. The prices of solar systems are continually decreasing, which is a positive sign for the adoption of solar energy. Since the first solar cell was used to deploy the Vanguard 1 satellite in Earth's orbit in 1958, there has been massive growth in PV technology. After applying PV technology in space, it sparked interest in making it more efficient and affordable for the commercial sector. It took a few decades for PV prices to drop to a level that enabled their terrestrial use and market penetration. PV has become a vital energy commodity in some countries, allowing them to meet the daily energy needs of their consumers. The ever-growing advances in various PV technologies are illustrated in terms of efficiency in the NREL chart, with a closer look at thin-film solar cells in Figure 1.1.

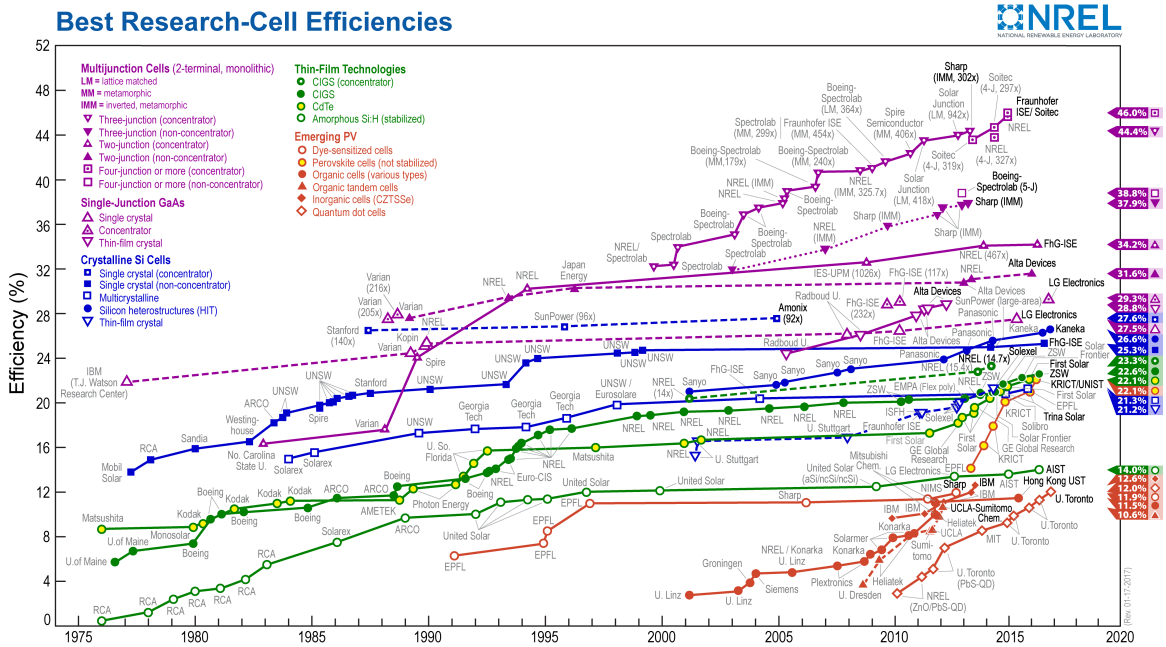

(a) NREL solar cells efficiency chart: "This plot is courtesy of the National Renewable Energy Laboratory, Golden, CO"

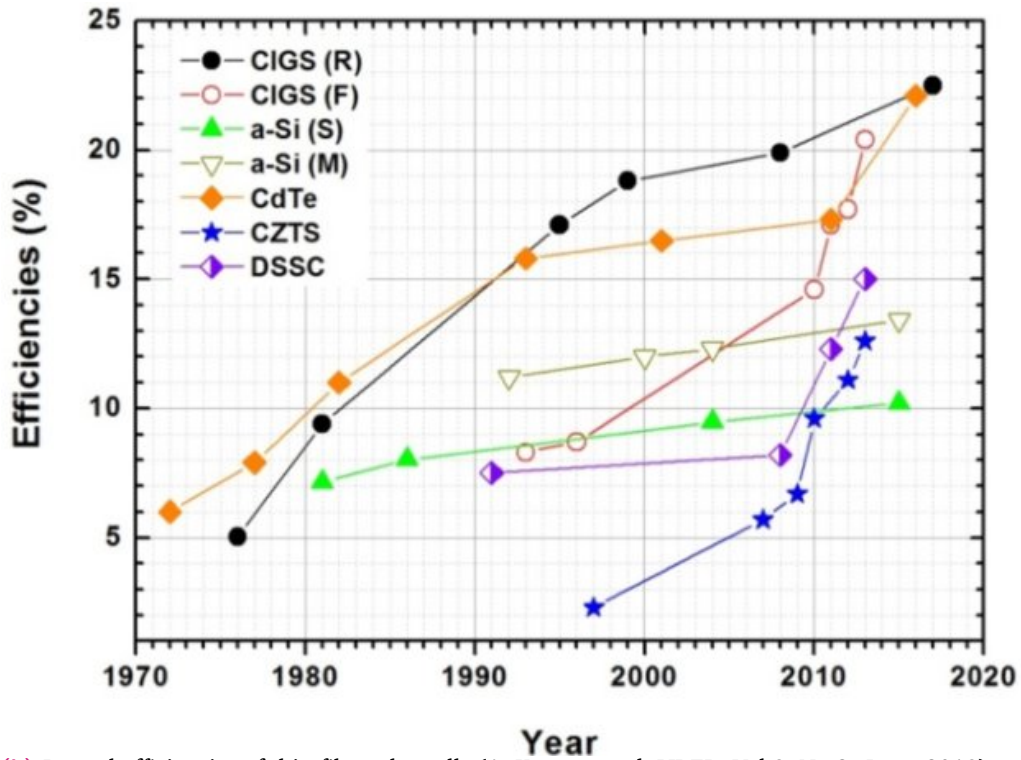

(b) Record efficiencies of thin-film solar cells (A. Kowsar et al.,IJRER, Vol.9, No.2, June, 2019)

Fig. 1.1: Evolution of various solar cell technologies

To meet the demand for electricity through primary energy sources like PV, it is necessary to have a strategic plan for the PV technology roadmap. Garcia of Sandia National Laboratories said: 'A technology roadmap is a plan that matches short-term and long-term goals with specific technology solutions to help meet those goals.' [4]. A roadmap of PV technology requires favorable control to promote market growth, observe changing market trends, and have realistic milestones to ensure progress in a certain time frame. The Technology Readiness Level (TRL) is a tool that plays a crucial role in assessing the maturity of technology during its development stages. Without TRL, bringing emerging technologies into the market is impossible.

Thin-film PV technology began its commercial journey with amorphous silicon (a-Si:H), but its demand remained low due to its relatively low efficiency compared to crystalline silicon technology. The central part of the PV installation consists of polycrystalline and monocrystalline solar cells, based on silicon wafer technology. However, because of limited production and complex manufacturing process, some competitive new thin-film PV technologies are dictating their growth position in the market. They are sought after due to their competitive pricing compared to crystalline silicon technology. The good thing about using thin films is that they perform well in diffuse and low-light conditions, in contrast to crystalline silicon technology. The majority of existing commercial thin-film PV consists of a-Si:H, cadmium telluride (CdTe), and copper indium gallium diselenide disulfide (CIGS). Photovoltaic technologies, such as CIGS and CdTe, have already established a foothold in the market, positioning them as potential competitors to crystalline silicon technology. Figure 1.2 shows a pie chart to provide a view of the market share of individual thin-film technologies.

The Si wafer-based solar cells have a thickness of a few hundred microns. In contrast, thin-film PV technology has cells with thicknesses ranging from hundreds of nanometers to a few microns. The thin-film PV sector has been on the market since the 1980s and has witnessed considerable advancement in manufacturing techniques and material usage. According to the new report by GBI Research, "Thin-Film Photovoltaics (PV) Cells Market Analysis to 2020," the presence of the thin-film solar PV market globally has grown from a mere 14 MW in 2001 to 2.14 GW in 2009, accounting for the compounded annual growth rate of 58% from 2001 to 2009. It is projected to grow at a rate of 2.8% from 2001 to reach 22.21 GW by 2020. This was due to sudden inflation in the price of polysilicon, resulting from a supply shortage between 2006 and 2009. Before then, the thin-film market was dominated by a-Si:H, but this sudden shortage of polysilicon led to other higher conversion efficiency, enabling thin-film technologies to enter the demanding market. Although the share in thin-film PV production was only 6% in 2016, the CAPEX increased by more than 1 billion US$ in the next 2-3 years. Despite the low price of PV and the enhancements in scalability and mass production, crystalline silicon technology maintained dominance due to its higher efficiency, faster technological

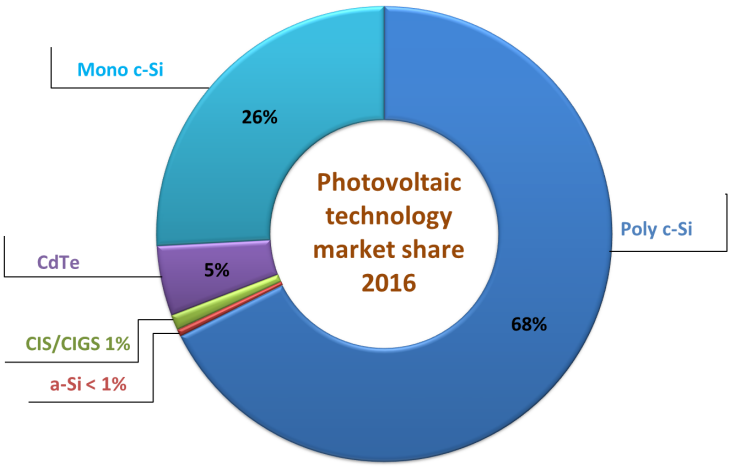

(a) Market share in 2016

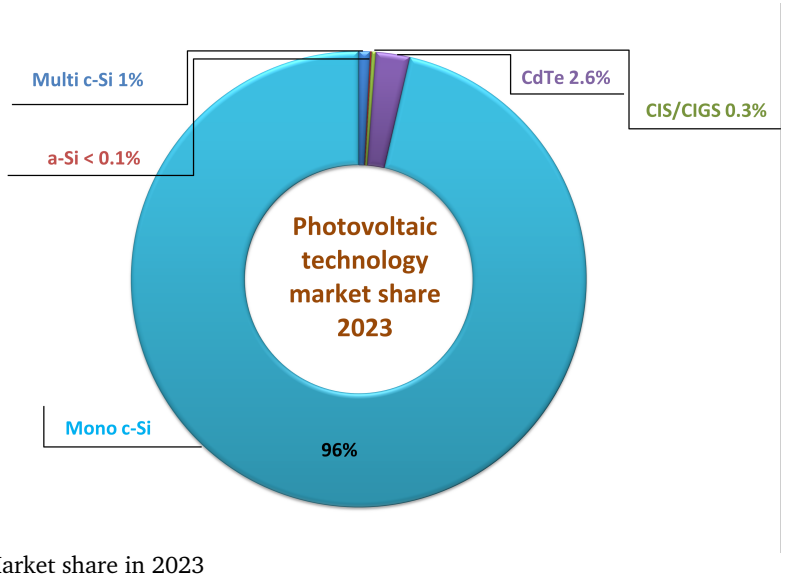

(b) Market share in 2023

Fig. 1.2: Market share of different PV technologies in 2016 and 2023

advancements, and higher research investments. In 2023, the size of the thin film PV market was greater than 5.1 billion US$, but the total share of the PV market has decreased by 3%.

CdTe modules became the face of thin-film technology on a global scale. A significant boost in the industry was achieved through First Solar, a manufacturer of CdTe technology, with the construction of a 550 MW power plant in Arizona, which increased demand for thin-film technology. Recent growing concerns about the presence of the toxic element cadmium and the use of rare earth tellurium are causing concern about maintaining its growth in the future. CIGS technology now fills this gap. Due to its relatively simple manufacturing and flexibility, it has significant potential to replace silicon-based technologies. CIGS is already competing

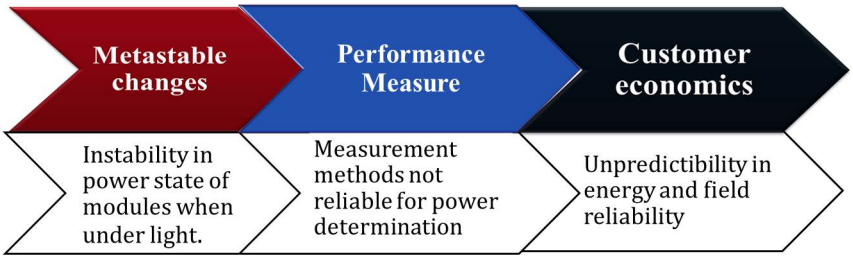

Fig. 1.3: Impact metastabilities on the thin-film PV market

with silicon technology in terms of efficiency and manufacturing costs, making it the most attractive thin-film technology.

1.2 Thin-film PV Metastabilities

Thin-film PV is advancing its share in the global market but still lacks reliability in power output. This is due to uncertainty in power delivery resulting from their inherent metastabilities, which can be induced by illumination or voltage bias. These metastabilities are causing inconvenience and financial loss to manufacturers and investors in PV power plants, as shown in Figure 1.3. When power ratings are performed on thin films inside a pulsed-sun simulator, several factors can affect the resulting measurement, including metastabilities, transient effects, the use of crystalline reference cells, and current matching in a tandem cell. Temperature stability is a primary concern in terms of power rating. Otherwise, it can result in the introduction of various metastable effects, which are then difficult to rule out. In many thin-film devices, reversible changes in fill factor and V_{OC} have been observed, which occur during light soaking or voltage biasing.

Metastability generally refers to changes in the arrangement and bonding of atoms and defects inside semiconductors, leading to deviations in the electronic properties. Metastability in material occurs when it leaves its original ground state (state of least energy) and becomes a partially stable state, in contrast to the actual ground state. Metastable effects are correlated to lattice relaxations caused by intrinsic defects such as vacancies, interstitials, or complexes. They exist in two configurations, acceptor and donor, where each can have a multivalent character. The defects allow for the trapping of charge carriers in donor and acceptor configurations. An example of amorphous silicon can be explained by the defect generation that occurs when the Si-H bond is broken, resulting in the recombination of charge carriers.

$$\mathrm{Si-H} \longleftrightarrow \mathrm{Si_{dangling\ bond}} + \mathrm{H} \tag{1.1}$$

Thin-film photovoltaic materials are known to show metastabilities as a result of their trapping mechanisms for the generated charge carriers. The major thin-film

technologies available on the market and emerging thin-film technologies show metastabilities.

A clear understanding of the mechanism in thin-film PV devices is still lacking with regard to their inherent defect behavior and light-induced metastabilities. In most thin-film PV technologies, these metastable effects are reversible when an external trigger is applied, such as a change in temperature or a considerable relaxation time in the dark. In general terms, two types of metastabilities are observed in thin-film PV: **long-term** and **short-term** metastable effects. In a-Si:H, long-term metastabilities occur during outdoor operation, particularly when subjected to prolonged illumination periods. Still, when annealed at $160\,^{\circ}\mathrm{C}$, it reaches its low defect density in a few minutes. This metastability is triggered by the light, which leads to the creation of light-induced defects. The photoconductivity also decreased due to the trapping and recombination of charge carriers. Some effects of metastabilities in a-Si:H are given as:

- Increase in the activation energy: Metastable defects increase the energy required for charge-carrier activation.
- Decrease in charge carrier lifetime: Recombination processes, induced by defect creation, reduce the lifetime of charge carriers and lower the minority carrier diffusion length.
- Reduction in dark conductivity: Defects limit charge transport in the absence of illumination.
- Time-Dependent performance degradation: Over prolonged periods of operation, the metastabilities cause seasonal and time-dependent performance degradation.

During the laboratory operation of thin-film PV technology, extreme care is generally taken to measure these devices because of their inherent metastable behavior. Many reforms have already been made in the IEC standard community; this makes it an area of intensive research because of ambiguity in the measurement routines. Even the more commercial-based technologies like CIGS and CdTe are still suffering from the inadequacy of inaccurate power measurement.

1.2.1 Correlation of Metastabilities

In technologies based on chalcogenide (CdTe), chalcopyrite (CIGS), and kesterite (CZTSSe), metastabilities have been observed. Metastabilities result in similar electrical properties, which depend solely on the type of defect formation within the material structure or the material's quality. Even solar cells of the same technology have been observed to exhibit completely different behavior under similar conditions because of the varying quality of the samples.

1.3 Thesis Structure

This thesis is systematically structured as follows.

- Chapter 1 presents an overview of the current status of photovoltaics (PV) and provides insights into thin-film technology, including its key electrical characteristics.
- Chapter 2 covers the theoretical principles underlying PV and thin-film technologies, the primary methods employed in this work, and existing standards for reliable power measurement.
- Chapter 3 describes the equipment used and discusses potential sources of measurement errors.
- Chapter 4 details the experimental procedures.
- Chapter 5 presents the experimental results, while Chapter 6 analyzes and discusses these findings in depth.
- Finally, Chapter 7 concludes the thesis and highlights key takeaways.

Chapter 2

THEORY

> *Everything is theoretically impossible, until it is done.*
>
> **— Robert A. Heinlein**
> (Science fiction writer)

2.1 Investigating thin-film technologies

Solar cell is a semiconductor device based on the principle of the photovoltaic effect, which converts photons into electricity. However, to achieve this, a p-n junction or, in some cases, a p-i-n junction must be formed between two semiconductors. To fully understand a solar cell's functionality, it is also essential to understand the photoelectric effect, which was proposed by Albert Einstein in 1904 to show that the electron behaves differently to each wavelength of light, where light consists of packets of energy called quanta, and only a certain amount of energy is accepted by the electrons from the available photons to gain enough energy to be emitted. The photocurrent density is measured at incident spectra, where the probability of each photon generating an electron in the external circuit is referred to as the quantum efficiency of solar cells. Note that the quantum efficiency of solar cells depends upon the device structure, formation environment, different materials, material quality, deposition methods, absorption rate of the photons, charge separation, charge extraction, etc. In this study, several thin-film devices with different architectures were studied. The thin-film PV is generally monolithically integrated, resulting in all cells being successively connected in series, as shown in Figure 2.1.

The samples used for the metastability investigation were double-junction or single-junction PV devices. The samples ranged from commercially available PV modules to laboratory-deposited PV cells. Table 2.1 shows the PV technologies investigated in this work at the cell and module levels.

The cells in a-Si:H modules were double junctions with a p-i-n structure, as shown in figure 2.2 (a). This i-layer facilitates carrier transport, as explained in Section 2.7. Micromorph technology is also a tandem cell technology, in which a-Si:H serves as the top cell and microcrystalline silicon is the bottom cell. The other technologies CIGS, CdTe, and CZTS were all single junction technologies, and their architecture is shown in figure 2.2 (b).

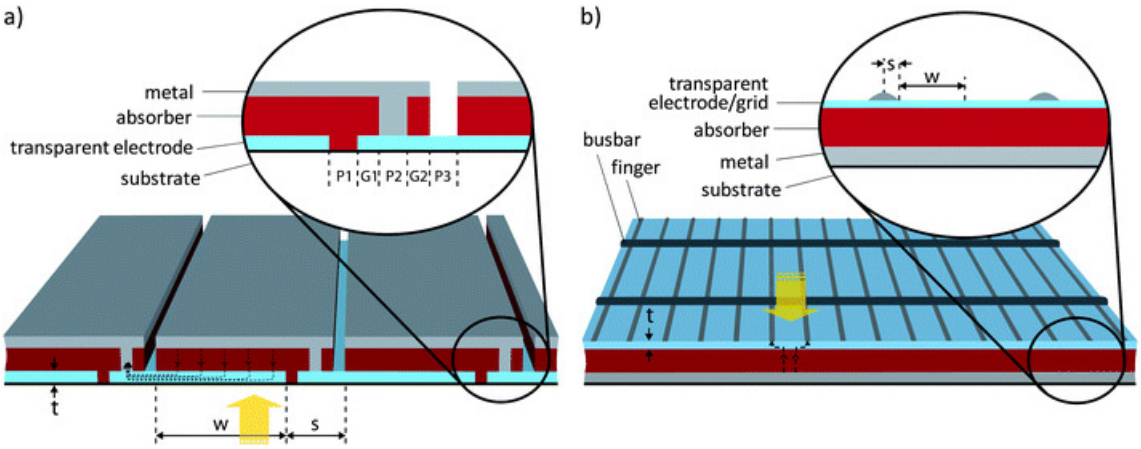

Fig. 2.1: [Comparison between an a-Si module vs c-Si cells (a) shows an integrated series of connected a-Si cells, whereas in case (b) is a single cell of c-Si which has to be externally assembled to the final module. (Rowell M. W., McGehee M. D., Transparent electrode requirements for thin film solar cell modules. Energy Environ. Sci., 4(1), 131–134 (2011).)

Sample	Technology Type	Experiments
Modules	a-Si:H CdTe Micromorph CZTS	Pretreatment Annealing Stabilization
Cells	CZTS CIGS	Pretreatment Impedance spectroscopy

Tab. 2.1: Thin-film PV technologies researched upon in this work

The solar cells can be deposited in either substrate- or superstrate-based configurations, shown in figure 2.3. In a superstrate-based configuration, light enters through the glass substrate. Some solar cells are deposited in a substrate configuration, where cells are deposited from back to front, like in CIGS. In this case, the back contact, which is typically made of Mo (Molybdenum), does not need to be transparent, as the light enters through the transparent conductive oxide layer.

2.2 Theory of solar cells

A solar cell is a current-generating device, whereas a battery is a voltage-generating device. The output current of a solar cell depends directly on the incident light to which it is exposed, whereas the voltage is logarithmically dependent. For a solar cell to operate, electrons and holes are separated by a built-in electrical potential. These so-called semi-permeable membranes, consisting of n- and p-type semiconductors, have high conductivity for one type of charge carrier and low conductivity for the other [2]. In general, when solar cells are exposed to light, the photons deliver their energy to the electrons, resulting in electron-hole pairs. These excited charge

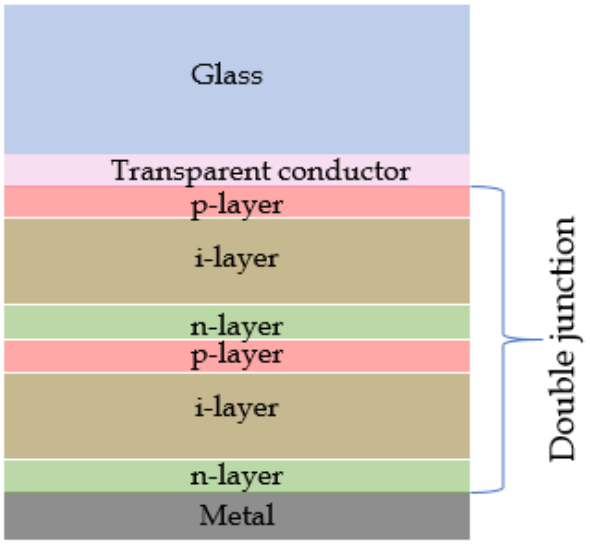

(a) Schematic diagram of a-Si:H double junction solar cell in a superstrate configuration

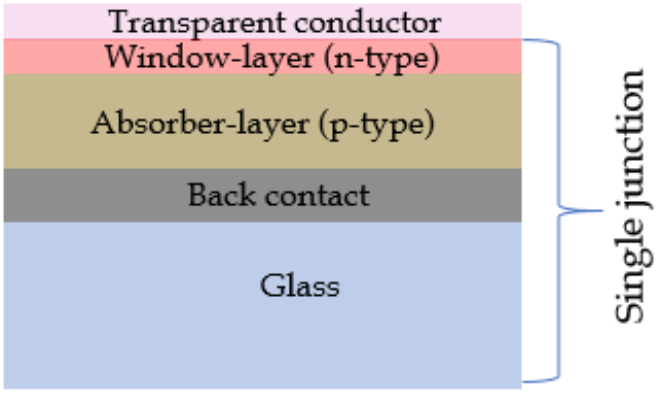

(b) Schematic diagram of single-junction thin-film solar cell architecture in a substrate configuration.

Fig. 2.2: Architecture of thin-film solar cells technologies.

carriers wander randomly until directionality is given through metal contacts, and they are extracted. Sometimes, when the solar cell is removed from the light and stored in the dark, in principle, the cell should reach its equilibrium state through the recombination mechanism, involving electrons and holes.

When atoms are in their nascent state, they have electrons occupied in specific orbits, where the electrons in the outermost orbit are referred to as in valence state. The valence state has electrons that are occupied in the orbitals. When the atoms come close together, the interaction between the electrons splits the valence state into bonding and antibonding levels. The bonding level is at the lower energy state filled with electrons, referred to as the valence band, and the antibonding

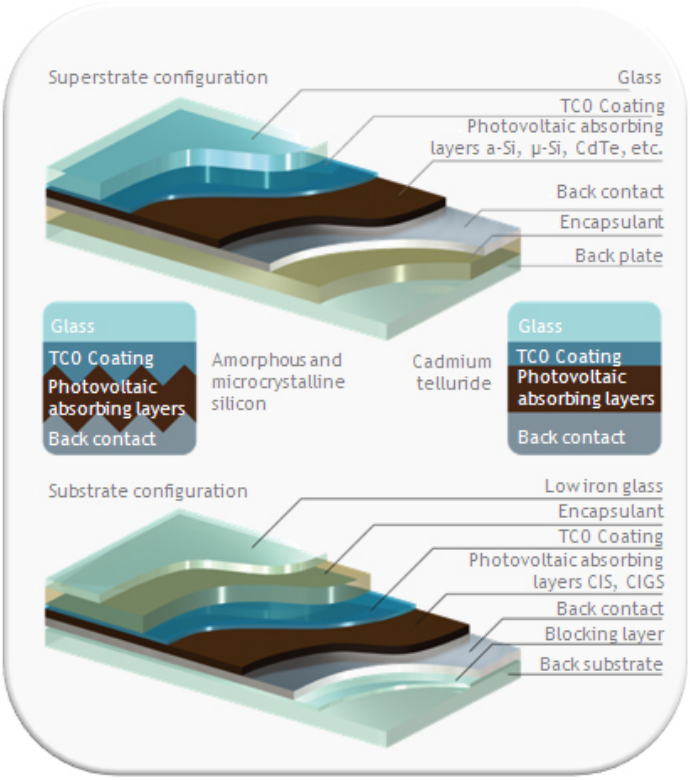

Fig. 2.3: Different configurations of thin-film solar cells (`https://www.pilkington.com/en/global/knowledge-base/types-of-glass/solar-energy/solar-technologies/thin-film-photovoltaics`)

level is at a higher energy state with lower electron occupancy, referred to as the conduction band. Metals, insulators, and semiconductors all consist of a valence band and a conduction band. Metals, or conductors, are solids that have a partially filled conduction band, resulting in high electrical conductivity. Insulators have a large bandgap of more than 4 eV, making it difficult for conductivity to occur. The semiconductor bandgap lies between those of metals and insulators.

When photons interact with the semiconductor material over a broad range of energies, they excite the electrons to higher-energy states. These may collide with the semiconductor atoms and transfer excess energy, a process known as phonon interaction. Therefore, the electrons are relaxed near the edge of the conduction band. The same thing happens in the valence band, where the excited electrons leave behind holes that are then filled up by the electrons that are still higher up in the valence band, causing the holes to accumulate near the valence band edge. These processes are called thermalization, which populates the band edges with electrons and holes, respectively. The electrons that settle at the edge of the conduction band cannot remain there for long and instead jump back to the valence band to recombine with the holes. This is correlated with the exponentially decreasing density of charge carriers n as one moves away from the band edges

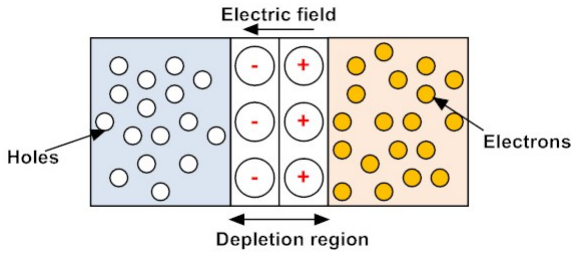

Fig. 2.4: Depiction of formation of a p-n junction

$$n \propto e^{-E/kT}, \tag{2.1}$$

where E is the energy, k the Boltzmann constant, and T the temperature. The time to recombination is on the order of nanoseconds, a sufficient amount of time to utilize the electrons for extractable power by connecting the solar cell to the external circuit.

For a solar cell to operate the following conditions should be fulfilled: photons transfer energy to the carriers, charge carriers are moved from a low energy state to a high energy state, a metal contact is used to collect the charge carriers, and after the external circuit dissipates energy, carriers return to the second contact to start the process of charge flow again. This makes it ideal for use as a photovoltaic (PV) device. Likewise, a good working solar cell needs to balance voltage formation and current flow. Therefore, the choice of semiconductor material required for appreciable voltage generation and high charge extraction is crucial. A larger bandgap results in higher voltage and lower current, whereas a lower bandgap results in higher current and lower voltage. The voltage is formed because of the splitting of the Fermi energy, which is then referred to as the quasi-Fermi energy under external voltage bias or photon absorption. This results in an increase in the energy of the electrons in the n region and the holes in the p region, leading to a potential difference between the two contacts.

An electron-rich semiconductor material (n-type) and a hole-rich material (p-type) are joined together through a metallurgical/chemical process, forming a p-n junction to construct a solar cell. This junction is known as the space-charge region, where the electrons and holes from either side diffuse to form positive ions at the n-side and negative ions at the p-side. When charges are neutralized, this voltage is called the built-in voltage, V_{bi}. This generates an electric field, which helps transport the charge carriers. The open-circuit voltage (V_{OC}) is the maximum available voltage that the solar cell delivers when the current is zero. In general, it cannot exceed V_{bi} because the band bending at the junction will cause the photogenerated charge carriers to move in the opposite direction.

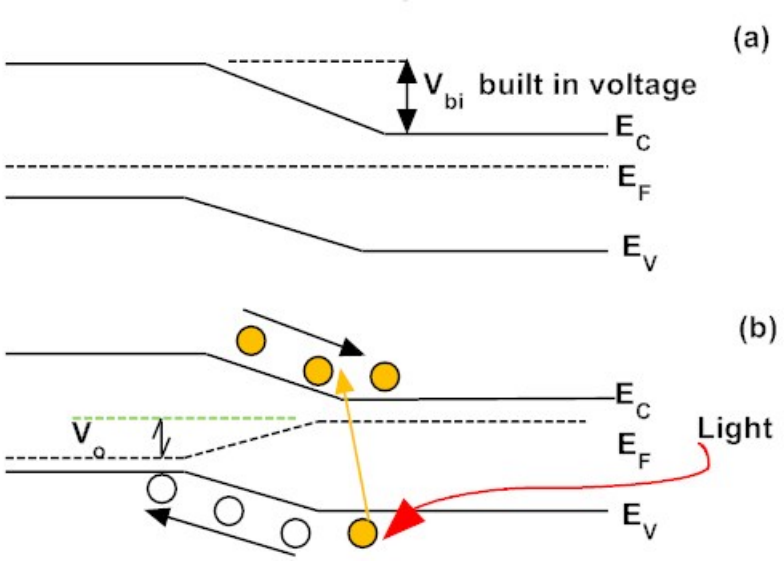

Fig. 2.5: Fermi level (a) when the solar cell is under dark (b) when the solar cell is irradiated by the light showing splitting of the fermi levels.

Two selective electron and hole contacts are required to transport the charge carriers in a PV cell, which carries the excited and relaxed carriers. Since electrons from the n-side and holes from the p-side are the dominant carriers, metal contacts matching the Fermi energy of the free carriers make them available to the external circuit. To collect the charge carriers, their diffusion length should be greater than the thickness of the absorber. In the dark, solar cells do not deliver any voltage or energy; however, when exposed to light, they split the Fermi level at the p-n junction. When light enters the n region, it causes an increase in the energy of the electrons. Hence, their Fermi energy also increases. When recombination is considered, the minority charge carriers are the factor that limits the recombination. The density of carriers decreases exponentially by the Boltzmann factor when away from the edges of the band [5].

It is undesirable when the electronic properties of the materials change due to some defect sites. The defects vary according to the material's structure and properties. Many pairs of atoms form defect compounds that act as trapping or recombination sites, hindering the movement of the charge carriers. Generally, many defect states lie inside the bandgap, termed deep states, which can cause the trapping of the charge carrier when traveling from conduction to valence band or vice versa. This can result in reduced or increased power and fill factor.

2.2.1 Solar Cell Geometry

A typical solar cell design consists of a metal electrode back-contact, an absorber layer (generally a p-type), a window layer (n-type), and a transparent conductive oxide (TCO) as a top contact. Both the metal electrode and the TCO are useful

for charge transport. In amorphous silicon (a-Si:H) it is generally a p-i-n-based configuration, where i stands for the intrinsic layer, rather than the conventional p-n-based devices. Because the mobility of electrons is better than the mobility of holes, it is usual to keep room for carriers with higher mobility (electrons) to travel wider and carriers with lower mobility (holes) to travel shorter in a semiconductor. The intrinsic layer of a-Si:H serves two purposes: first, to provide a strong electric field to accelerate the charge carriers, and second, to provide enough charge carriers.

2.2.2 Solar cell parameters

When characterizing solar cells, a simple circuit analysis is used to determine the parameters, which include a p-n junction diode with shunt and series resistances. A diode equation explains the mechanism of current generation in a solar cell. Generally, the photocurrent is referred to as the short-circuit current, which is added to the dark current. This photogenerated current is opposite in sign to the dark current of a diode. The short circuit current is mainly affected by irradiance and temperature as external factors, but the internal factors can be several, such as manufacturing defects, shunt resistances or material defects, as for example, trapping or recombination through defects [6, 7, 8]. The short-circuit current is dominated by the generated charge carriers, which are within the limit of the diffusion length of the junction, resulting in a large charge collection.

Equation of a solar cell assuming the one-diode model:

$$I = I_{\text{ph}} - I_{\text{s}} \left[\exp(\frac{qV}{nkT}) - 1 \right]. \tag{2.2}$$

The model is composed of two terms: (1) I_{ph} accounting for the light-generated (and considered to be a voltage-independent constant) current, and (2) the exponential diode equation (without series and shunt resistance) as a loss mechanism. In the diode equation, I_{s} is the saturation current, n is the ideality factor, and k is the Boltzmann constant. The Fermi energy is closer to the valence band in a p-type semiconductor and closer to the conduction band in an n-type semiconductor.

Open circuit voltage at I=0:

$$V_{\text{OC}} = \frac{nkT}{q} \ln \left(\frac{I_{\text{ph}}}{I_{\text{s}}} + 1 \right) \tag{2.3}$$

The fill factor is an important parameter of a solar cell in terms of how it differs from its behavior from an ideal characteristic. It is a measure to quantify the quality of a junction and the series resistance of the cell that affects the open-circuit voltage. In simplified terms, the fill factor is seen as the squareness of the I–V curve, which is defined as the ratio of P_{MPP} to the product of I_{SC} and V_{OC}

$$FF = \frac{V_{\text{MPP}}.I_{\text{MPP}}}{I_{\text{SC}}.V_{\text{OC}}}. \tag{2.4}$$

Parasitic resistances are one of the leading causes of the loss of fill factor, as the shunt and series resistances affect the squareness of an I–V curve from its threshold point. When the series resistance becomes very high and the shunt resistance becomes very low, they affect I_{SC} and V_{OC}, respectively.

There is also an important parameter often mentioned for comparing different PV technologies: their conversion efficiency. The conversion efficiency is defined as the maximum power output over the incident light intensity and the total surface area.

Parasitic Resistance

All parasitic resistances cause a reduction in fill factor and efficiency. They are classified into two categories: series resistance (R_S) and shunt resistance (R_{SH}), depending on the geometry and material quality of a solar cell.

The series resistance (R_S) originates mainly from the bulk of the semiconductor material. The shunt resistance (R_{SH}) is due to the manufacturing impurities and imperfections in solar cells.

The series resistance is contributed by metallic contacts, bulk resistance of the semiconductor, movement of current through the junction, and contact resistance between the metal contact and semiconductor material. It decreases the voltage that arrives at the external terminals. The short circuit current is generally not affected by the series resistance, as it is not very large (< 10 ohms).

The shunt resistance is the result of manufacturing defects or precipitation of foreign impurities that cause many local sites to pass the current directly. This causes the current from the cell to surge through a localized area or around the edge of the cell. Such diversion can lead to a reduction in voltage from the solar cell. An equivalent diagram of the solar cell that indicates the series and shunt resistance is shown in figure 2.6.

Temperature

A PV device is sensitive to temperature change, which can affect electrical and electronic properties. An increase in temperature causes the current to increase and the voltage to decrease. The elevation of temperature reduces the bandgap, which decreases the voltage. This, in turn, increases the energy of the charge carriers; however, due to phonon interaction, recombination increases, resulting in a slight increase in I_{SC}.

Irradiance

Varying light intensity can significantly impact the performance of a PV device. Several performance parameters are affected by it, like efficiency, open circuit

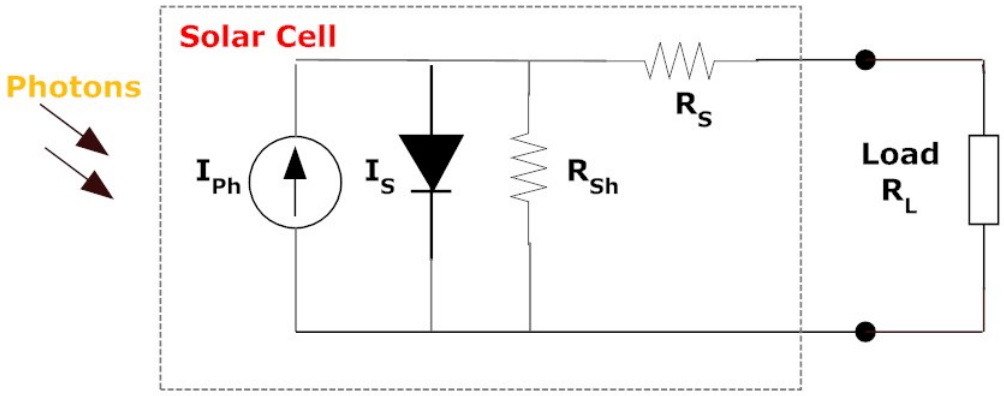

Fig. 2.6: A one-diode equivalent circuit of a PV device showing its series and shunt resistances

voltage, fill factor, short circuit current, etc., due to the impact of parasitic resistances. Under low-light conditions, the influence of shunt resistance becomes significant. Therefore, a PV device with a high shunt resistance could lead to a higher power retention compared to a solar cell with a low shunt resistance.

Ideality factor

The ideality factor describes the proximity of a PV device to the ideal diode. Ideality factors define the part of the curve that is most relevant to the operation of a PV device.

2.2.3 I–V curve characteristics

Some important parameters of a solar cell or module are measured while acquiring their current-voltage characteristics. Generally, a PV device is measured through a voltage sweep, where the voltage is ramped linearly, and the resulting current is measured. During measurement, 0 volts [V] gives the short-circuit current, and 0 amperes [A] gives the open-circuit voltage. There is an operating point in a solar cell where maximum power can be extracted; it is the product of voltage and current at the maximum power point. Different I–V characteristics can be obtained in light or dark conditions, depending on the parameter of interest. A typical I–V curve is shown in fig. 2.7.

In a typical solar cell, there is a formation of the p-n junction that results in the photovoltaic effect, and when connected to a load, this results in a current flow. The quasi-Fermi energy levels split to build the voltage at the p-n junction [9]. If we were to use only one kind of semiconductor, like n or p-type, we could not transport electrons and holes because of its symmetry. Like in the case of an n-type semiconductor, the Fermi energy at the surface merges into a single Fermi

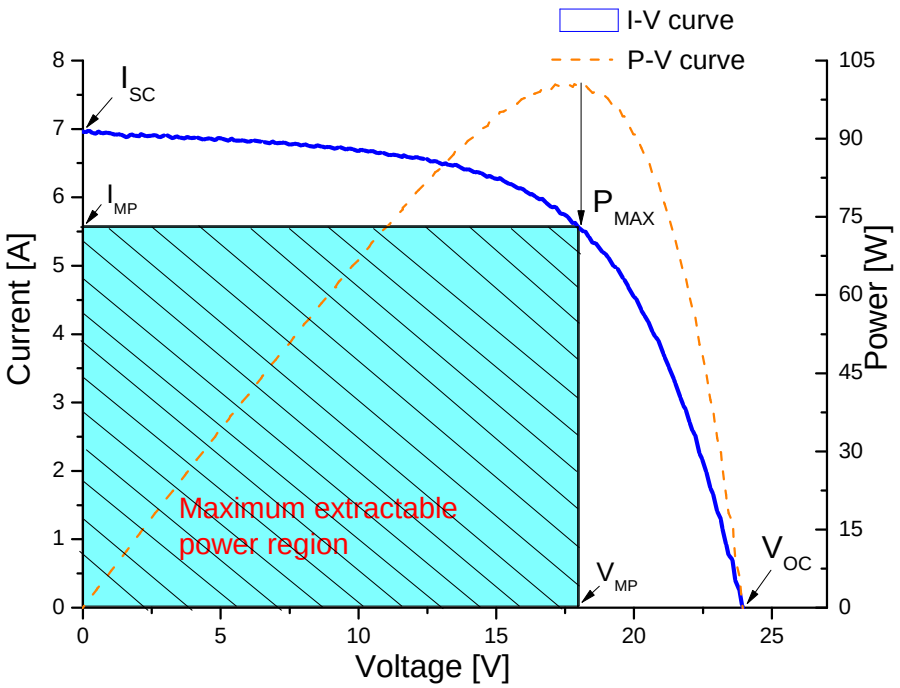

Fig. 2.7: An I–V curve of a typical PV module

energy. Although this results in a Fermi energy gradient, it directs the electrons and holes towards the surface where they recombine. In addition, the concentrations of electrons and holes are the same on the right and left surfaces, which leads to no voltage formation. In the p-n junction, the quasi-Fermi levels are at different positions because of the different carrier concentrations on the left and right sides of the surface.

2.3 Two Diode Model

The series resistance R_S gives the measure of internal losses due to the presence of internal resistances of the cell and the interconnections that affect current flow and cause voltage drops. The shunt resistance R_{Sh} measures the leakage current when the diode is negatively biased or at low voltages.

If we need to consider the recombination effect in a PV device with defects, then it is necessary to use the two-diode model instead of the one-diode model. The two-diode model takes into account a second diode that complements the Shockley-Read-Hall recombination. It works at low temperatures and irradiances, thus giving more accurate results and curve characteristics.

The two-diode model is a lumped circuit that separates the diffusion and recombination current in the PV device. The equivalent circuit is shown in Fig. 2.8.

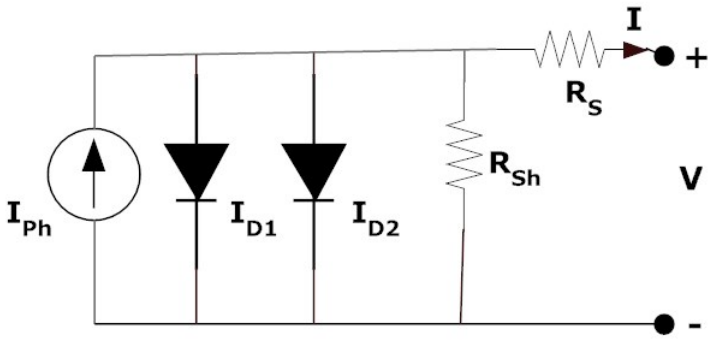

Fig. 2.8: A two-diode model equivalent circuit diagram.

Mathematically, the two-diode model is represented as [10]:

$$I(V) = I_{Ph} - I_{D1}\left(\exp\frac{V+IR_S}{n_1 V_T} - 1\right) - I_{D2}\left(\exp\frac{V+IR_S}{n_2 V_T} - 1\right) - \frac{V+IR_S}{R_{Sh}}, \quad (2.5)$$

where I_{ph} is the photocurrent, I_{D1} is the reverse saturation current of the first diode, I_{D2} is the reverse saturation current of the second diode, n_1 and n_2 are the ideality factors of the diodes, V_T is the thermal voltage, R_S is the series resistance, R_{Sh} is the shunt resistance, and V is the terminal voltage.

The current losses of the PV device are divided into two diodes (the losses reduce the light-generated photocurrent I_{ph}), where the first diode's saturation current I_{D1} represents the diffusion current and the second diode's saturation current I_{D2} represents the current through the recombination mechanism; mainly through traps known as Shockley-Read-Hall recombination. The n_1 is generally kept at 1 according to the classical p-n junction theory [11, 5]. The second diode's ideality factor n_2 value should be 2 from recombination using trap theory [12], but it can be higher for cells with defects and lower for high-quality samples [13]. The thermal voltage $V_T = kT/q$, where q is the electric charge. The recombination mechanism because of defects causes the charge carriers to recombine before they reach the external terminal.

2.4 Preconditioning and Power Rating

Light soaking was a treatment introduced as a *preconditioning* procedure on the PV technology to ensure its stability before conducting an I–V characterization for power rating. However, the light-soaking procedure worked well for crystalline silicon technology, as it did not have any defect-driven trapping states. This could lead to a short-term change in the electrical parameter [14].

Every commercial PV technology must be rated for its deliverable power because it is important to measure the power delivered by a power source such as a PV module or PV cell. All commercial PV modules have a nameplate capacity written as the nominal electric power, which is determined by varying a resistive load from open-circuit conditions to short-circuit conditions, from zero current generation to the maximum current generation. The maximum power lies somewhere in between this region of open circuit and short circuit. Accurate information on power from PV technology helps determine the installation capacity in terms of power or forecast the energy yield for the coming year, as well as identify the power loss with each operating year.

The IEC committee has certain procedures and guidelines to follow when measuring commercial PV technology before installing a PV facility. The measurement in the lab is conducted through a solar simulator at Standard Test Conditions (STC), which are specified for crystalline and thin-film technology in the standards like IEC 61215, and IEC 61646; specifically, the power provided by the sun per unit area, known as the solar intensity, is 1000 W/m^2, with a spectrum similar to sun spectra hitting the Earth's surface at latitude 35 °N in the summer (air-mass 1.5), and the temperature of the device at 25 °C. However, in reality, the solar intensity varies drastically due to clouds and haze and when the radiation from the sun has to travel a longer path through the atmosphere. In each PV device, the higher the absorption of photons, the greater the short-circuit current will be.

2.4.1 IEC standards on testing photovoltaic solar cells

The IEC (International Electrotechnical Commission) is a committee concerned with the standardization of electrical and electronic fields. The field of PV issues various standards and guidelines for performing accurate measurements on PV devices such as crystalline silicon modules and thin-film modules.

A block diagram in Figure 2.9 shows the IEC standards followed during the measurement routine.

- IEC 60891: Photovoltaic devices - Procedures for temperature and irradiance corrections to measured I–V characteristics
- IEC 60904-1: Photovoltaic devices – Part 1: Measurements of PV current–voltage characteristics
- IEC 61646: This is an old standard that was designed to fulfill special but common testing requirements for all thin-film PV modules.
- IEC 61215-1-x: This standard is designed to fulfill special testing requirements for technology-specific PV modules.

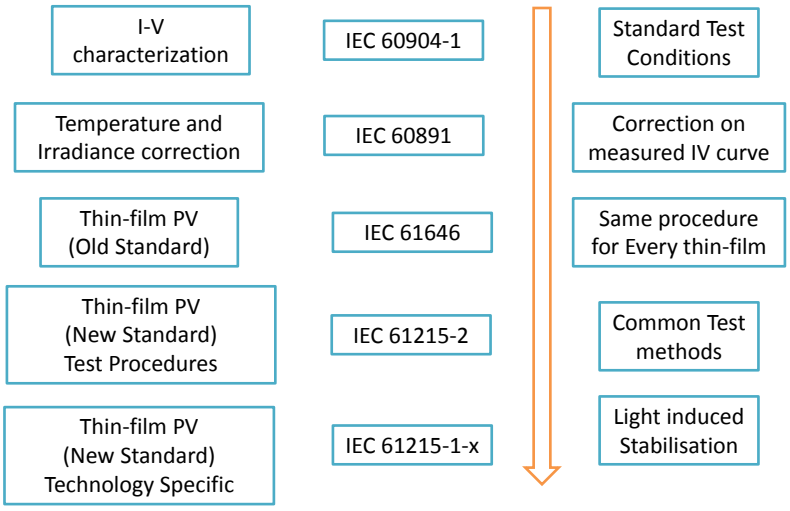

Fig. 2.9: Representation of IEC standards followed during the measurement routine for the thin-film PV technologies

- IEC 61215-2: This standard is meant for the design qualification and type approval of terrestrial photovoltaic modules to test their electrical and thermal characteristics.

2.5 Capacitance–Voltage Measurements

Capacitance techniques monitor the movement of electronic charges within a semiconductor device, providing a measure of free-carrier and electrically active defect-state properties. Capacitance is the charge storage capacity and is measured across a capacitor or rectifying junction. In the simplest case of homogeneously distributed shallow doping, the doping concentration defines the width of the depletion region of the p-n-junction. In this situation, the thin film solar cell is equivalent to a plate capacitor of area A (cell area), with a plate distance of W (extension depletion region), and causes a capacitance [12]. It can store a charge with the applied voltage. When an AC voltage is applied, the small signal capacitance changes. In reverse polarity, a voltage increase widens the depletion region.

The capacitance of a solar cell has three different contributions:

1. The junction capacitance, which represents the charge storage in the depletion layer of the p-n junction, and dominates in reverse and low forward bias conditions,

2. the diffusion capacitance, which corresponds to the minority carrier storage in the quasi-neutral regions of the junction, is important in forward bias,
3. the transient carrier capacitance, which is influenced by the existence of defects and interface states[15].

The last two contributions depend exponentially on the applied voltage. This allows combining these two into the free carrier capacitance. The diffusion capacitance is mainly responsible for the measurement artifacts described in this section. The diffusion capacitance has the following dependence on the applied voltage V [16]:

$$C_{\text{diff}} = C_0 \exp(bkT/qV), \tag{2.6}$$

where C_0 and b are constants. Typical values for the total capacitance of a high-efficiency solar cell vary from 30 to 100 μF/cm^2 and are 100 times higher than for conventional solar cells.

C–V measurement: defects respond differently to the signals at high frequencies to low frequencies. At high frequencies, only shallow states can respond because for deep-state defects, the frequency is too high to see any observable effect. Only at low frequencies can defects respond, and a clear increase in the capacitance along with the free carrier density can be observed.

$$N(\text{total}) = N(\text{carrierdensity}) + N(\text{defects}). \tag{2.7}$$

C–V measurements can be made either forward-biased or reverse-biased. However, when the cell is forward biased, the applied DC voltage must be limited; otherwise, the conductance may be too high for the capacitance meter to measure. It determines the concentration of majority carriers in the bulk of the device, as well as the energy levels of the interface states (or both) that often exist between the surfaces of different materials [17]. The C–V measurement captures the oscillating charges in the space-charge region at the right frequency. If it is too low, then the traps can interfere with the data, and if it is too large, rather than plotting dC/dV, it is sometimes desirable to view the data as 1/C^2 vs voltage because some parameters are related to the 1/C^2 data. For example, the doping density (N) can be derived from the slope of this curve because N is related to the capacitance by:

$$N(a) = \frac{2}{\epsilon_0 \epsilon_r A^2 [d(1/C^2)/dV]}, \tag{2.8}$$

where: N(a) = the doping density (1/cm^3), q = the electron charge (1.60219 $\times$ 10^{-19} C), ϵ_0 = absolute permittivity (8.854 $\times$ 10^{-14} F/cm, ϵ_r = semiconductor permittivity, (11.7 for silicon), A = area (cm^2), C = the area-normalized capacitance (F/cm^2), and V = applied DC voltage. Equation (2.8) applies only to the depletion capacitance observed under reverse bias voltages (and assuming a pn-junction rather

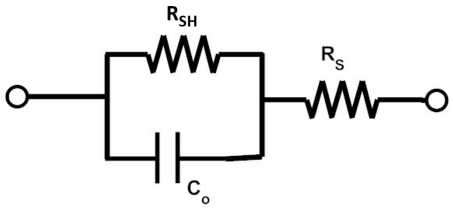

Fig. 2.10: Representation of impedance present in a solar cell in terms of an equivalent circuit.

than a pin-junction). The built-in voltage of the cell junction can be derived from the intersection of the $1/C^2$ curve and the horizontal axis. This plot should be a fairly straight line.

2.6 Impedance Spectroscopy

Impedance spectroscopy is used to analyze the measured AC response of a solar cell, utilizing resistances and capacitances in an equivalent circuit. It is a useful technique to distinguish between the processes occurring in solar cells over several decades of frequency. These effects include series resistance, recombination resistance, depletion, and junction capacitance, which are passive elements in a circuit that can be represented. In the Nyquist plot, the arc present at low frequencies reflects the effect of the recombination mechanism at low bias voltages. As the bias voltage increases, the influence becomes less pronounced.

Through impedance spectroscopy, we can distinguish the effects from different regions in the solar cell, such as the bulk, contacts, and heterojunction interface, based on their distinct time constants. The AC equivalent of a p-n heterojunction contains three elements, R_S (series resistance), R_{SH} (parallel resistance), and C_0 (sum of diffusion and depletion capacitance). The bulk and contacts generally contribute to the series resistance, while recombination in the depletion region contributes to the parallel resistance.

Charge storage is represented by capacitors, which is a reversible process. Resistances represent interfacial charge transfer, transport, and recombination, and are primarily irreversible processes. The complex impedance is given by

Imaginary part: $Z' = R_s + \frac{R_{SH}}{1+\omega^2 {C_0}^2 {R_{SH}}^2}$; real part: : $Z'' = \frac{\omega C_p {R_{SH}}^2}{1+\omega^2 {C_0}^2 {R_{SH}}^2}$.

The equivalent circuit has a single time constant $R_{SH}C_0$, therefore, the semicircle in the Nyquist plot shows the predominance of a single time constant. The series resistance R_S to the capacitor is determined from the minimum Z_0 value at the highest frequency. The Z_0 value at the lowest frequency represents the sum of the series resistance and the parallel resistance (R_S + R_{SH}) to the capacitance.

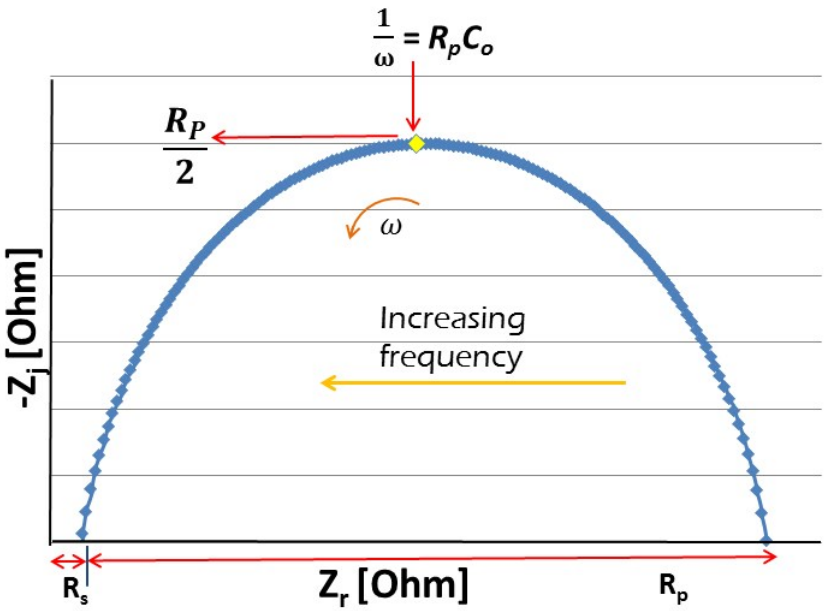

Fig. 2.11: Representation of impedance as the Nyquist plot and the basic information to be extracted from the graphical representation

When a reverse bias is applied to the solar cell, the depletion width increases and the capacitance decreases. It is given by the expression where the width of the depletion layer is proportional to the square root of the reverse bias voltage

$$C_{\mathrm{j}} = \frac{\epsilon_0 \epsilon_r}{W}. \tag{2.9}$$

At forward bias, the junction capacitance increases as a result of an increase in diffusion current until the electrostatic barrier is reduced to zero at the junction. After surpassing the electrostatic barrier under forward bias, the conduction mechanism changes from diffusion to drift, and the drift current becomes dominant, resulting in a decrease in capacitance.

$$Z = Z^{'} + iZ^{"} = R + iX, \tag{2.10}$$

where Z is the impedance and Z' and R are the real part (resistance) and Z" and X the imaginary part (reactance).

The analysis of the impedance is an important technique for evaluating AC circuits. The resistance is plotted along the real axis, and the reactance, stemming from capacitors and inductors, is plotted on the imaginary axis. Equation (2.10) represents the complex impedance in Cartesian format. The equations are used in their polar form to determine the impedance of the combination of RC circuits

$$V(t) = V_m \, e^{i(\omega t + \phi_v)}, \tag{2.11}$$

$$I(t) = I_m \, e^{i(\omega t + \phi_i)}, \tag{2.12}$$

$$Z = \frac{V(t)}{I(t)} = \frac{V_m \, e^{i(\omega t + \phi_v)}}{I_m \, e^{i(\omega t + \phi_i)}} = \frac{V_m}{I_m} e^{i\phi} = |Z| \, e^{i\phi}, \tag{2.13}$$

$$Z = |Z| \cos\phi + i \, |Z| \sin\phi. \tag{2.14}$$

2.7 Amorphous Silicon

One technology that is considered to be the birth of thin-film technology is amorphous silicon technology. A-Si research was started by Carlson and Wronski in 1976 at the RCA laboratory. This particular technology has made an immense change in the thin-film industry. After many decades of research, the microscopic structure of a-Si:H and its defects remain unclear. It has paved the way for the introduction of new thin-film technologies such as tandem solar cells consisting of microcrystalline, amorphous silicon, and HIT (heterojunction with intrinsic thin-layer) solar cells. A-Si:H has a continuous random structure, where a localized silicon lattice is considered to define the band structure. It has a wide band gap of 1.75 eV and behaves as a direct bandgap material during photon absorption. With a direct bandgap, a-Si:H has a high absorption coefficient to ensure only a few microns of material are good enough to reach high absorption, in contrast to crystalline silicon. The latter has an indirect bandgap and a low absorption coefficient, requiring 200 times more material to absorb photons above the bandgap.

In amorphous silicon, the alternative bonding configurations give rise to electronically induced metastable states. Still, in CIGS, CdTe, and CZTS different tertiary or secondary compound formations cause the electronically induced metastable states. Producing amorphous silicon is one of the most environmentally friendly techniques, since the by-products generated are environmentally benign. However, unfortunately, it is not mass-produced due to its low efficiency which hinders its growth in the market.

The main characteristics of a-Si (unhydrogenated amorphous silicon) are uncoordinated atoms and broken bonds, which are called dangling bonds. During its deposition, hydrogen is introduced, which passivates the dangling bonds in a-Si:H, thereby further reducing the defect density by several orders of magnitude and improving its electronic properties. The hydrogen density composition in a-Si depends on the manufacturing process used. Almost any impurity can be introduced into

this open structure, leading to unsuitable semiconducting behavior. A-Si:H solar cells were found to exhibit a loss in efficiency over several hundred hours under light exposure and then reach a steady state. A decline in efficiency shows a loss in conductivity and an increase in the defect density of a-Si:H. This particular effect is called the Staebler-Wronski effect [7,8]. It is a self-limiting effect, but when the material is heated to over 160 °C, it reverses its original efficiency.

Fig. 2.12: Structure of (a) hydrogenated amorphous silicon and (b) crystalline silicon.

The dangling bonds also act as non-radiative recombination centers for charge carriers, known as deep states. The energy separation between the conduction and valence bands has exponential distributions, which cause the formation of tail states, which are localized in nature.

Although defects in amorphous silicon are reduced after hydrogenation, it does not rule them out completely from affecting device performance. With a-Si:H, one can reach a high open-circuit voltage, but the short-circuit current is low. It has a high amount of midgap electronic states that originate from the formation of dangling bonds inside.

In the cell configuration the intrinsic layer i has to be as thick as possible for the maximum absorption of photon flux. Also, it cannot be thicker than the depletion width otherwise a reduction in charge collection would occur. The density of states in a-Si:H has an exponential distribution in valence and conduction bands. A representative diagram for the density of states in the a-Si:H is shown in figure 2.10.

The hydrogen percentage in a-Si is measured by FTIR spectroscopy. The peak for the presence of Si:H is useful in determining the concentration of hydrogen in the amorphous silicon film.

For a-Si:H technology, a short-term metastable effect is also observed, which can lead to deviations in the electrical performance of the thin-film modules [9]. Similar behavior has already been reported for other thin film devices [10-12]. As a result, exposure to low illumination levels prior to power rating can introduce a systematic

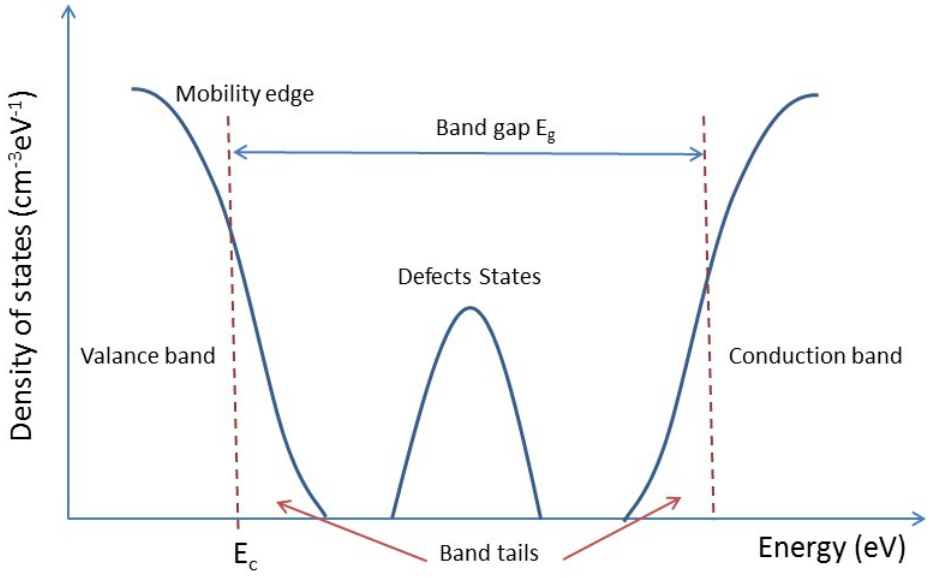

Fig. 2.13: Energy states in a-Si.

error in the accuracy of standard power rating procedures as defined in the former IEC standard 61646, which is now IEC 61215-1-3 [13-15].

The activation energy is described by the fact that the magnitude of the current is proportional to the number of charge carriers able to overcome the energy barrier E_a, and also the thermal energy of the charge carriers that follow the Boltzmann factor.

Metastability occurs in a-Si:H through external excitation, such as irradiance, current bias, energetic particles, etc., which induce defects in the continuous random structure of a-Si:H. These defects can be annealed by applying a temperature treatment at 160-180 °C, reaching a state of thermal equilibrium, also synonymous with the equilibrium of the defects. A tandem cell configuration of amorphous silicon and microcrystalline solar cells is called a micromorph structure. The structure of microcrystalline silicon has a higher crystallinity than that of a-Si:H.

2.7.1 Defect models

During the determination of the loss in photoconductivity under the illumination of a-Si:H, many defect models were proposed to understand the formation of new defects inside the a-Si:H.

Bond Breaking Model

The earliest model to explain metastabilities in a-Si was the 'weak Si-Si bond breaking model' proposed by Stutzmann in 1985. When a weak Si-Si bond is adjacent to the Si-H bond, it is broken by the hole trapping, resulting in a dangling bond and switching

Fig. 2.14: Cross section of an a-Si cell.

of the Si-H bond, leading to a non-radiative electron and hole recombination. The creation of dangling bonds is given by the following equation:

$$\frac{dN_{\mathrm{d}}}{dt} = C_{\mathrm{SW}} A_{\mathrm{t}} np, \tag{2.15}$$

where C_{SW} is dangling bond creation efficiency, A_t is the recombination rate, and n and p are the electron and hole density, respectively. The relation between the density of the dangling bonds N_d, the illumination time, and the generation rate was theoretically deduced, and found to be in good agreement with the experimental results; $N_d \propto G^{2/3}\ t^{1/3}$.

Hydrogen related bond breaking model

This model was proposed by Godet in 1998 and was based on the experimental fact that the density of light-induced dangling bonds is proportional to the density of Si-H bonds. Dangling bond creation was explained by the interaction of two Si-H bonds, which led to a transformation of a metastable Si-H-Si bonding state. This state interacts with either the Si-H bond to create a dangling bond or a Si-Db (silicon with a dangling bond) to reduce it to a stable state.

Hydrogen-collision model

This model was proposed by Branz in 1999 and in 2003 an extended version of this model was published. The hydrogen atom dissociates from a Si-H bond by releasing energy from the nonradiative recombination of an electron and a hole. This disassociated hydrogen atom will interact with a Si-Si bond to form two Si-H bonds, resulting in two separate dangling bonds. These two hydrogen-dangling-bond complexes interact with each other to annihilate the metastable hydrogen atoms.

Hydrogen-mediated model

The hydrogen-mediated model was proposed by Zafar and Schiff in 1989. In this model, the hydrogen is transferred between the clustered and dilute phases of bonded hydrogen to form silicon-dangling bonds.

2.7.2 Amorphous silicon cell

Silane-based (SiH_4 gas) glow discharge induced by RF voltages, or plasma-enhanced chemical vapor deposition, are the commonly used methods to deposit a-Si:H. The

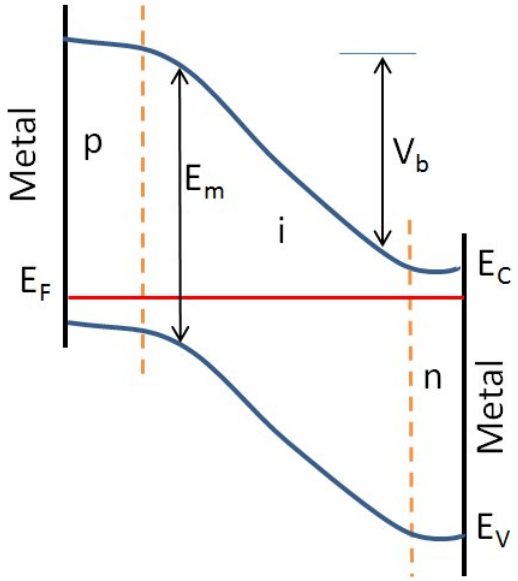

Fig. 2.15: Graphical representation of the energy bands in an a-Si cell.

substrate temperature should be around 150-300 °C to ensure hydrogen incorporation into the a-Si:H material. Lower temperatures lead to worse film quality; on the other hand, higher temperatures lead to less incorporation of hydrogen, thereby increasing the number of dangling bonds. The superstrate type is the most common deposition scheme used to prepare a-Si:H cells. It consists of a TCO (Transparent conductive oxide) as front contact over a transparent glass substrate. Different layers of semiconductors (p-i-n structure) are then deposited onto the TCO. The textured layer of the TCO helps in light trapping. A schematic diagram of the a-Si:H p-i-n-based solar cell is shown in figure 2.14 .

Over the window glass plate, a thin layer of around 50 nm silicon dioxide is applied, followed by the TCO layer. Suitable materials for TCO is ITO and ZnO:Al. Texturization of the TCO layers helps in light trapping. Over the TCO a thin p-type layer (Boron doped) of a-Si:H layer is deposited. It is alloyed with carbon to minimize the absorption in this layer. A boron-doped a-SiC:H layer is deposited over the p-layer, acting as a buffer layer. It serves as a diffusion barrier between the p and i layers. An intrinsic layer of a-Si:H followed by an n-layer is deposited over the buffer layer. Finally, a metallic contact is placed on top.

The band diagram of the a-Si:H cell is shown in figure 2.15. The p-i-n cell configuration facilitates charge collection through the drift mechanism, rather than the conventional diffusion mechanism. In an a-Si:H cell, the p and n layers establish the junction, i.e., they provide a built-in voltage and have to be as thin as possible since they do not contribute to charge collection. When the light is absorbed in the i-layer, pairs of electrons and holes are generated, separated by the electric field through a

drift mechanism where holes reach the p-layer and electrons reach the n-layer. The metallic contacts on either side of the device extract the charge carriers.

Table 2.2 shows the samples used for the a-Si:H technology during the experiments. Please note that the samples mentioned here were selected from a larger batch of modules used previously in both indoor and outdoor experiments.

Tab. 2.2: Sample modules for the pre-treatment experiment; S1, S5, S6, S7 are all a-Si:H technology and S9 belongs to the micromorph technology.

Samples	State of operation	Stabilization
Sample S1	Outdoor	Preconditioned indoors
Sample S5	Outdoor	Preconditioned indoors
Sample S6	Outdoor	Preconditioned indoors
Sample S7	Outdoor	preconditioned indoors
Sample S9	Indoor	Unstabilized

2.7.3 Light-Induced defects

Defects greatly influence the electronic properties of the a-Si:H. First, different charge states within the bandgap are of great interest because they act as charge-trapping and recombination sites. Second, the electronic states differ due to the bonding and atomic structure of the defect. Third, the effect of the defect reaction on growth is important.

To explain the defect mechanism, one must first understand how recombination occurs in the solar cell when an electron and a hole are combined immediately after being created through a photon carrying sufficient energy. Recombinations are of two types: radiative and nonradiative. Nonradiative recombination results in an electron-phonon interaction to supply a defect reaction.

The density of dangling bonds increases over a prolonged period of illumination. The defect density N_d is proportional to the power of 0.6 of the illumination (G) and the cube root of the time (t) of exposure. The defect rate is proportional to the nonradiative recombination rate. Under the thermal process, the activation energy of a-Si:H is approximately 1 eV, which is correlated with hydrogen movement. The external illumination provides energy to overcome this thermal barrier, resulting in the extraction of energy from a nonradiative recombination process. When the energy from recombination exceeds the energy of the thermal process, defects are formed, causing the system to deviate from its initial equilibrium state.

The equilibrium density of the defect is:

$$N_{\mathrm{d}} = N_{\mathrm{d0}} \exp(\Delta E_{\mathrm{F}}/kT), \tag{2.16}$$

where ΔE_F is the shift in Fermi energy and N_{D0} is the density of the neutral defects.

The illumination increases defects in the i-layer and p-i interface of a-Si:H technology. This increase in defects saturates after long exposure to irradiance.

2.8 Cadmium Telluride

Cadmium Telluride solar cells have an ideal bandgap of 1.45 eV, which ensures high solar energy conversion to deliver high efficiency. So far, CdTe solar cells have reached only up to 20 % efficiency because of the difficulty in creating good ohmic contacts for the stability of solar cells. Additionally, the formation of many secondary and tertiary compounds leads to defect centers in the bandgap, resulting in the creation of a metastable state.

Since its introduction as a PV device in 1972 by Bonnet and Rabenhorst, CdTe technology has experienced a significant boost in the present thin-film sector. There are several defects associated with the CdTe technology. It has been a long way to reach high efficiency and compete with existing silicon technologies. CdTe and CdS react to form an interfacial layer of $CdS_{1-x}Te_x$ [1]. CdTe cells are deposited with the highest quality through the closed-spaced sublimation (CSS) process. The configuration is as a heterojunction with the most widely preferred window layer, cadmium sulfide (CdS). The presence of a barrier at the back contact reduces FF.

The dominant thin-film photovoltaic materials, namely CdTe, CIGS and a-Si, exhibit transient performance changes upon exposure to light [1,2,3]. The operation of CdTe technology in forward bias was shown to reduce the degradation of V_{OC} and P_{MPP} that occurs with illumination [5]. Still, after dark storage, more degradation was observed than before the application of bias on the modules. Although there is a similarity in the observed behavior between biased and light-exposed modules, it was not possible to establish the equivalence of bias to light exposure using a repetitive measurement routine.

Cadmium telluride (CdTe) is an established thin film technology that continues to demonstrate its edge in high efficiency and flexibility in the manufacturing process [18]. As millions of modules of this type of technology are installed outdoors, it makes this one of the most promising technologies for achieving climate control goals. CdTe has a direct bandgap of 1.45 eV and a chalcogenide structure suitable for optimal photovoltaic (PV) conversion [19, 20]. Due to its high optical absorption coefficient, only a few microns (1-2 μm) of CdTe is sufficient to absorb incident spectra; this reduces the amount of material required substantially. The CdTe PV devices are manufactured in superstrate configuration. The problems, in addition to its toxicity due to the presence of cadmium, are exacerbated by its inherent metastable behavior, which affects its electrical parameters, especially when testing indoors [21, 22] under exposure to light or elevated temperatures. This requires

harmonization and improvement in the current measurement standard, IEC 61215-2.

A reversible metastable effect is observed in CdTe modules, where they all show changes in their performance upon exposure to light, driven by the presence of defects [23]. Under low light exposure (< 50 W/m^2), it is easier to observe the influence of metastability on the fill factor, which is mainly influenced by the high series and the low shunt resistance. This generally affects the open circuit voltage and the maximum output power.

Illumination triggers metastabilities that lead to non-stable behavior of the electric parameters of the modules [24, 25]. The dynamic change makes it tedious to measure the nominal power. The protocol generally followed for power rating CIGS modules was also extensively used for CdTe technology. NREL made the latest proposal for a harmonized power rating of thin-film modules for CIGS and CdTe. It was adopted in the new IEC 61215-2 standard [24]. Suitable for most commercial modules, all these methods lack (a) an understanding of the underlying effects and therefore (b) general validity for new module types [26]. Therefore, it is essential to (c) establish a correlation between the low-light behavior and the module state (e.g., rate of degradation) and (d), in principle, understand the origin and nature of the metastabilities. Additionally, in low light, similar modules can respond differently, which can lead to an incorrect estimation of the module's performance when estimating its energy yield. It can affect a standard power rating of the module [24].

This study was conducted on several standard commercial CdTe modules, which were mounted outdoors in a PV power plant for some years, and a module fresh from a manufacturing facility. The modules installed outdoors varied in terms of degradation (between 22.11 % and 4.62 % below the nominal power labeled) and were chosen for the pretreatment process. This work investigated the dependence of power-rating results on the degradation level. Further, the variation of the power-rating result was investigated for preconditioning of the modules (i) with illumination and (ii) with biasing, followed by illumination. It was observed that the higher the amount of degradation (in terms of deviation from its nominal power) of the module, the greater the degree of deviation in its electrical behavior.

CdTe cells are most commonly deposited by using the closed-space sublimation technique. For fabrication as a superstrate type, a high-quality TCO is deposited like an indium tin oxide (ITO) on glass. A layer of ZnO and CdS is deposited as a buffer layer, forming a heterojunction with the CdTe absorber material. The back contact is typically made of a carbon paste with copper.

All PV technologies require a standard performance measurement procedure to quantify their reliability in outdoor facilities. A transient effect is observed in all thin-film technologies, such as a-Si and CIGS, which are all subject to changes in

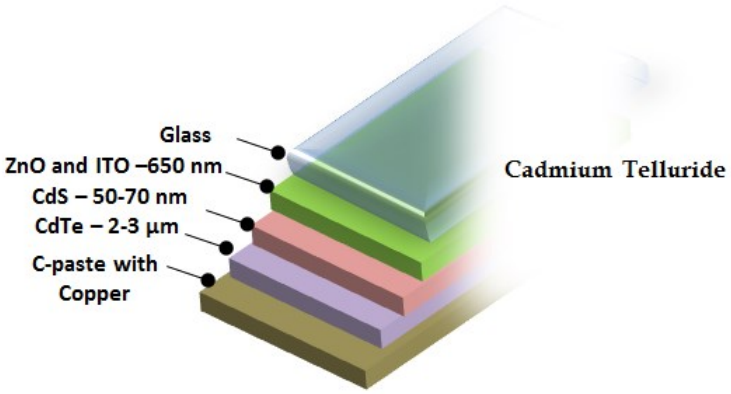

Fig. 2.16: Cell morphology of a superstrate-type CdTe photovoltaic device.

their performance upon light exposure driven by defects. These metastable changes in performance parameters can introduce ambiguity in energy yield, which is further used to calculate the cost of electricity. For conducting a performance measurement (I-V characterization at Standard Test Conditions) on thin-film devices, special care should be taken because of the reversible transient nature of light-induced metastabilities, which can introduce errors in repetitive measurements.

Tab. 2.3: Sample modules for the pre-treatment experiments

Samples	State of operation	Stabilization
Sample 1-5	Outdoor	Preconditioned indoors
Sample 6	Indoor	Unstabilized

Table 2.3 shows the commercial modules that were used for experimental purposes. All of the samples were glass-glass type. Samples 1-5 used in this study were operated outdoors for years, including laboratory treatments such as preconditioning. Sample 6 was unstabilized without performing any treatment and was used as a reference.

The protocol generally followed for power rating the a-Si modules was extensively used for CdTe technology. NREL made the latest proposal for a harmonized power rating of thin-film modules for CIGS and CdTe. It was also adopted in the new IEC 61215 standard. However, the proposed preconditioning procedure was intended to improve existing protocols to achieve a stabilized power rating. Still, according to our findings, it did not meet the stabilization after treating the modules with bias preconditioning. Despite being useful for most commercial modules, all these methods lack (a) an understanding of the underlying effects, and, therefore, (b) general validity for new module types. Hence, it is important to (c) find a correlation between the low-light behavior and the module state (as, e.g., rate of degradation). Additionally, under low-light conditions, similar modules can respond differently, which can lead to an inaccurate estimation of the module's performance when

calculating its energy yield. It can affect the standard power rating of the module [27, 28].

2.9 Kesterite

Another thin-film material used for solar cells has a kesterite structure, highly similar to the CIGSSe chalcopyrite structure, as shown in figure 2.17. The defects present inside both structures show similar effects in their electronic properties. Tungsten and molybdenum are the refractory metals that prevent these metals from diffusing into the absorber material. CZTSSe has a p-type conductivity with a tunable bandgap ranging between 1.0–1.5 eV and a high optical absorption coefficient ($>10^4$ cm^{-1}) [29, 30, 31, 32, 33].

CZTSSe used here has a monograin structure, where each monograin is a complete solar cell in itself. It is a heterostructure architecture, where the absorber/buffer interface has a spike at its conduction band minima. This reduces the recombination of the majority charge carriers at the absorber/buffer interface, reducing loss in V_{OC}. The same effect has been observed in CIGS solar cells [16].

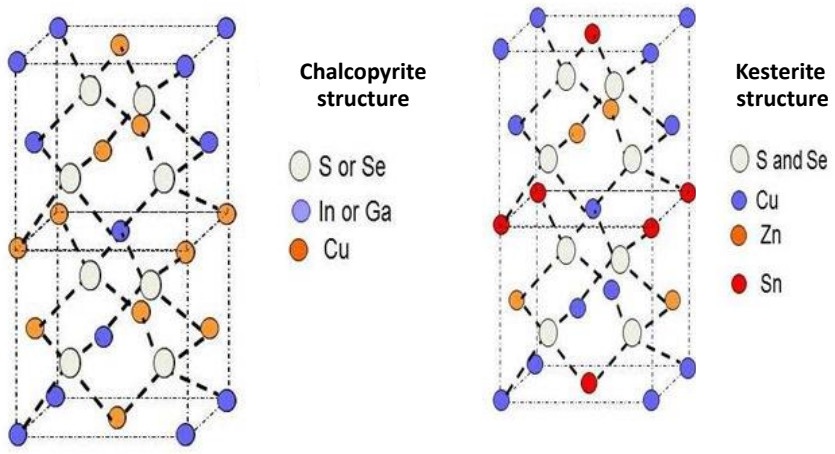

Fig. 2.17: Crystal structure of CIGSSe and CZTSSe materials
(Taken from: Parag S. Vasekar and Tara P. Dhakal (2013). Thin Film Solar Cells Using Earth-Abundant Materials, Solar Cells - Research and Application Perspectives, Prof. Arturo Morales-Acevedo (Ed.), InTech, DOI: 10.5772/51734)

The samples used here were all monograin CZTSSe type of PV devices, as shown in table 2.4. In this work, cells and minimodules were used for the characterization. The cells used here were 0.16 cm^2 in size, and the minimodule consists of 12 cells in series, with a total area of 65.7 cm^2.

A kesterite solar cell structure is similar to those made of CIGS and CdTe, see figure 2.18. All of these cells consist of a molybdenum-coated back contact and a ZnO window layer. CZTS material was first synthesized in 1966 and was found

Tab. 2.4: Sample cells and modules for experimentation purposes

Samples	State of operation	Stabilization
Cell 1x,2x and 3x	Indoor	not preconditioned
Module non-degraded	Indoor	not preconditioned
Module degraded	Indoor	not preconditioned

to exhibit a photovoltaic effect in 1988. It is one of the promising PV materials, as its bandgap lies between 1.4 and 1.5 eV, with a large absorption coefficient. CZTS is a semiconductor quaternary compound material of the I-II-IV-VI group, with electro-optical properties similar to the CIGS material. CZTS can be obtained from the CIGS chalcopyrite structure by replacing the In/Ga structure with Zn and Sn, forming a kesterite structure.

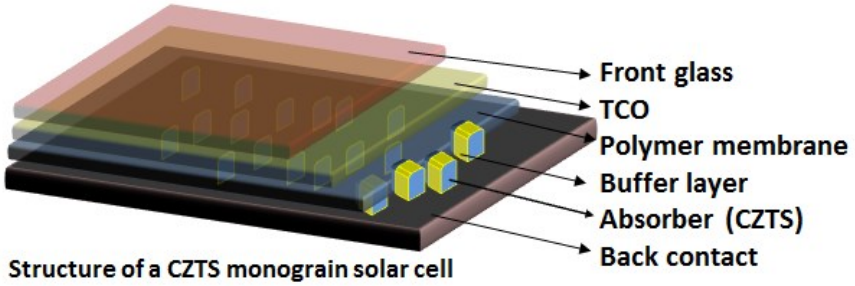

(a) a

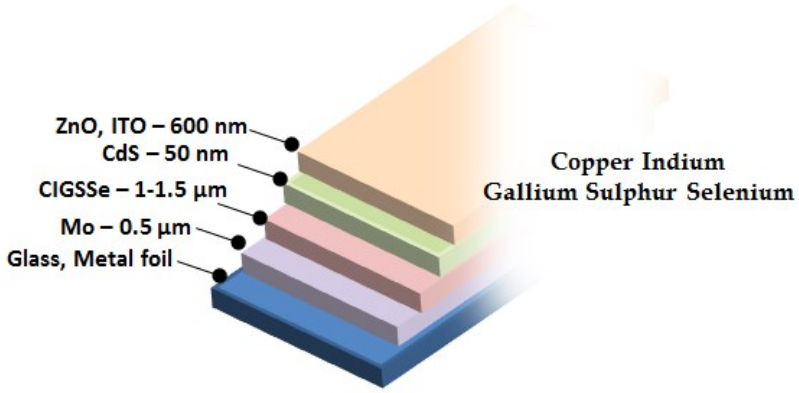

(b) b

Fig. 2.18: Cell morphology of (a) CZTSSe monograin substrate type and (b) CIGSSe superstrate type photovoltaic device

Unlike similar carrier concentrations and absorption coefficients of CZTS and CIGS, the carrier lifetimes are low in CZTSSe material due to high defect complexes or

recombination at the grain boundaries. The material used for this research was CZTSSe, which has a band gap smaller than that of CZTS. In these materials, the leading cause of recombination is the secondary phases formed at the interface, which act as the leakage current paths or the recombination centers. CZTSSe is a self-doped material through formation of internal defects in the form of vacancies (V_{Cu}, V_{Zn}, V_{Sn} and V_S), antisite defects (Cu_{Zn}, Zn_{Cu}, Sn_{Cu}, Zn_{Sn}, and Sn_{Zn}) and interstitial defects (Cu_i, Zn_i and Sn_i). According to theoretical calculations, the Cu-Zn cation is a fairly common defect that is expected to form. CZTS is a material that can be prepared through vacuum and non-vacuum techniques.

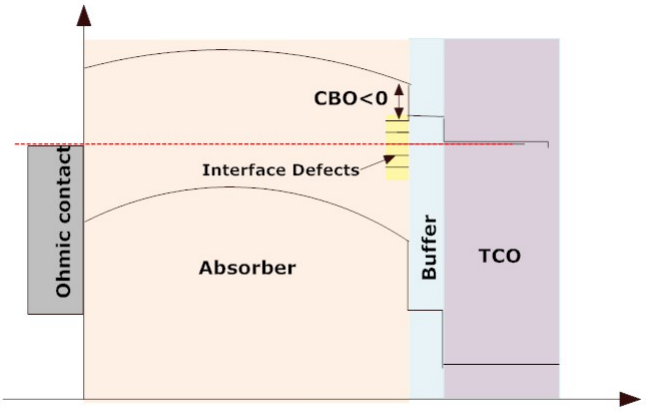

(a) a

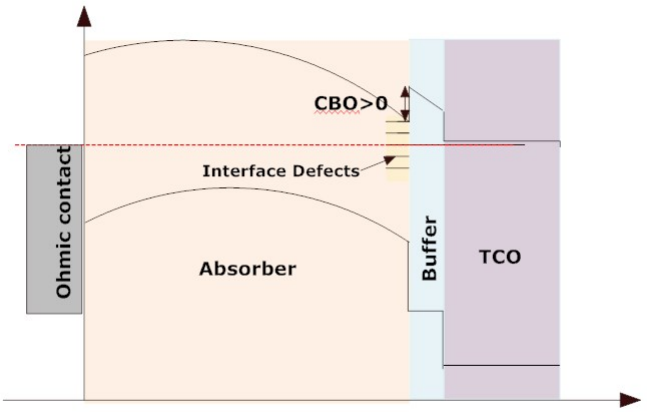

(b) b

Fig. 2.19: Bandgap configuration in CZTS and CIGS of (a) cliff and (b) spike

The band gaps of the CZTSSe and CIGS show a similar behavior under light-induced defect formation. Both CZTS and CIGS configurations are shown in detail in figure 2.19. Sometimes spike or cliff effect forms at the interface of the absorber and buffer layers' interfaces. The current-voltage (I-V) curve for a negative conduction band offset depends heavily on the amount of interfacial recombination and exhibits reductions in voltage and fill factor due to the increased forward current. When CdS

is used as the buffer layer with CIGS, low gallium concentrations result in a spike, and high ones result in a cliff.

If there is a band offset for minority carriers in the buffer layer, it can lead to the formation of a 'spike' or a 'cliff', depending on the sign of the offset. If the band offset produces a cliff, the probability of inter-recombination at the interface increases, and the flat band condition is achieved with a bias smaller than E_g/q of the absorber [5]. One consequence is that the cell output voltage is limited due to a lack of barrier height. Band alignment with a moderate spike is rather optimal, although the presence of a spike means that the band offset for the minority carrier decreases, and the interface becomes less selective.

Chapter 3

MEASUREMENT EQUIPMENT AND THEIR UNCERTAINTIES

> *Error, never can be consistent, nor can truth fail of having support from the accurate examination of every circumstance.*
>
> **— James Hutton**
> (Scottish geologist and physician,)

Measurement uncertainty provides information about the estimated error of a specific measurement procedure. We commonly consider systematic and random errors to be part of the error measurement [34, 35].

3.1 Flasher

The class A pulsed simulator meets the standard IEC60904-9 when it has 0.75-1.25 of spectral match, less than 2% of nonuniformity of irradiance, less than 0.5% of short-term temporal instability of irradiance, and less than 2% of long-term temporal instability of irradiance. The flasher is placed in a vertical setup and can emit irradiance from 200 to 1100 W/m^2 by changing the charge capacity of a Xenon flash tube (lamp power). The illumination time of the flasher can reach up to 10 ms. However, in practice, the trigger delay was set to 2.5 ms to minimize irradiance fluctuations at the beginning of light emission.

3.2 Electronic and Electric Load

3.2.1 Passive load measurement equipment

The Berger is an ohmic load measurement device called a 'passive load measurement equipment'. This instrument features resistances in a cascade connection, which allows for various combinations of resistances to be measured, enabling the determination of the corresponding voltage and current to create the I–V curve. To obtain the whole I–V curve, 80-150 data points per dataset were measured. 30 μs of the measuring time per data set point and 5μs of the interval between each point are set. The total measurement time (trigger delay + measurement time of the I–V curve)

should be less than 9 ms, so that the temporal stability of the irradiance can be less than 2 %.

3.2.2 Active load measurement equipment

The Pasan (Model no. BV 66) is an active load measurement device for pulsed light measurements. The voltage and current ranges are up to 300 V and 30 A, respectively. The number of measured data points for each measurement was around 250, which could be measured within the 10-ms range. The Pasan load measures the V–I characteristic through an active voltage and current source, traversing the specified voltage range. Starting from -26 V, it sweeps the voltage across the module to measure the current and voltage characteristics.

3.3 Setup used for light soaking for the pretreatment

The lamp array used during the light soaking experiment, model number MASTER SDW-T 100W/825 PG12-1 HG 1SL, is a high-pressure sodium lamp that gives a golden yellow light in the visible spectrum. The two spectral lines at 589.0 nm and 589.6 nm are the dominant features in the sodium spectrum. The atomic spectrum of sodium is broadened into a continuous spectrum due to the high vapor pressure inside the tube.

The spectra of the lamps were observed using a portable grid spectrometer (Ocean Optics HR2000+), which revealed a trend of two peaks in the spectrum, one located in the 550 nm to 600 nm range and another in the 600 nm to 700 nm range. The wavelength spectrum extends from 380 nm to 800 nm, encompassing the visible range and a portion of the infrared spectrum. The spectra were measured at different positions under the lamp array. They are plotted parallel in the graph with the sun spectra of AM 1.5, downscaled to a factor of 6.5 for visual comparability. This also provided evidence that all components of natural sunlight were included, albeit in varying magnitudes.

3.4 Using the integrated software of PASAN to calculate temperature coefficients

The Pasan software automatically corrects the I–V curve according to the IEC correction and also performs temperature compensation. After each flash, the Pasan software asks for the temperature of the module and the reference cell to compensate for the results. Pasan uses the temperature coefficients for the PV modules as a modified input parameter to compensate for the results. α is the temperature

coefficient for the current, and β is the temperature coefficient for voltage, as shown in equation no. 3.1 and 3.2.

$$\alpha = \frac{I_{\text{SCtk}}}{A_{\text{Cell}}} \tag{3.1}$$

In equation (3.1), the temperature coefficient α for Pasan is calculated from the temperature coefficient for the current (I_{SCtk}) divided by the area of the cell (A_{cell}).

$$\beta = \frac{V_{\text{OCtk}}}{N_{\text{Cell}}} \tag{3.2}$$

In equation (3.2), the temperature coefficient β for Pasan is calculated from the temperature coefficient for the voltage (V_{OCtk}) divided by the number of cells in the module (N_{Cell}).

3.5 Measurement errors

Measurement errors are the differences between the measured value of a quantity and its true or accepted value. These errors can arise from various sources, including instrument accuracy, environmental conditions, operator errors, or inherent uncertainties in the measurement process.

3.5.1 Errors caused by measurement loads

The measurements for the pretreatment of the module were made mainly using the PASAN device to simulate the electrical load. It has an accuracy of 0.1% for measuring current and voltage values. The light soaking effect, measured by the PASAN electronic load, was performed on different amorphous silicon modules and micromorph modules, as listed in Table 1. All modules showed a short-term metastable effect in the same increasing profile in the case of a-Si and reversal behavior in a-Si/μSi for electrical parameters such as V_{OC}, P_{MPP}, and FF.

Although the overall change in magnitude of the electrical parameters during measurements was in the range of 0.3% to 5.3% (varying for different specimens and module types), the reproducibility between the two measurements (electronic measurement resolution) was high. As all raw data points were temperature-corrected by the PASAN software, the impact of this correction on the results was also checked.

It should be said that there might be some change in the electrical parameters, which could have been introduced due to a mismatch in the spectral distribution inside the flasher or due to induced current in the wires, or maybe due to the positioning of the reference cell [36, 37]. Each module's I–V characteristic was measured precisely to exclude these errors. Furthermore, the reference module was measured periodically to detect any deviation in the I_{SC} and V_{OC} values of the polycrystalline reference

module. The deviation in electrical performance of the reference module has to remain below the 0.5% of the previous value of I_{SC} and V_{OC} for the setup to work well. The observable change was less than 0.01% in the absolute values of the previous module.

In addition, module measurements were always performed under 1-sun illumination in the flasher after a light soak under a 50 W/m^2 lamp illumination. The flash duration was relatively short, around 10 ms, which could have produced only a slight light soaking effect compared to the effect of light soaking by the lamp field.

3.5.2 Spectral mismatch

Spectral mismatch occurs when there is a difference between the spectral response of the light source of the static sun simulator and the AM 1.5 sun spectra and also the spectral response between the reference cell and the device under test during an I–V measurement [38].

3.5.3 Temperature effect

It was observed that there was a small increase in temperature during the light soaking of the module. The increase in temperature was below 7°C. This change was thought to be caused by the computational algorithm used by the PASAN. To verify this, 30 arbitrary temperature values were entered into the PASAN software. The formula used by PASAN to correct the data is provided in Appendix 2. The calculations performed by the software showed overcompensated values of I_{SC}, V_{OC} and P_{MPP} when compared to the results of the correct temperature. This clearly demonstrated that light soaking produced an effect on the module, which was not due to spurious or temperature effects.

Since all pretreatment experiments were performed in varying temperature profiles (5°C to 7°C), it was realized that the dependence of the electrical parameters on temperature is also accounted for; therefore, a specimen from Bangkok Solar was chosen for the experiment. A constant temperature (variation in the range of 1°C) was maintained throughout the experiment by heating the module to an estimated equilibrium temperature at 27.5°C (which was found to be the equilibrium temperature of the module due to LS) inside the flasher. It was observed that maintaining a constant temperature does affect the electrical parameters, with slight changes in power and the magnitude of the fill factor. However, a change in the open-circuit voltage showed an increase in magnitude of 50% less than that observed at the increasing temperature profile.

Chapter 4

EXPERIMENTAL SETUP

> *The proper method for inquiring after the properties of things is to deduce them from experiments.*
>
> — **Isaac Newton**
> (English physicist and mathematician)

Electrical-optical characterization techniques are a powerful tool in the investigation of PV devices. Various non-invasive techniques applied to solar cells and modules help investigate the causes of metastabilities. The techniques employed include power rating according to IEC standards, external quantum efficiency measurement, electroluminescence and photoluminescence, color-selective low-irradiance illumination, and impedance spectroscopy. These techniques are explained in the following sections.

4.1 Power Rating

Power rating is a procedure where the nominal power of a PV module given by the manufacturer is tested indoors under a sun simulator following an internationally recognized IEC standard, as described in section 2.4.1. This test ensures that the module can deliver the power quoted on the datasheet. A light source of a xenon long-arc flash lamp is used in the solar simulator to test the industrial-scale modules using PASAN or Berger load. I–V (current as a function of voltage) curves were taken for a duration of 10 ms under 1000 W/m^2 illumination, with a trigger delay of 2.5 ms. A typical measurement is made with a four-wire connection from an electronic load, sweeping the voltage from the short-circuit current (I_{SC}) to the open-circuit voltage (V_{OC}), as it is less susceptible to capacitive or metastable changes.

4.2 Pretreatment

The pretreatment involves exposing a module or cell to low-irradiance illumination before it is measured at standard test conditions (STC). Before starting the experiment, the modules were kept in the dark for at least 2.5 hours or overnight to minimize any instability caused by stray illumination. The experimental setup for the LS is comprised of a sodium vapor lamp array integrated in front of the pulsed solar simulator. This facilitates the acquisition of standardized I–V curves

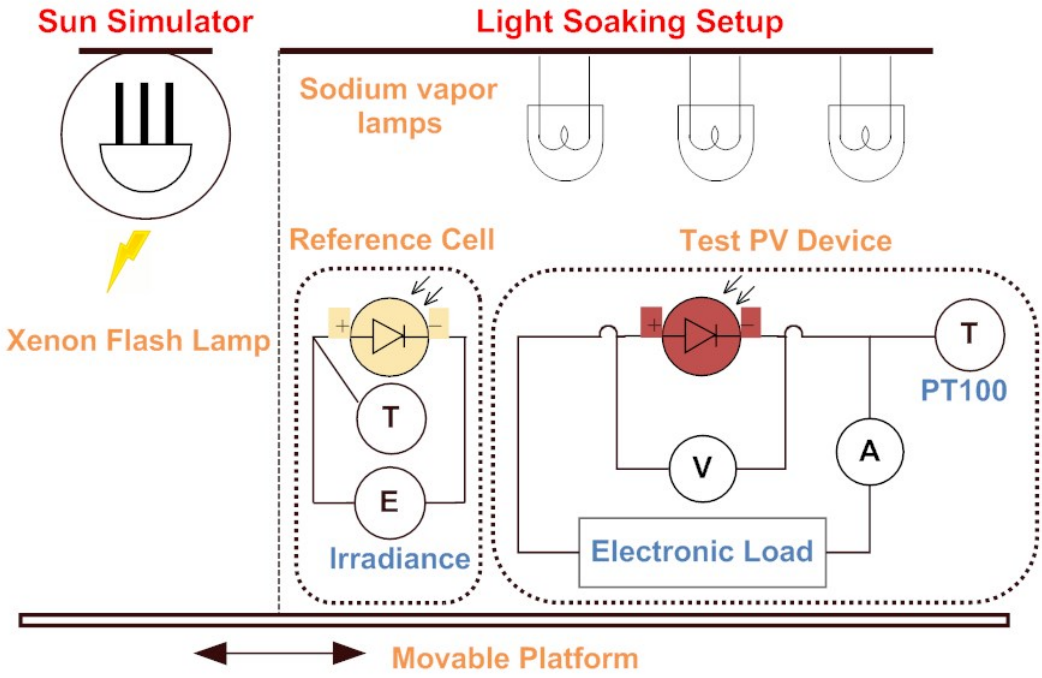

Fig. 4.1: Pretreatment setup for conducting light soaking of a thin-film PV device

without requiring the transfer of modules each time for I–V tests. Modules are kept in open-circuit conditions during the LS cycle. The high-pressure sodium vapor lamp array irradiates the module plane with $\sim$50 W/m^2 at a spectral distribution above the wavelength of 550 nm. The lamp array was turned on for 0.5 hours to stabilize the light. The PV modules were exposed to low irradiance for approximately 2 to 3 hours. Some modules reached a saturated state under illumination. After the module's performance reached saturation, pretreatment was continued in dark storage (DS) conditions until a stable state of the module's power output was achieved. During the DS period, the I–V curves were repeated at successive intervals. The last measurement performed during the LS cycle corresponds to the first measurement at the beginning of the DS cycle. The setup for the pretreatment is shown in figure 4.1.

The solar simulator utilizes a variable electronic load and is of the AAA-class pulsed light type. For some samples, pretreatment was performed at two different temperatures to observe how metastability affects the electrical parameters. The first pretreatment cycle was conducted at a temperature variation of +5 K to +7 K during the LS and DS test periods. During the LS and DS test periods, the second pretreatment cycle was carried out at a temperature variation of $\pm$0.5 K. During the pretreatment period, the modules were kept under constant static illumination of

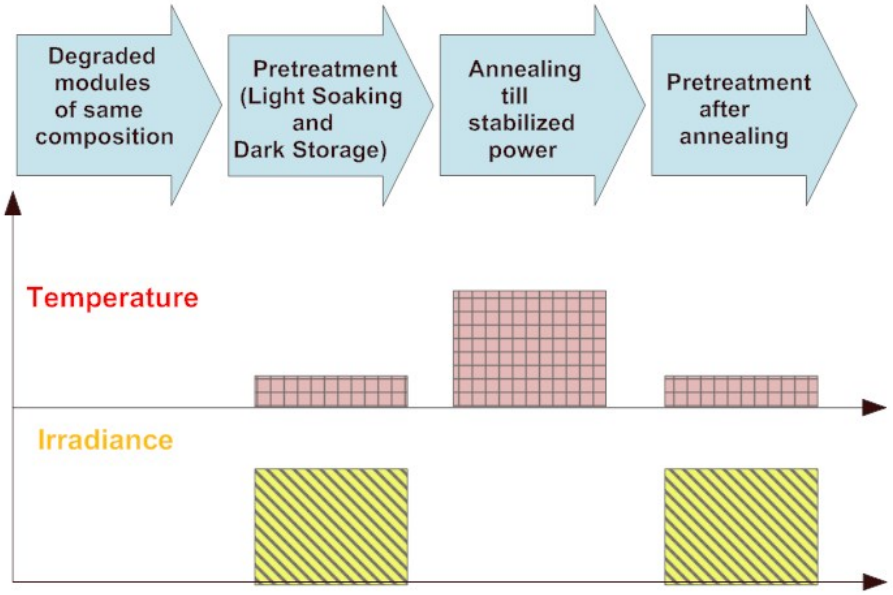

Fig. 4.2: Pretreatment cycle

$\sim$50 W/m^2 and afterwards in darkness while taking repetitive I–V curves corrected to the STC conditions according to Eq. (1) and (2), as explained in the next section.

4.2.1 Pretreatment under load and short-circuit conditions

The LS and DS procedures for this experiment were the same as those for the pretreatment experiment. The only change was that the modules were operated under MPP or short-circuit conditions of their respective I–V curve. The load point was set by an external ohmic resistor in series with the module. Choosing a load point at such low irradiances is a challenging task, as it has been found that the conventional IEC formula does not hold for low irradiances. The load resistance values were chosen by selecting a voltage slightly less than V_{OC} and I_{SC} to be approximately one-tenth of the I_{SC} value, and then calculating the corresponding load resistance value. The load point for each module was checked by measuring the corresponding voltage and current values for the modules at the calculated load. For micromorph technology, the load value was chosen to be 1200 Ω, as it was found that voltage and current were not able to reach its MPP value using the ohmic load. For the Schott module, the load resistance was chosen to be 30 Ω, and for the Bangkok Solar, the load was chosen to be 6.2 Ω. During short-circuit testing of the modules, the load was changed to zero to perform the pretreatment of the module under short-circuit conditions. For all modules, whether under load or short circuit, the I–V characterization was performed under open-circuit conditions only, which required approximately 15 to 20 seconds to obtain the I–V curve (including module movement). The remaining modules were kept under load or in short circuit.

4.2.2 Colored light pretreatment

This pretreatment involved only small cells (< 1 cm^2), as commercial modules could not be used due to their size restrictions. A stationary sun simulator, accommodating only cells and minimodules, was used to perform the colored light pretreatment. Monochromatic filters were used to differentiate the impact of different selective wavelengths of light on PV devices. The colored filters were chosen in the sequence from smaller to larger wavelengths. The small wavelength was represented by a blue color, the middle one by green, and the large wavelength by a red color filter.

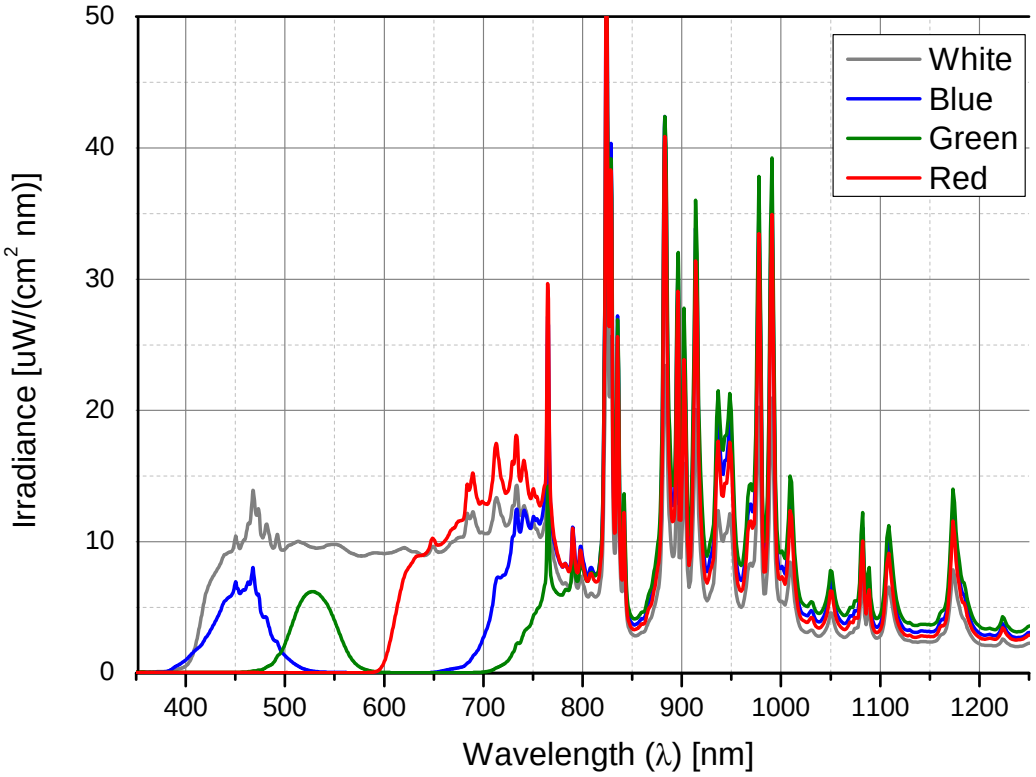

Fig. 4.3: Spectra of the white light of the Xenon lamp and with filters (red, green, and blue) used for the light soaking pretreatment

Figure 4.3 shows the comparative spectral response of various filters under a xenon lamp and white light. The purpose of colored filters is to target a specific layer in the solar cell, depending upon the photon's energy; the higher the photon's energy, the quicker it is absorbed. Typically, blue light is primarily absorbed in the top layers, which have a large bandgap.

The purpose of the proposed wavelength-selective light soaking is to determine the influence of defects on the electrical parameters and the amplitude of change in the performance parameters of the solar cells. Exploiting this property, it was possible to determine the direction and origin of the metastability in the cells. The white- or

color-filtered, low-light soaking behavior of solar cells can provide information on cell metastabilities and their origin within the heterojunction. Taking the example of a kesterite solar cell, the light passes through the top transparent conductive oxide (TCO) contact and the transverse window (ZnO) and the buffer layer of the cadmium sulfide (CdS) layer before being absorbed in the kesterite itself, generating charge carriers. As a result, the light of smaller wavelengths is significantly absorbed in the top layers, while the light of larger wavelengths is mainly absorbed in the absorber.

The irradiance was approximately 80 W/m^2, and I–V curves were measured under the same illumination conditions in a Class BBB static solar simulator with a shutter mechanism using an electronic load and a reference cell for the monitoring of the irradiance. Two filters were used to quantify the effects of specific wavelengths: blue (450 nm) and red (650 nm) for light soaking. Two sheets of white paper attenuated the light to 80 W/m^2 level for the white-light soaking.

Before light-soaking measurements, the PV devices were kept overnight in the dark to avoid parasitic light and ensure stabilization. Each light-soaking measurement was carried out for approximately 250-300 minutes. After each light-soaking measurement, the PV devices were stored in the dark to ensure stabilization before the next light-soaking was performed.

An I-V curve measurement was also performed under standard test conditions (STC) to determine the actual performance parameters of the device, as explained in Section 2.3. The STC measurement was performed before starting with the light soaking, immediately after completing the light soaking, and after the PV device was stored overnight in the dark.

4.3 Temperature and irradiance correction for current and voltage

The I–V characteristics of a PV device must be corrected for STC conditions, according to the IEC 60904-1 standard. There is also a standard procedure to follow when performing a standard I–V characterization. First, a reference device with a spectral response similar to that of the device under test is required; otherwise, the device and the reference cell's spectral responses should be corrected using the spectral mismatch factor. A correction should be applied to the reference cell's temperature and its temperature coefficient, as provided in the STC conditions. The reference cell should exhibit linear behavior in I_{SC} over a range of irradiance, as specified in IEC 60904-10.

4.3.1 Temperature correction equations

The time variation of the open circuit voltage (V_{OC}), maximum power point (P_{MPP}), short circuit current (I_{SC}), and fill factor (FF) was analyzed. The results of similar experiments carried out on CIGS and CdTe devices have recently been reported [39, 18, 40]. For the first time, these pretreatment experiments were applied to the amorphous silicon family of thin-film photovoltaics.

A high-precision measurement system, as specified in IEC 60904-1, was used to conduct an I–V characterization (see Section 4.3). The translation of the I-V curve according to the IEC 60891 correction procedures [41] was followed to recalculate the power rating relating to the STC conditions, which describe the requirements for evaluating the performance of the PV module in terms of power over a standard irradiance and temperature. The electrical parameters (V_{OC}), (P_{MPP}), (I_{SC}), and (FF) were extracted from the achieved I–V curves for all experiments.

The power correction according to the IEC standard [41] is derived by the following formulas:

$$I_2 = I_1 + I_{SC}.\left(\frac{G_2}{G_1} - 1\right) + \alpha.(T_2 - T_1)\,, \tag{4.1}$$

$$V_2 = V_1 - R_S.(I_2 - I_1) + \beta.(T_2 - T_1)\,, \tag{4.2}$$

where I_1 and V_1 are the coordinates of the measured I–V curve,
I_2 and V_2 are the coordinates of the translated I-V curve,
G_1 is the irradiance measured with the reference cell,
G_2 is the irradiance at desired conditions in the matrix,
T_1 is the module temperature,
T_2 is the desired temperature in the matrix,
I_{SC} is the measured short circuit current of the test specimen in the measured I–V curve,
R_S is the internal resistance of the test module.
The two constants α and β are the temperature coefficients for the current and voltage of the module.

The subscript '1' denotes all parameters measured with the experimental setup, whereas the subscript '2' refers to the corresponding parameter in the standard specifications. The symbols I, V, G, and T correspond to the current, voltage, irradiance, and temperature, respectively. The series resistance of the module, R_S, which is assumed to be independent of G and T, must be determined separately. In the case that $T_1 > T_2$, the temperature coefficients α (for the current) and β (for the voltage) must also be determined to successfully transform the measured I–V curve to the standardized one. The temperature coefficients were used as mentioned on the datasheet of the selected PV modules. The R_S was calculated from the slope of the data points near the V_{OC}.

4.4 Preconditioning

To measure a PV device under IEC standard testing, it must be soaked in light to achieve power stabilization. This can be done by:

- Irradiation under sunlight operating the PV module at its load point
- Irradiation under artificial light operating the PV module at its load point

or to let the PV device go through the light-induced stabilization cycle. The number of hours under light depends on the technology. For silicon wafer technology, it is recommended to be 20 kWh/m^2 for two or three cycles, and for thin film technologies such as a-Si, it is recommended to irradiate the module for a period of 43 kWh/m^2. In CdTe and CIGS technologies, it is recommended to irradiate them for 20 kWh/m^2 for two or three cycles until the power stabilizes.

4.4.1 Light induced stabilization

Every commercial PV module must undergo a testing cycle of light-induced stabilization, where modules are exposed to light for a specified time under an artificial light source to observe whether the electrical output power has stabilized.

$$(P_{\text{MAX}} - P_{\text{MIN}})/P_{\text{AVERAGE}} < x, \tag{4.3}$$

where x is defined in the technology-specific parts of this standard.

According to the IEC 60904-9 standard, the sun simulator must be a BBC class standard. Our sun simulator is a class BBB standard. During exposure to the sun simulator, it is ensured that the temperature is in the range of 50 $\pm$ 10°C for all thin-film technologies. An exception is made for the a-Si technology, which should be below 55 °C, because it is highly prone to annealing effects at higher temperatures, as shown in our findings at the low-temperature annealing. All PV technologies should be maintained at their maximum power point using a resistive load during preconditioning. Each module technology is subject to at least two irradiance exposure intervals until the PV module has achieved equilibrium. For the a-Si technology, each preconditioning cycle is defined as 43 kWh/m^2, where it must run for a minimum of two cycles of operation until the electrical output power stabilizes at the defined level. For CdTe technology, the light-induced stabilization cycle requires a minimum of at least two intervals, each with a power density of at least 20 kWh/m^2. The temperature should stay at 50 °C during the preconditioning inside the sun simulator.

4.4.2 Bias procedure

An alternative stabilization procedure with the same effect as light exposure is termed a current or voltage bias procedure. It is a relatively new procedure that

requires verification for its reliability. The thin-film technologies are shown to be sensitive to bias at higher currents and voltages. As proposed by NREL, a PV device is biased with a voltage up to 90% of its V_{OC} and must be kept in the dark for 90 minutes.

4.4.3 Thermal annealing

Thermal annealing was performed to observe the changes in power recovery of amorphous silicon modules. Power recovery directly relates to the reduction of defects in solar cells. Many defects in amorphous Si have low activation energy, which could be sufficiently supplied at low temperatures. The defect density inside the a-Si:H is reduced when subjected to higher temperatures. The reduction in dangling bond density is expressed as a function of annealing time. This is given in the form of a stretched exponential curve

$$\Delta N_{\mathrm{d}}(t) = \delta N_{\mathrm{d}}(0) \exp(-(t/\tau)^{\beta}), \tag{4.4}$$

where β and τ depend on the applied temperature. In a stretched exponential function, β expresses the rapid decay. In contrast, τ represents the lifetime to represent the decay characteristics in a long-term region.

4.4.4 Low-temperature light annealing

The modules were subjected to initial annealing under light in a climate chamber. This was chosen to replicate outdoor conditions. Nevertheless, a-Si technology was seen to anneal outdoors in years of field operation. It is assumed that the annealing that originates from it drives the annihilation of the defect. Interestingly, defect recovery was observed at a low temperature of 60°C to 75°C. The modules were annealed under light and elevated temperatures and operated in a climate chamber for an extended period. After several hours, the modules were left in the dark to continue low-temperature annealing.

Photovoltaic modules are not unusual to reach above 80°C or 90°C in the field, mostly in tropical countries. This can cause a fast annealing process, resulting in higher efficiency and power delivery from the PV module. Another crucial factor in achieving higher output during the summer is related to the spectrum, which is relatively rich in its blue part.

4.5 Quantum efficiency

Quantum efficiency measures the number of incoming photons absorbed by a photovoltaic device over the resulting current. The light source consisted of a quartz lamp with a slit. In the setup, we used a monochromator composed of 3 filters and two gratings. The wavelength ranges were 0-375 nm, 375-585 nm, and 585-infinite.

Grating 1 is set from 0-400, and grating 2 is set from 400 to infinity. Typically, the beam size is 2×0.5 mm^2.

To calibrate the device, the signal from the reference Si detector is first measured and amplified using a lock-in amplifier. Then, a standard reference solar cell is measured to check the accuracy of the measurement by comparing it with the last measurement. After completion of these steps, the external quantum efficiency of a solar cell is measured.

The light source consisted of a quartz tungsten halogen lamp with a reflector behind the lamp to minimize light ripple and provide stable output. The modulated light is passed through the motorized filters into the Oriel Cornerstone 260 1/4 m monochromator. The purpose of filters is to remove any wavelength doubling from the diffraction gratings. The monochromator is composed of ruled diffraction gratings to generate an output of monochromatic light focused into a defined area. The detector is calibrated in the range of 200 nm to 1100 nm. The test is then repeated for the device under test (on a small solar cell area), where the total optical power is compared with the generated current.

The detector calibration compares a device under test with a standard Si detector, which has a known spectral response. To calibrate the device, the signal from the reference Si detector is first measured and amplified using a lock-in amplifier (Oriel Merlin digital lock-in radiometry system). The Merlin control unit acts as a lock-in amplifier, which retrieves signals and rejects unmodulated radiation. Then it computes the signal value using the loaded detector calibration data. This is stored as a reference detector file. Afterward, a standard reference solar cell is measured to check the accuracy of the measurement by comparing it with the last measurement. After these steps are completed, the external quantum efficiency of the solar cells is measured. The device under test generates a spectral response when exposed to the beam, which is then converted into external quantum efficiency.

The external quantum and spectral responses are related as follows:

$$\eta QE(\lambda) = 1239.8(S(\lambda)/\lambda), \tag{4.5}$$

where η QE(λ) is the external quantum efficiency, S(λ) is the spectral response and λ is the wavelength.

4.6 Electroluminescence

The camera used for measuring the electroluminescence (EL) of the thin-film modules was manufactured by Sensovation, model number coolSamBa HR 830. It has a high resolution of 8.3 Megapixels (3326x2504 pixels), with a high signal-to-noise ratio at sufficiently long exposure times. The image sensor type is a full-frame, scientific-grade silicon CCD with on-chip microlenses, an ITO transparent gate, and

a low dark current. It can collect frames at 0.3 per second with a 16-bit dynamic range, allowing for the detection of even the most minor defects in the cells.

The CCD camera captures the emitted near-IR radiation from the module and produces a digital image of the module surface. A mixture of various cell defects causes the radiation emitted. EL imaging is performed in the dark, as light can interfere with the sensor and introduce noise within the system.

4.7 Impedance spectroscopy

For impedance spectroscopy of solar cells, we used an HP4562 LCR meter, with a frequency range of 10 kHz to 1 MHz under voltage bias. A small AC voltage is applied in conjunction with the DC voltage bias, allowing for a linear charge response (dQ = CdV) and facilitating the application of the small signal approximation.

4.7.1 Voltage-dependent capacitance measurements

The capacitance–voltage (C–V) method is a standard measurement technique to determine the charge carrier concentration in a solar cell. The depletion capacitance is determined during the reverse bias, and the diffusion capacitance is determined during the forward bias. The depletion capacitance is a result of the majority of carriers. The diffusion capacitance is due to the minority carriers.

The setup consists of an Agilent LCR Meter 4284A and a four-point measurement using gold-coated tungsten pins. Since the focus is on the capacitance building up in the space charge region of the solar cell, it is studied in the reverse-bias region. It is ensured that the negative bias is in the range where the cell does not reach its breakdown voltage. A small AC signal is applied at a frequency in a range higher than 10 kHz, such that the trap or defects do not suppress the effect. Moreover, at higher frequencies, it provides a more accurate estimation of the capacitance. The squared inverse capacitance is plotted against the applied voltage bias.

4.7.2 Frequency dependent capacitance measurement

In the capacitance–frequency (C–f) method, it is helpful to measure capacitance, conductance, or impedance as a function of the test frequency. The frequency range is generally 10 kHz to 1 MHz. Both the sweep frequency range and the bias voltage can be adjusted. The desired parameters, such as the trap densities, can be extracted from the capacitance vs. frequency data. The measurements can be repeated at various temperatures.

An equivalent circuit for impedance measurement includes a diode in parallel with a capacitor related to the diode response and will respond to an AC voltage.

Properties required for impedance spectroscopy:

- The absorber material is conductive and the dielectric relaxation frequency does not affect the measurement.
- The junction is abrupt, and good ohmic contacts.
- Only the majority charge carriers participate.
- The cell is operated in reverse bias mode.

4.8 Technology Overview

The following summarizes all experiments conducted on the investigated device systems.

Technologies					
Methods	a-Si	a-Si/μSi	CdTe	CZTSSe	CIGS
Short-term metastable	x	x	x	x	x
Changes in Pre-conditioning	x	-	x	-	-
Annealing at low temperature	x	-	-	-	-
Changes in Pretreatment <100 W/m^2	x	x	x	x	x
Changes in Pretreatment >300W/m^2	x	-	-	-	-
Pretreatment under Blue light	-	-	-	x	x
Pretreatment under Red light	-	-	-	x	x
Pretreatment under Green light	-	-	-	x	x
Impedance Spectroscopy	-	-	-	x	x

Tab. 4.1: Summary of the experiments on the various thin-film technologies.

Chapter 5

RESULTS

> *Users do not care about what is inside the box, as long as the box does what they need done.*
>
> — **Jef Raskin**
> about Human Computer Interfaces

5.1 Amorphous and micromorph technology

Technologies of the same amorphous silicon family can react differently in terms of metastability to external conditions. Various configurations of the a-Si:H layer in a PV cell structure can introduce changes in the performance parameters. Here, the effect of pretreatment (section 4.2) is performed on the a-Si:H and micromorph technologies.

5.1.1 Pretreatment

Samples from table 2.2 were selected to check the effect of light and temperature on metastabilities. The measurement of LS and DS-based pretreatment shows an evolution of the parameters of the electrical module V_{OC}, P_{MPP}, and FF with time. The relative variation of these parameters with time is shown for modules S1 (a-Si) and S9 (a-Si/μc-Si) from table 5.1 in figures 5.1 and 5.2, respectively. The data were normalized to the initial state of the modules prior to LS and DS. The horizontal time axis is logarithmic.

The variation in the electrical parameters of modules S1 and S9 at the end of each step of pretreatment, LS and DS, compared to the initial values, is summarized in Table 5.1. The short circuit current, I_{SC}, oscillated during the pretreatment at variable temperatures but remained constant at stable temperatures within the measurement resolution throughout the experiments.

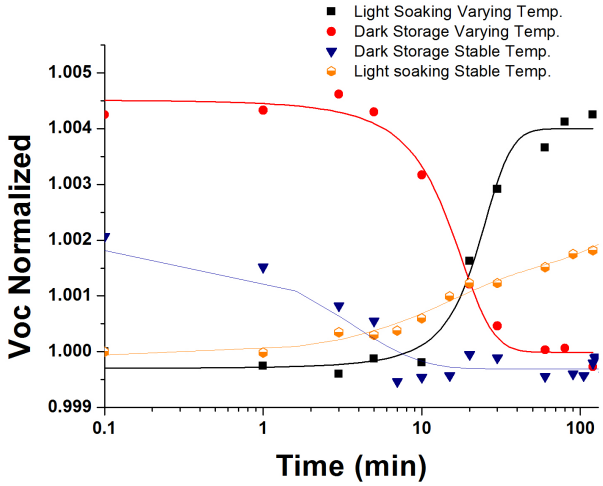

(a)

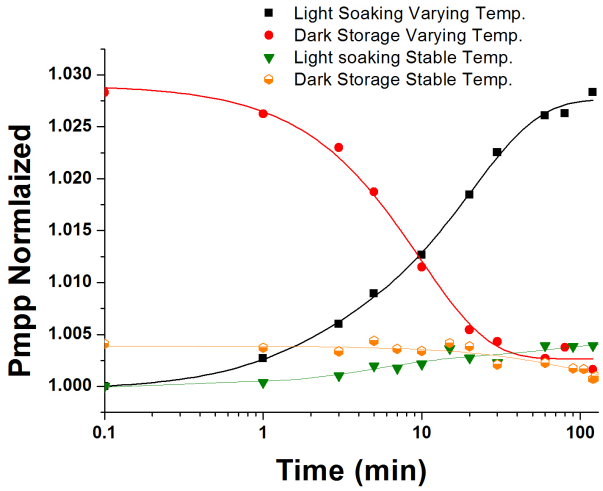

(b)

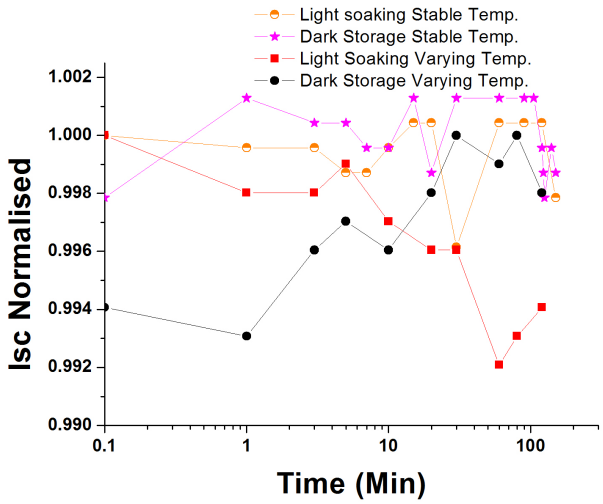

(c)

Fig. 5.1: Pretreatment behaviour during Light soaking and Dark storage, of sample S1 (a-Si) at variable temperature and at a stable temperature of 25.7°C respectively. (a) Shows the change in V_{OC}, (b) Shows the change in P_{MPP} and their best fit for the LS and DS data points, and (c) shows the change in I_{SC}. The lines are fit of τ LS and τ DS in P_{MPP} and V_{OC}.

Double junction a-Si (S1)

In Fig.5.1(b), the P_{MPP} of module S1 (operating at a variable temperature 25°C< T< 30°C) shows a significant change immediately after the beginning of light treatment, while V_{OC} in Fig.5.1(a) is stable in the first minutes. After about 10 min, V_{OC} begins to increase strongly, while the changes of FF and P_{MPP} continue to follow their monotonic trend. The FF showed saturation after an hour of LS. In contrast, during the first 10 minutes of illumination, V_{OC} remains stable and only increases rapidly for longer periods of light exposure, reaching a final value of +0.43 % after 120 minutes, although it continues to increase slowly. After approximately 1 hour of illumination, FF and P_{MPP} reached their final values of +2.83 % and +2.94 %, respectively, after 120 minutes. After 120 min, the LS treatment was terminated, and the DS period began. The plot of the time variation for the DS treatment of all three parameters in Fig. 5.2(a) and (b) appears fully reversible in the dark. The identical time scale τ = 120 minutes of this relaxation process suggests that it is based on the exact mechanism. All of the changes were attributed to originate from both temperature and irradiance.

For module S1 pretreatment operated at a stable temperature of (25.7 ±0.5)°C as depicted in Fig. 5.1 (a), V_{OC} and Fig. 5.1 (b), P_{MPP} shows a change immediately after the first minute of illumination, which indicates a strong dependence of both parameters on exposure to light, since the temperature was kept stable. In contrast, during the first 20 minutes of illumination, V_{OC} showed a fast increase in its value and only increased more slowly for longer exposure times to light, reaching a final value of +0.21% after 150 minutes. After the LS treatment, the DS was performed, showing a reversed evolution: V_{OC} decreased rapidly after the first 10 minutes in the dark and remained constant for the remainder of the measurement, yielding a final value of -0.23% after 150 minutes of DS. The evolution of P_{MPP} with continuous LS and DS follows the qualitative behavior of V_{OC}. The P_{MPP} increased by +0.41% during LS and then decreased during DS to -0.33%. It was seen to be further reducing towards its saturation point. The FF did not show any discernible pattern from the measured values. Here, the changes in electrical parameters were due to irradiance.

Multijunction a-Si/μSi (S9)

In Fig. 5.2(a-b) the 2 parameters, V_{OC}, P_{MPP} are plotted for module S9 (a-Si/μc-Si multijunction architecture device) in the same way like for S1 (Fig. 5.1a-b). Module S9 was also subjected to variable temperatures during pretreatment measurement. The time dependence of the performance parameters of this module differs considerably from the behavior of module S1 for both treatment periods.

During the LS period, all parameters remain almost constant for the first 10 min and then they exhibit a gradual decrease with time. Subsequently, V_{OC} and FF decrease significantly by -3.3% and -2.23% without reaching saturation after 2 hours. $P_{MPP}(t)$

appears to oscillate during LS (Fig.5.2b) due to the sudden surge in I_{SC}, reaching -1.64% at the end of LS.

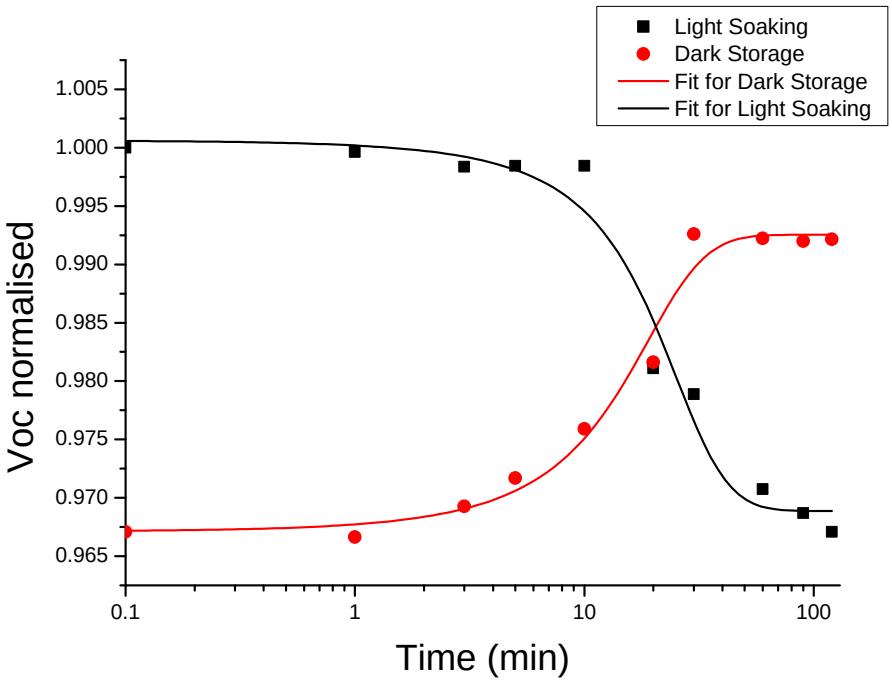

(a)

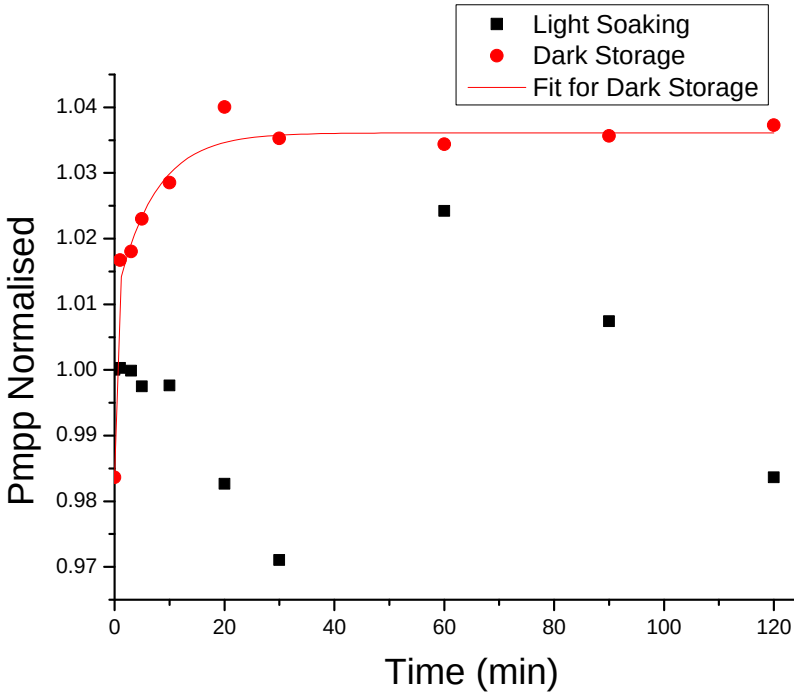

(b)

Fig. 5.2: Pretreatment behavior of sample S9 (a-Si/μSi) during light soaking and dark storage, where (a) shows the change in V_{OC} and (b) shows the change in P_{MPP}. The lines are fit of τ LS and τ DS.

In the dark, all three parameters shows a progressive recovery with time, but start to stabilize after 20 minutes. However, V_{OC} increase montonically during the storage time reaches saturation after 2 h,however the recovered level was below the initial start level of the light soaking. FF and P_{MPP} show a tendency to increase further by +1.24% and +5.45%.

Tab. 5.1: The absolute change in V_{OC} [V], P_{MPP} [W] and FF [%] and the relative change [%] to the previous state of the electrical parameters due to the pretreatment of the modules S1 with variable and stable temperature and S9 module with variable temperature are shown.

Modules	V_{OC}			P_{MPP}			$Fill factor$		
	Initial	*LS*	*DS*	*Initial*	*LS*	*DS*	*Initial*	*LS*	*DS*
Amorphous									
S1 Variable (absolute)	62.82	63.09	62.80	36.77	37.81	36.83	0.579	0.596	0.581
S1 Variable (relative %)		+0.43	-0.45		+2.83	-2.59		+2.94	-2.50
S1 Stable (absolute)	63.34	63.47	63.32	43.90	44.08	43.94	0.594	0.597	0.596
S1 Stable (relative %)		+0.21	-0.23		+0.41	-0.33		+0.47	-0.22
Micromorph									
S9 Variable (absolute)	159.47	154.23	158.22	131.20	129.01	136.09	0.701	0.685	0.694
S9 Variable (relative %)		-3.29	+2.59		-1.64	+5.45		-2.23	+1.24

5.1.2 Power rating before and after low-temperature annealing

Double junction a-Si (S6) Undergoing treatment in the climate chamber S6 (double junction a-Si) showed a significant change in P_{MPP} from 99.73 W to 102.97 W. In Figure 5.3 the change of the module's power output with time is presented. During the annealing at 70°C, the module was continuously exposed to white light with an irradiance of 830 W/m^2. The horizontal axis (time) of Figure 5.3 is scaled in exposure dose units of kWh/m^2 rather than in hours. A maximum was reached after 57 kWh/m^2 (the corresponding time is 69 h). Since the slight decrease in power during further exposure, up to 70 kWh/m^2, was less than 2% of the overall module power, it was considered stabilized and the annealing process was ended. A total gain in power output of +3% was observed during the transition from the initial degraded to the final stable state. The corresponding change in power can be considered as SW-based behavior. The curve was fitted using the sigmoid growth function.

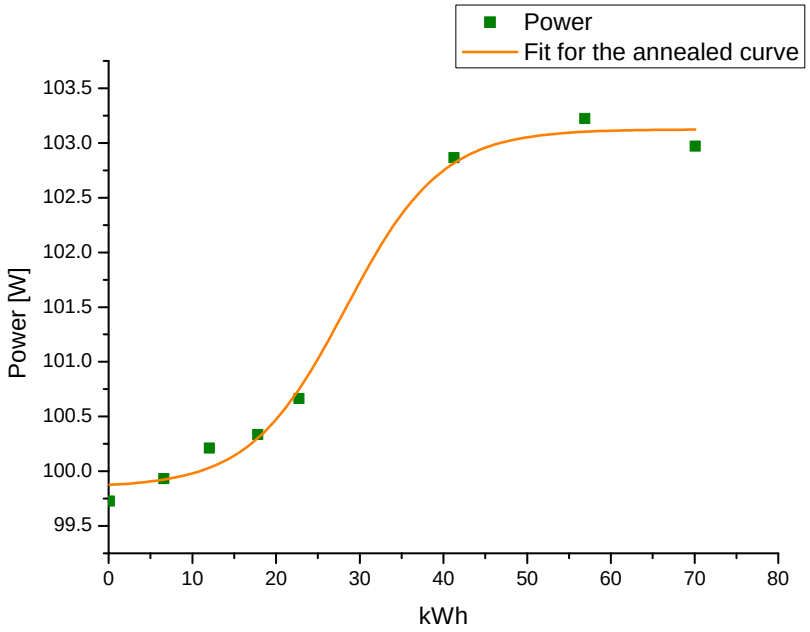

Fig. 5.3: Low-temperature annealing showing the stabilized power state of the sample S6; please note that the power shown here was measured at the STC conditions.

Before and after this indoor stabilization process, the module underwent an LS-DS procedure as described above. An STC power rating at low irradiance was performed for the degraded state of module S6 and in the stabilized, annealed state. The variation in electrical parameters (absolute and relative change) for the degraded and annealed states are tabulated in Table 5.2. The plots in Figure 5.4 refer to the measurements taken before the low-temperature annealing step, while those in Figure 5.5 plot the results after the annealing. The time-dependent variations are shown in Fig.5.4(a) and Fig. 5.5(a) for V_{OC}. Fig.5.4(b) and Fig. 5.5(b) show the P_{MPP} dependence. During the pretreatment experiment, a temperature offset of $+5°C$ was applied to the STC condition.

A significant change in P_{MPP} and V_{OC} from the degraded state to the low-temperature annealed state was observed for module S6. It showed a change in its absolute P_{MPP} from 99.73 W to 103.05 W under thermal and light treatment. As seen in figure 5.3, when the module underwent the thermal annealing with illumination at $\sim 830\,W/m^2$, an increase in P_{MPP} was observed after 57 kWh/m^2, which was confirmed to be in a stabilized annealed state after annealing it further till 70 kWh/m^2 (difference smaller than $\pm 2\%$).

During LS and DS, the change in V_{OC} and P_{MPP} with time for module S6 exhibits similar behavior to that observed for module S1 at variable temperatures.

However, the changes caused by the treatments are significantly larger than before the low-temperature process was applied. The change in P_{MPP} for the initially

Tab. 5.2: The absolute change in [V], [W], and [%] and relative change in the electrical parameters during pretreatment at variable temperatures of S6 module before and after annealing.

Modules	V_{OC}			P_{MPP}			$Fill factor$		
	$Initial$	LS	DS	$Initial$	LS	DS	$Initial$	LS	DS
a-Si S6									
Degraded (absolute)	23.88	23.99	23.84	99.73	101.91	99.44	0.602	0.604	0.599
Degraded (relative %)		+0.44	-0.63		+2.19	-2.43		+0.32	-0.61
Annealed (absolute)	24.02	24.09	24.06	103.05	103.828	103.55	0.611	0.612	0.612
Annealed (relative %)		+0.34	-0.18		+0.75	-0.27		+0.21	-0.02

degraded module is larger than 2% after the LS period and the DS period compared to after annealing. After annealing, the observed changes were well below 1% in both cases. Another difference was found between the degraded and annealed modules. During DS treatment, the degraded module reached final values for V_{OC} and P_{MPP} that were even lower than the initial values. In contrast, after stabilization, the final recorded values for V_{OC} and P_{MPP} were higher than the initial values. This observation deviates from the results of module S1, where the DS effect is reversible compared to the LS effect.

In the pretreatment, S6 shows an increase in electrical parameters under illumination and a recovery under storage in the dark. Before annealing, V_{OC} starts to rise immediately after the first minute of illumination, increasing to a relative change of +0.44%. The relaxation state during dark soaking was reached even below the initial starting point of LS. It was reached in 10 minutes with a relative change of -0.63%.

The P_{MPP} showed a relative increase of +2.19 % with LS. During DS the initial state was achieved after the first 10 minutes. The saturation was reached after 30 minutes of DS with a relative change in magnitude from the final point of LS by -2.43 %. The fill factor also showed a relative change in magnitude by +0.32 % during LS after 120 min but took longer to stabilize during the DS cycle at -0.61% after 120 minutes.

After annealing, the amplitude of the metastable effect on the module was significantly reduced, as shown in Fig. 5.5. The relative change in V_{OC} during the LS cycle was +0.34 % which relaxed during DS cycle by -0.18 %. The initial value of V_{OC} during the DS of the degraded module was reached within 10 minutes, but after annealing, the initial value could not be reached after DS. Similar characteristics were observed for P_{MPP}, showing a relative increase of +0.75 % during the LS cycle. However, during DS, it relaxes by -0.27 % from the final LS point. FF did not show an observable pattern in the relative change during LS and DS.

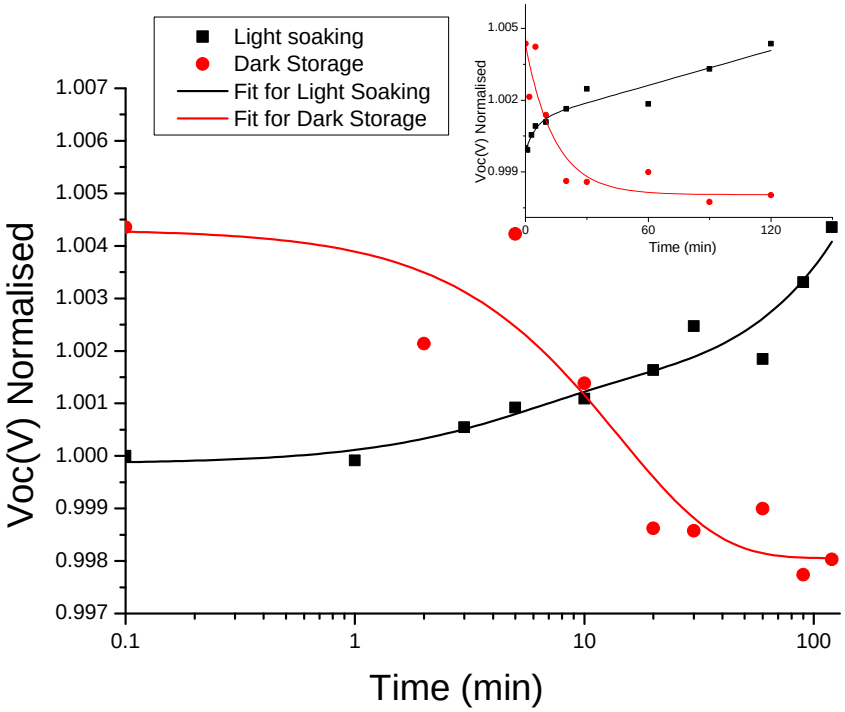

(a)

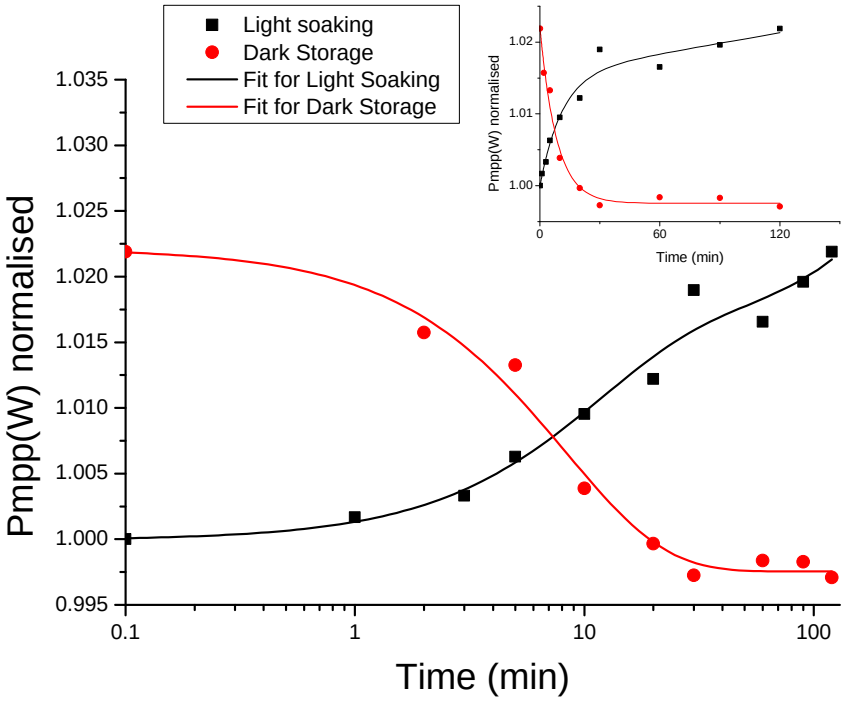

(b)

Fig. 5.4: Pretreatment results of S6 module at degraded state showing the V_{OC} and P_{MPP} behaviour during LS and DS at room temperature.

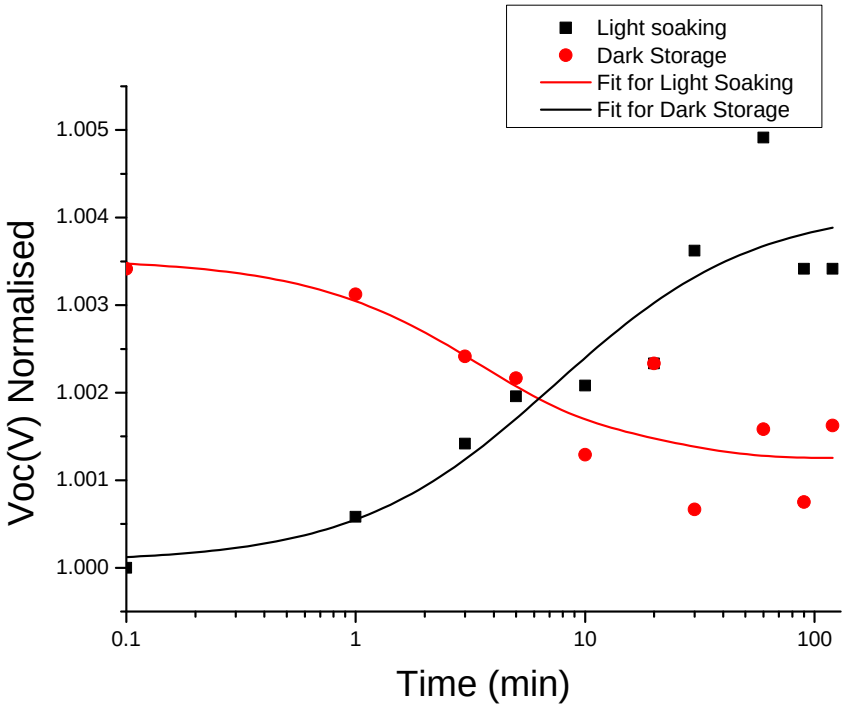

(a)

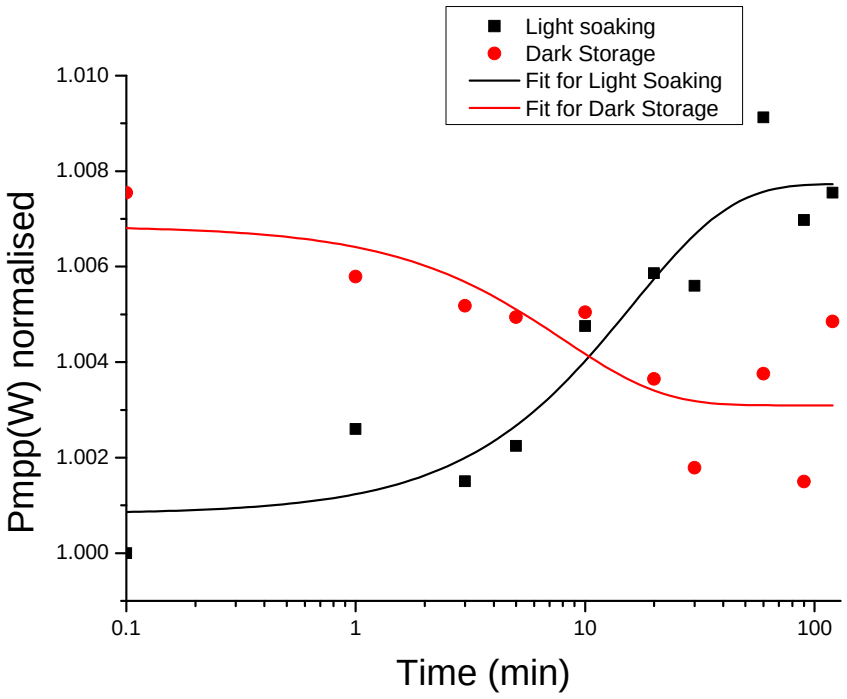

(b)

Fig. 5.5: Pretreatment results of S6 module at annealed state showing the V_{OC} and P_{MPP} behaviour during LS and DS at room temperature.

5.2 Annealing

Low-temperature annealing enables the investigation of the behavior and stability of a-Si modules. In an open field, a module is always exposed to illumination and temperature in a coupled way. In laboratory experiments, both effects are segregated:

- by analyzing SW under low irradiance, i.e,. suppressing the metastabilities,
- by dark annealing, i.e., light-induced defect formation,
- by a test experiment with initial annealing under illumination and subsequently in the dark, but at the same temperature.

5.2.1 Thermal Annealing

According to the procedure defined in section 4.4.4, dark annealing was performed at temperature steps of 60°C, 65°C, and 70°C. As the 2 modules S5 and S7 were selected for dark annealing, as referred in table 2.2. Figure 5.6 shows the power increase during all three passes. The black symbols represent the 60 °C run. The module has stabilized in the climatic chamber at 60 °C after approximately 553 hours. The power at the initial measuring point was 98.6 Wp. In order to obtain the stabilized final power of the run at a defined temperature, a fit function was applied to the performance profile, and the average final value was determined. The fit function applied in the 60 °C run is an exponential growth function, and the stabilized final value is 107.7 Wp (±0.2%), resulting in a performance gain of 9.1 Wp.

At 65 °C, the stabilized final value reached after about 635 hours in the climatic chamber is 111.7 Wp (± 0.2%), which results in a further increase in power of 4 Wp. For the 70 °C annealing cycle, a final stabilized power of 114.9 Wp (± 0.2%) was reached after about 920 hours. The performance increase from 65 °C to 70 °C is 3.2 Wp. Thus, the total increase over all three cycles is 16.3 Wp.

The changes in series resistances were small, as shown in figures 5.11 and 5.12 in the Arrhenius section, and were correlated with the power change in each annealing cycle.

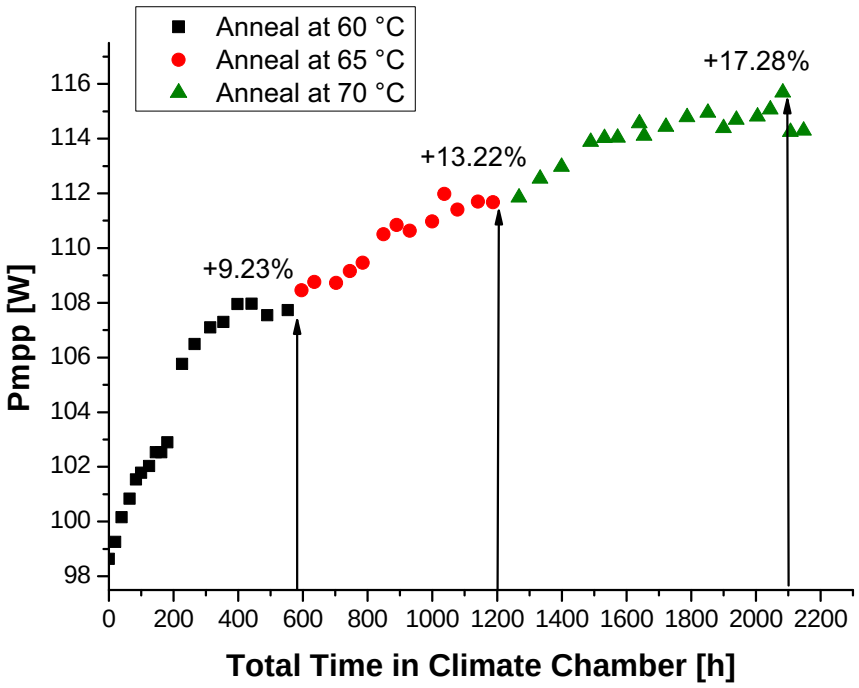

Fig. 5.6: Annealing of the S5 a-Si:H module at low temperature.

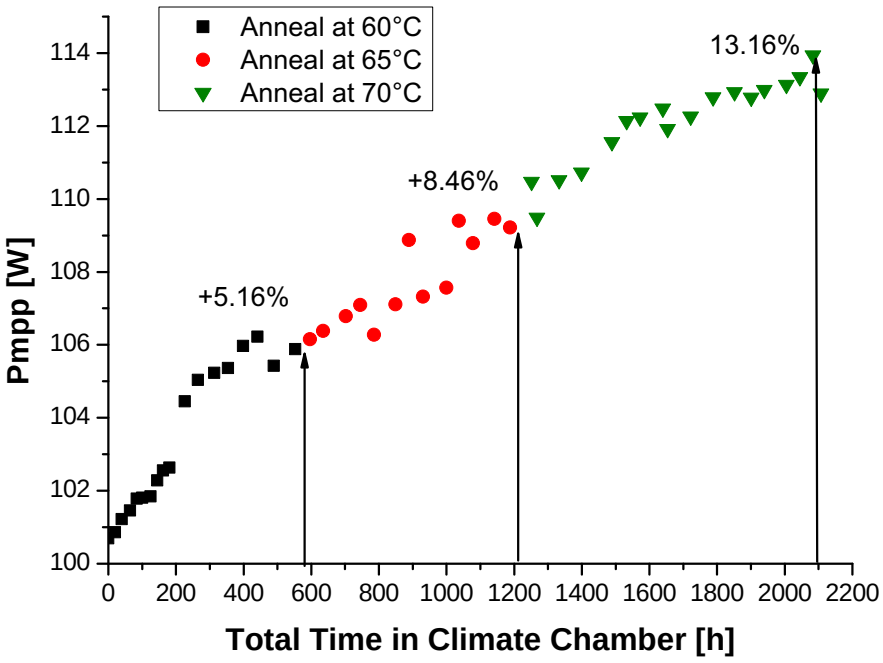

Fig. 5.7: Annealing of the S7 a-Si:H module at low temperature.

Module S7 shows a similar behavior under dark annealing as S5, as shown in figure 5.7. The module S7 has stabilized during the 60 °C run after 553 hours in the climatic chamber. It can be seen that the power of the first measuring point was 100.7 Wp. For this module, the same fit function was used for the 60 ° C data, which exhibited exponential growth. The average stable final value is 105.9 (±0.3%) Wp, resulting in a performance gain of 5.2 Wp. After about 635 hours in the climatic chamber at 65 °C, a stabilized final value of 109.1 Wp (± 0.3%) was obtained. The increase in power during the isothermal annealing step from 60°C to 65°C was 3.2 Wp. Possible causes for the strong fluctuations between 700 and 1100 h are given in chapter 4. The 70 °C run ended after about 920 hours. The stabilized final power was found to be 113.3 Wp (± 0.3%), resulting in a further increase in power of 4.2 Wp and an overall increase of 12.6 Wp.

5.2.2 Annealing under light and dark

In order to investigate the influence of illumination on the SW and reversed SW, the first annealing step was performed under illumination of 830 W/m^2 and at an elevated temperature of 65 °C as described in section 4.6.

In figure 5.8, the first part for about 550 h represents the 60 °C annealing. The module has stabilized after about 553 h starting at 98.6 (±0.2%)Watt peak (Wp) and finally stabilized at a value of 107.7Wp (±0.2%) of power. This results in a performance improvement of 9.1 W (9.2%). In the 65 °C cycle, the stabilized final value was reached after 635 h with 111.7 Wp (±0.2%), resulting in a further increase of 4 W (4%). At 70 °C the module finally reached 114.9Wp (±0.2%) after 920 h. The power increase from 65 °C to 70 °C cycle was 3.2 W (3.3%). Thus, the overall increase for three runs is 16.3 Wp, i.e., 16.5% from the degraded value. In Figure 5.8, the relative increase in power of the module is shown for each temperature step. All temperature steps lead to an increase in power. The initial power value after manufacturing (data sheet value of 116 Wp) was not reached.

The measurements showed that the module was not fully stabilized when annealed under illumination. This is because the ordering and disordering mechanisms driven by SW (illumination) and inverse SW (annealing) counteract each other. Therefore, the annealed state under illumination at 65°C is not the final stable state for this temperature. The final isothermal equilibrium is reached in dark annealing at 65°C at 107.7 Wp.

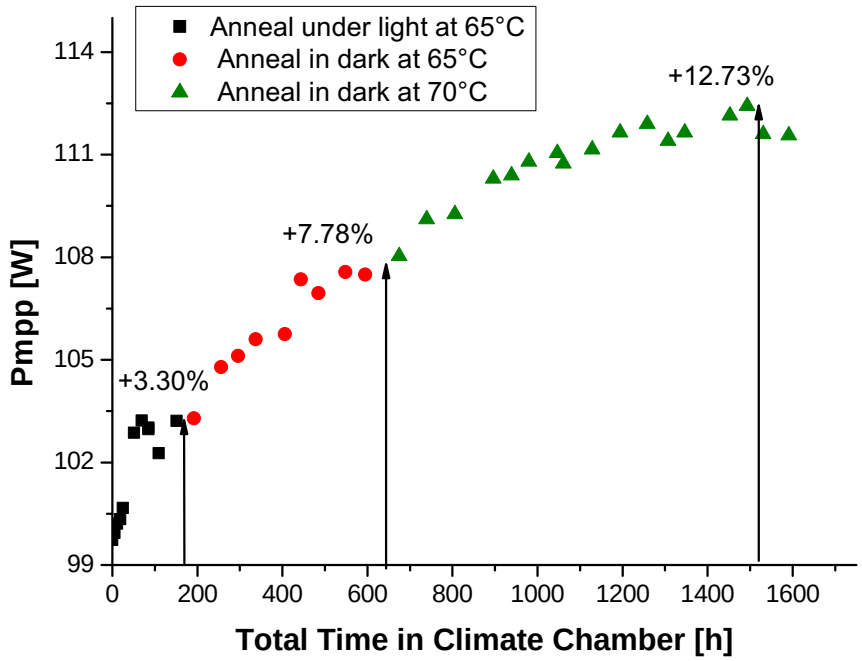

Fig. 5.8: Annealing of the S6 a-Si:H module at low temperature and illumination.

5.2.3 Pretreatment under high irradiance

A further step was to investigate the behavior of metastability under varying irradiance. The pretreatment of a-Si:H modules at high irradiance constituted only a LS cycle since it was conducted in a steady-state sun simulator. There, the DS cycle was not possible.

Double junction a-Si module (S6)

For this experiment, the module was placed in the static sun simulator. The I–V curves were measured in successive time intervals under constant illumination and stable temperature. After saturation was reached at a set illumination, the illumination level was changed, and the experiment was repeated. The measurement was performed at illumination levels of E = 300 W/m^2, 540 W/m^2 and 740 W/m^2, respectively. In addition, an I–V curve was measured under STC conditions before and after the pretreatment under high irradiance.

V_{OC} has shown a decrease in its trend during each LS cycle. When considering the 300 W/m^2 of LS the decrease was -1.7% from its initial point. Interestingly, the absolute value of V_{OC} at STC showed an increase from 24.396 V to 24.420 V after 300 W/m^2 LS. During 540 W/m^2 LS, the change was measured as -0.84% and the STC value as 24.352 V. Finally, at 740 W/m^2 LS, the change was -0.12%; the smallest compared to the previous two LS cycles at different irradiances, with a final STC value at 24.332 V.

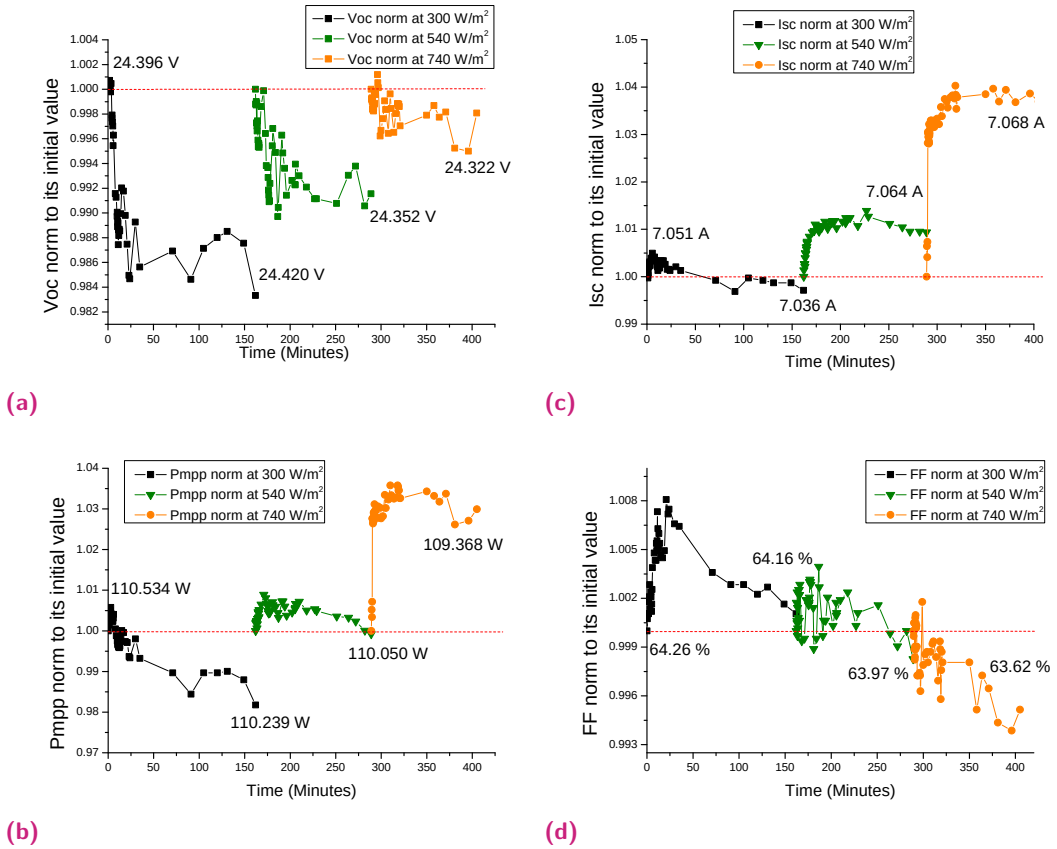

Fig. 5.9: Evolution of normalized (a) V_{OC}, (b) P_{MPP}, (c) I_{SC} and (d) FF for a-Si:H module S6 during the high irradiance light soaking at 300 W/m^2, 540 W/m^2 and 740 W/m^2.

P_{MPP} has shown a decrease during the 300 W/m^2 light soaking by -1.8%, while subjected to the 540 W/m^2 irradiance, it showed after 9 minutes of LS an increase of 0.8% and at the end of LS a decrease of -0.1% from its initial value. When the S6 module was irradiated with 740 W/m^2 LS, it showed a large increase of +2.4% during the first minute, and after 2 hours of LS, P_{MPP} increased to +2.65%. P_{MPP} also showed a decrease in its STC value due to the SW effect.

The change in each measurement was <0.1% and is then considered stable under illumination. The I_{SC} started to decrease after 1 hour of the LS at 300 W/m^2 and was reduced by -0.03% at the end. The STC value decreased from 7.051 A to 7.036 A. During LS at 540 W/m^2 and 740 W/m^2, an immediate increase in its amplitude was observed, and after approximately 10 minutes it became constant, reaching a final increase of +0.93% and +3.2%. The STC value reached after final 540 W/m^2 and 740 W/m^2 illuminations, was 7.064 A and 7.068 A, respectively.

The FF started to increase approximately by +0.8% during 24 minutes of LS at 300 W/m^2 and thereafter showed a decrease by $\pm$0.1% when LS was stopped after 162 minutes . The STC value of FF after 300 W/m^2 changed from 64.26% to 64.16%. For 540 W/m^2 and 740 W/m^2 LS, FF shows a decrease by -0.18% and - 0.5%,

respectively. The STC value after the completion of the 540 W/m^2 cycle was 63.97% and after 740 W/m^2 it was 63.62%.

Double junction a-Si module (S5)

The pretreatment procedure was the same as for the S6 module, with the STC measurement made after each LS cycle. The measurement at the end of each pretreatment cycle was added to the graph, allowing for comparison of the effect of increasing illumination across consecutive cycles.

The V_{OC} during 300 W/m^2 illumination started to increase after 17.5 minutes and afterward decreased to end at +0.11%. By comparing the STC value before and after LS, the V_{OC} showed a decrease from 24.146 V to 24.051 V. During 540 W/m^2 LS, after 31 minutes, the V_{OC} stabilized. At 740 W/m^2 LS, the V_{OC} started to increase steadily until 11 minutes of exposure by +0.41% and later decreased and became stable at 0.14% after 126 minutes. The final STC value after the 540 W/m^2 LS reached 23.962 V, and after 740 W/m^2 LS it reached 23.973 V.

The FF showed a fluctuating value for all LS cycles of 300 W/m^2, 540 W/m^2, and 740 W/m^2 but a long-term declining trend. For 300 W/m^2 LS the FF increased during the first 11.5 minutes by 0.49% with some fluctuation and then decreased to 0.17% after 117 minutes. At 540 W/m LS, the highest increase was observed after 1.6 minutes of exposure by 0.15%, but a decrease by -0.58% after 126 minutes of LS. Considering the 740 W/m^2 LS, the decrease in FF was much higher in amplitude as compared to the other irradiations. After 29 minutes, the FF decreased by -0.71%, and until the end of the LS cycle after 126 minutes, the decrease was -0.74%.

The I_{SC} at 300 W/m^2 LS showed a decrease from the start with intermittent jumps between exposures. The overall resulting decrease was -0.53%. During LS at 540 W/m^2, I_{SC} increased steadily and reached +1.08% at 22 minutes of exposure. Thereafter, I_{SC} became much slower in response and finished at 126 minutes by +1.24%. The LS at 740 W/m^2 showed a similar response as the one at 540 W/m^2 irradiance; a steady increase for 23 minutes, reaching +1.34%, then a sudden increase of +1.6%, followed by a relaxation to the final value of +1.1% after 126 minutes. I_{SC} showed a small change after 300 W/m^2 LS from 6.869 A to 6.871 A. At 540 W/m^2 illumination, it showed an increase and reached 6.095 A, but decreased after 740 W/m^2 LS reaching 6.878 A.

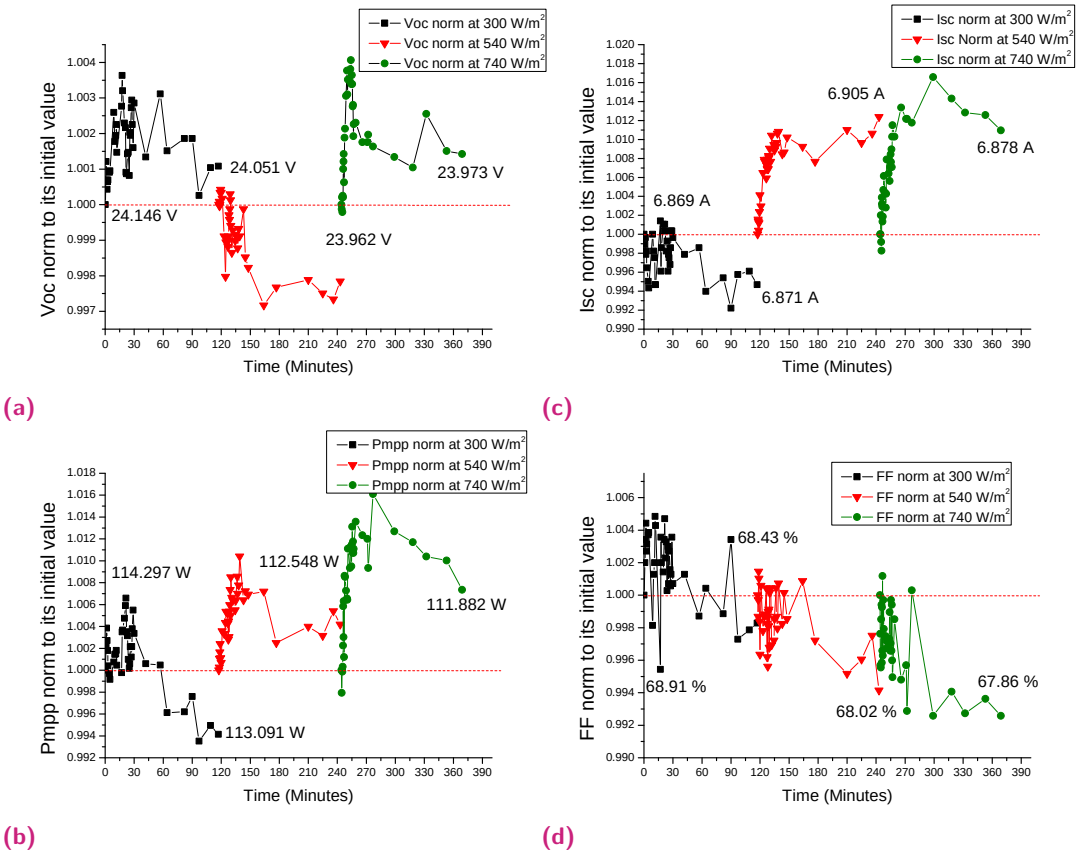

Fig. 5.10: Evolution of normalized (a) V_{OC}, (b) I_{SC}, (c) P_{MPP}, and (d) FF for a-Si:H module S5 during the high irradiance light soaking at 300 W/m^2, 540 W/m^2 and 740 W/m^2.

Also, the P_{MPP} curve at 300 W/m^2 shows an increase for 11.5 minutes by +0.18% and then a decrease reaching a final value of -0.6 %. The STC value before 300 W/m^2 was 114.297 W and after the pretreatment, it reached 113.091 W. For 540 W/m^2 LS, P_{MPP} increased for 22 minutes by + 1.04 %, and then showed a decrease along with a slow response until the end of LS after 126 minutes, reaching -0.42%. LS at 740 W/m^2 shows a similar response as at 540 W/m^2, with an increase for the first 13 minutes by -1.36% and a subsequent decrease until the end of LS by -0.73%. The STC value change after 540 W/m^2 and 740 W/m^2 illumination was 112.548 W to 111.882 W.

5.2.4 Time constant and thermal activation in low temperature annealing

Since metastable changes and the SW effect are thermally activated processes, it was investigated whether the process follows an Arrhenius behavior. The detection of the thermally activated behavior of the annealing process on the microscopic scale via an Arrhenius behavior would be an important indication. The Arrhenius model describes a particular temperature dependence with the following equation

$$y = A_1 e^{(-x/\tau)} + y_0, \tag{5.1}$$

where y is the measured value, τ the decay-time constant , A is the amplitude, and y_0 is the initial value of y.

In this case, the increase in power ΔP and voltage ΔV , more specifically, the difference in power or voltage, was treated as a parameter dependent on thermally activated defects. The residual resistivity of the annealed modules was analyzed to extract their activation energies during the respective annealing steps. The following graph of series resistances during the annealing is fitted to extract the time constant τ for each temperature.

During the low-temperature annealing of samples S5 and S7, the series resistance was recorded at each annealing cycle. The complete annealing procedure was conducted over a span for 3 months for the both PV modules. The time constant τ decreases as the samples are subjected to higher temperatures. Here, only two modules, S5 and S7, are reported in the figures 5.11 and 5.12.

For both modules S5 and S7, the temperature-dependent τ behavior was similar at each annealing temperature. The series resistance started relatively high, but decayed slowly over each annealing cycle. Sample S5 revealed time constants from the fits to equation (5.1) of 284 hours at the 60 °C, 217 hours at 65 °C, and 178 hours at 70 °C. Sample S7 gave time constants of 295 hours at 60 °C, 213 hours at 65 °C, and 164 at 70 °C. The results are tabulated in table 5.3.

Tab. 5.3: Time constants extracted from the fitting of the series resistance at each individual temperature.

Sample	**τ at 60°C**	**τ at 65°C**	**τ at 70°C**
Module S5	284.0	217.5	178.0
Module S7	295.7	213.0	164.5

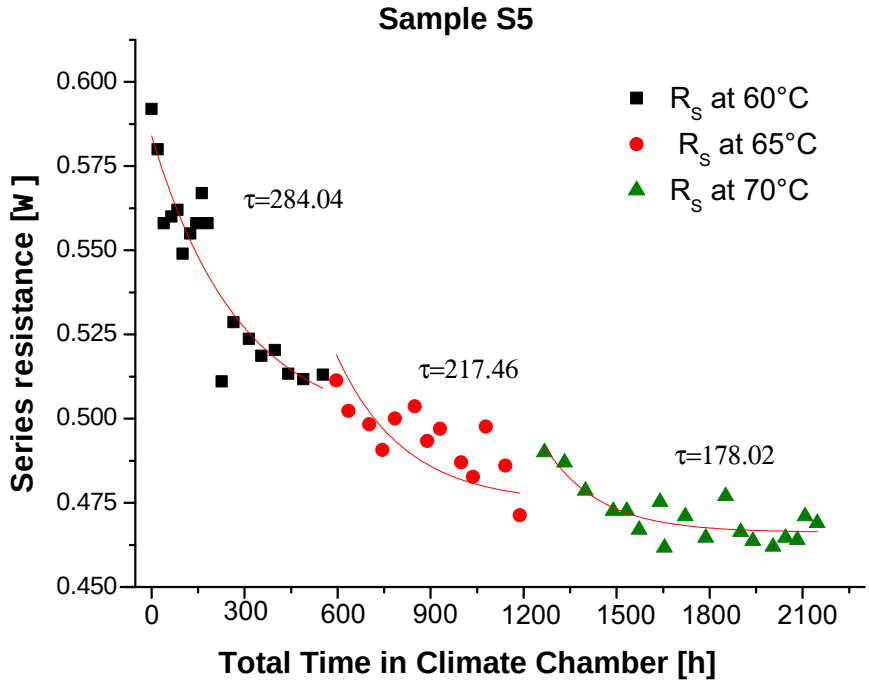

Fig. 5.11: Time constant in hours at each annealing step of the module S5.

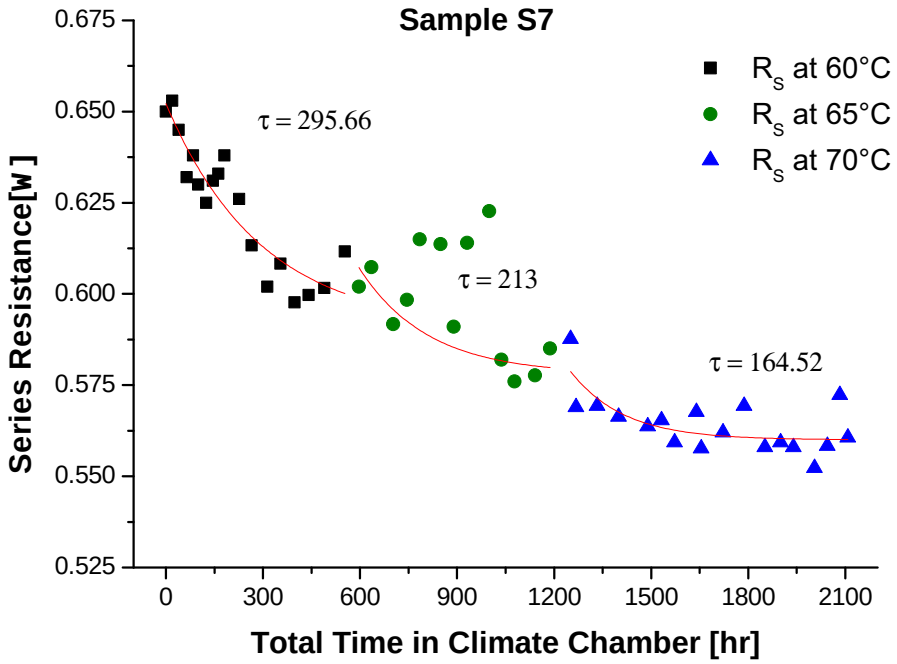

Fig. 5.12: Time constant in hours at each annealing step of the module S7.

5.3 CdTe Pretreatment

To perform the pretreatment, all field-aged CdTe modules were carefully selected based on their level of degradation. All modules were kept at an equilibrium temperature, with an overall variation in temperature of around ± 1 K throughout the pretreatment experiment. To improve the accuracy of the measured data, a spectral mismatch factor was applied based on precise outdoor measurements. The modules were operated at an outdoor facility and then treated in the lab through bias preconditioning before being stored in the dark for several days. The modules used for the experiment were in varying degrees of degradation, that is, loss of power from their nominal power. The results show the initial state of degradation, followed by the preconditioning procedure, and finally, after storage of the modules in the dark.

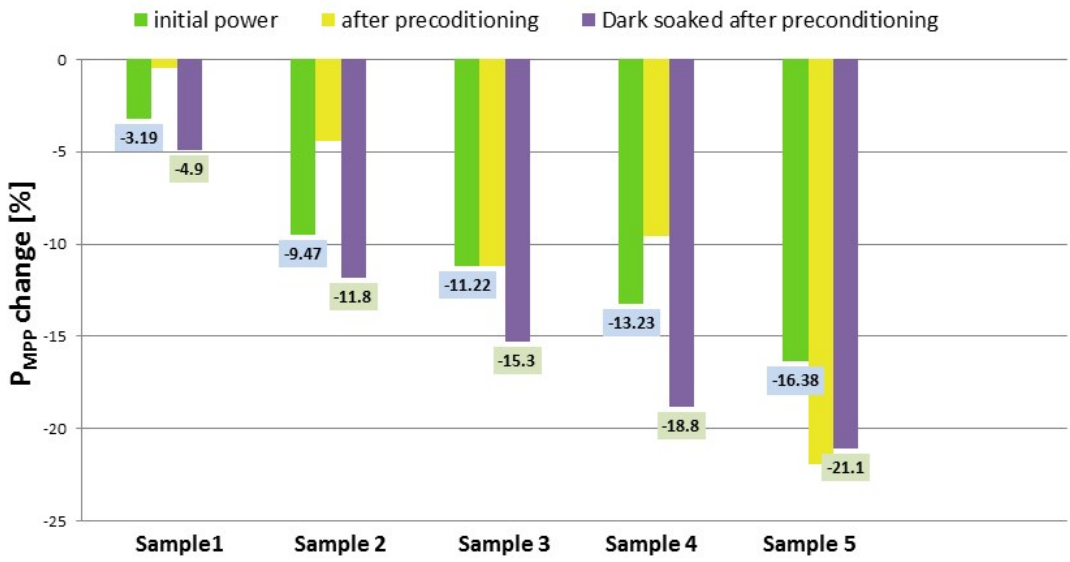

Fig. 5.13: Change in performance of the CdTe modules before and after preconditioning (stabilization).

This study was conducted on several standard commercial CdTe modules that had been mounted outdoors for several years, as well as a module fresh from a facility. Various outdoor-mounted modules with an increasing degree of degradation (ranging from 21% to 4.5% below the labeled nominal power) exhibited metastable changes in their electric parameters over time [6,7].

A low-intensity light soaking procedure, as explained in section 'Theory', was performed to observe a change in terms of short-term metastabilities, which influences the standard power rating procedure. The variation in power-rating results was investigated for already preconditioned modules with illumination and an unstabilized module (without preconditioning), followed by illumination.

This study focused on the influence of the degradation level on the power rating and metastable behavior of the CdTe modules. Modules of different degradation levels were first power-rated and then treated according to the newly proposed alternative preconditioning procedure, followed by a second power rating. Finally, after a storage period of a month, the power rating procedure was repeated. After dark storage, a metastable behavior was investigated. The standard procedure for quality testing of the modules requires one to follow certain guidelines. One of them is to measure the I–V curve at STC (standard test conditions). It is the measurement of a module at 1000 W/m^2, $25\,^{\circ}\mathrm{C}$ and 1.5 AM (Air Mass), using a AAA-type pulsed solar simulator.

A series of treatments was performed on 5 samples, except the unstabilized module (in this case, only pretreatment was carried out).

1. STC measurement,
2. Preconditioning according to the new IEC procedure,
3. STC measurement after pre-conditioning,
4. Pretreatment after a month of storage in the dark.

To determine the influence of short metastable effects on power rating, a pretreatment procedure was followed. In this pretreatment, the modules were exposed to light of approximately 50 W/m^2 for 2 to 2.5 hours; subsequently, the modules were relaxed by storing them in darkness. All modules were operated at open-circuit conditions while illuminated. All modules were maintained at an equilibrium temperature, with an overall temperature variation of around ± 1 K during the entire experiment. During the period of illumination and dark storage, the modules were successively characterized according to the standard test conditions (STC). The intervals of measurements were 1, 2, 2, 5, 10, 15, 15, 15, ... (in minutes) for both light and dark soaking. To improve the accuracy of the measurement, a spectral mismatch factor was applied based on a precise outdoor measurement. The translation of the I–V curve was carried out according to the IEC 60891 correction procedures to obtain the power rating under the STC conditions [9].

The modules were treated according to steps 1 to 4 as described in section 2. The modules used for the experiments were in varying degrees of degradation. The results of the power rating at STC for the steps 1 to 3 as described in the Methodology section 2, are presented in table 5.4.

The initial degradation values of samples 1 to 5 ranged from -3.19% to -16.38%, but after the application of the preconditioning procedure, samples 1 to 4 showed a reduction in the degradation level from -0.44% to -9.57%; only sample 5 showed an increase in its degradation level from -16.38% to -21.91%. After a month of dark storage, the samples exhibited further degradation, decreasing from -4.99% to -25.95% compared to their initial level. Interestingly, right before pretreatment, the

modules showed an additional slight change in their degradation level from -4.62% to -22.11%. It is clear from the results that the modules were not stable initially, nor were they after preconditioning or dark storage. They showed an increase in the level of degradation in open-circuit voltage, fill factor, and nominal power. A decrease in performance and high susceptibility to light soaking were observed, accompanied by significant metastability with a short time constant and dark relaxation with a longer time constant.

Samples	Initial	After preconditioning	Dark storage	PT
Sample 1	-3.19%	-0.44%	-4.99%	-4.62%
Sample 2	-9.47%	-4.4%	-9.75%	-9.72%
Sample 3	-11.22%	-11.2%	-15.32%	-15.90%
Sample 4	-13.23%	-9.57%	-18.87%	-16.03%
Sample 5	-16.38%	-21.91%	-25.95%	-22.11%

Tab. 5.4: Relative change in nominal power of the modules procured from the field, after applying the new preconditioning procedure, followed by storage of the modules in darkness and initial measurement during pretreatment (PT).

5.3.1 Pretreatment behavior of an unstabilized module

In figure 5.14, a pretreatment experiment of an unstabilized module (newly manufactured) is presented. During the first minutes of light soaking, an increase in the V_{OC} by +0.6% and in P_{MPP} by +1.5% was observed. Afterwards, a saturation in the effect was seen. The reverse behavior was observed during the follow-up dark storage for 13 hours, where P_{MPP} and V_{OC} approximately reached their initial values. A change in fill factor was also observed, amounting to +1.5%. This seems to relax at a much lower rate than that of degraded modules. The cause may be attributed to charge-trapping sites in CdTe.

In figure 5.14, a change in the pretreatment behavior can be seen for two ranges. The evolution of module performance, starting from a completely darkened state, differs from that during periods of illumination lasting longer than 4 minutes. The change in electrical characteristics is assumed to be triggered solely by the light-induced effect, as a stable low temperature (27.5 °C) is ensured to eliminate any thermally activated effect. Mostly, changes were observed in V_{OC}, FF and R_S and accordingly in P_{MPP}. No changes were observed in I_{SC}. This indicates that V_{OC} and P_{MPP} exhibit different time evolution slopes, initially increasing for $t < 4$ min and then decreasing for $t > 4$ min, before saturating.

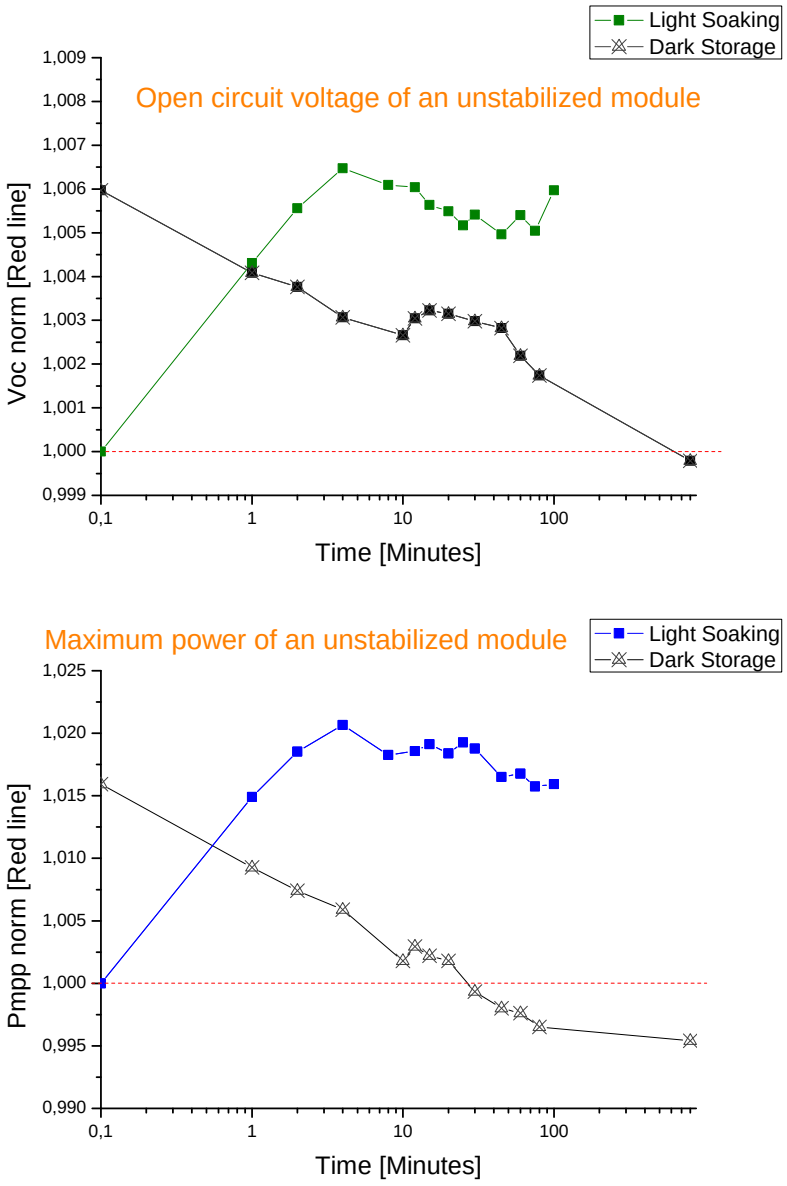

Fig. 5.14: Evolution of normalized V_{OC} and P_{MPP} for an unstabilized CdTe module during the light soaking and dark storage.

Then, in dark storage, the values monotonically decrease. While $V_{OC\ final}$ relaxes to $V_{OC\ initial}$, $P_{MPP\ final}$ becomes smaller than $P_{MPP\ initial}$.

Furthermore, the characteristics of the time dependence of the electric parameters (mainly V_{OC}) and their amplitude both showed a strong dependence on the degradation level. The modules also indicate that they are not saturated (stabilized) in the field, nor after step 2. The results on a fresh module, as shown in Figure 5.14, also demonstrate that this is true for a nondegraded module.

All field-installed modules showed a nonmonotonic behavior under the pretreatment procedure, different from the unstabilized module, which was not subjected to

any external treatment or degradation. All the degraded modules show the same behavior in terms of temporal evolution under light and dark soaking. The change in magnitude of electrical parameters during light and dark soaking is shown in table 5.5.

Samples	V^m_{OC} - V^i_{OC} [V]	V^f_{OC} - V^i_{OC} [V]	P^m_{MPP} - P^i_{MPP} [W]	P^f_{MPP} - P^i_{MPP} [W]
Sample 1	0.506	0.269	1.12	0.65
Sample 2	0.663	0.213	2.289	1.221
Sample 3	0.229	0.112	1.145	1.149
Sample 4	0.701	0.422	2.579	1.664
Sample 5	0.173	-0.102	0.126	0.229

Tab. 5.5: Amplitude change in open circuit voltage and power after light soaking and dark storage of degraded samples.
V^m_{OC} : Maximum reached point of V_{OC}
V^i_{OC} : Initial starting point of V_{OC}
V^f_{OC} : Final reached point of V_{OC}
P^m_{MPP} : Maximum reached point of P_{MPP}
P^i_{MPP} : Initial starting point of P_{MPP}
P^f_{MPP} : Final reached point of P_{MPP}

5.3.2 General trend observed on 4 samples

Samples 1 to 4 exhibited a similar evolution in behavior over time, accompanied by an increase in the magnitude of their metastabilities, which was proportional to their degree of degradation. This excludes the heavily degraded sample 5 which showed the opposite behavior. During the light and dark soaking of the pretreatment cycle, a substantial change in the V_{OC} amplitude was observed; see figure 5.15 (samples 1-4). For most studies, the amplitude of the metastabilities is proportional to the rate of degradation. Nevertheless, above a certain value of degradation, this correlation breaks down; most likely due to a high amount of volume defects.

As a general rule, it holds: $\Delta PT_i \propto$ Degradation,
where ΔPT_i is the change after pretreatment and i = V_{OC}, I_{SC}, FF and P_{MPP}.

During the pretreatment cycle, all modules exhibited an increase in V_{OC} and P_{MPP} within the first 2 minutes of light soaking, followed by a negative slope thereafter. Most of the modules did not return to their initial starting point during the dark storage period. An interesting effect was seen for the majority of modules when held in the dark for relaxation immediately after illumination.

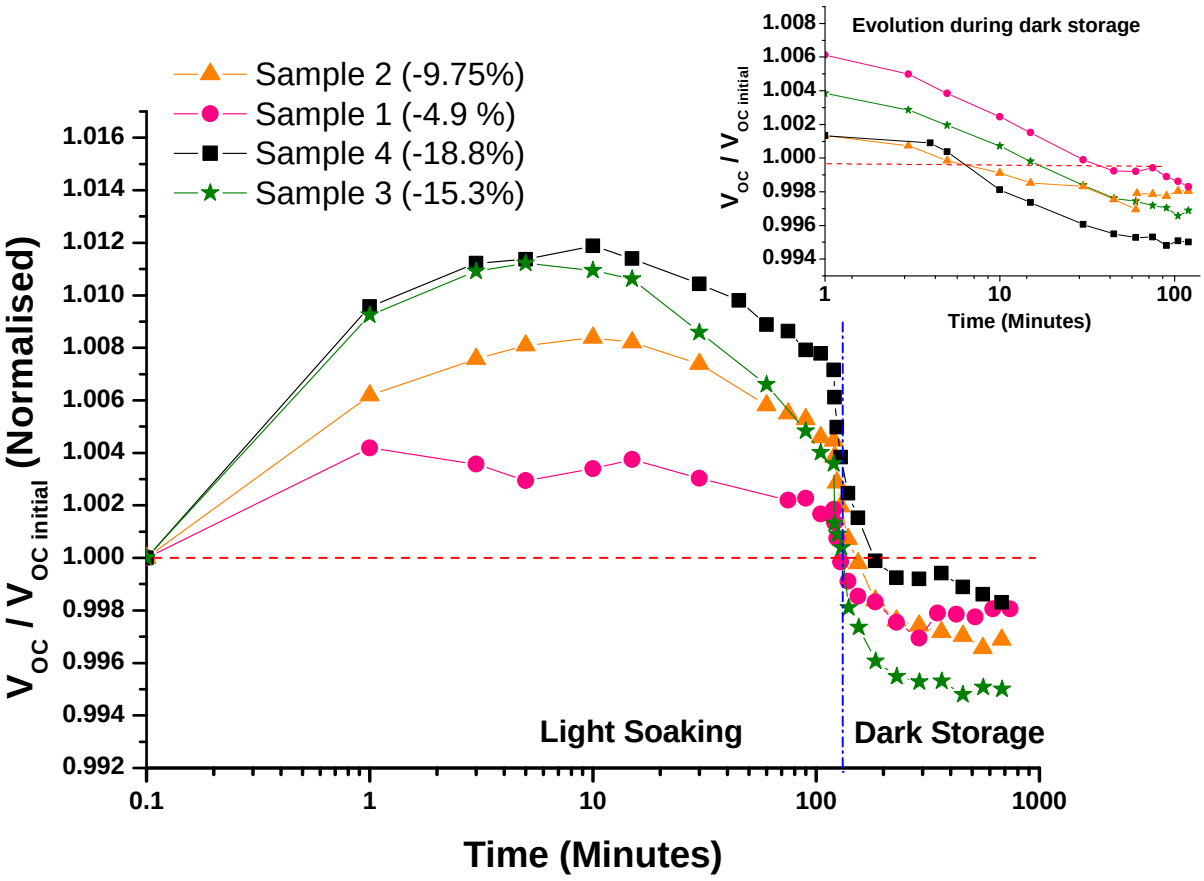

Fig. 5.15: Change in V_{OC} pretreatment amplitude of samples 1 to 4; the inset shows the similar slope of relaxation during dark storage in all samples

Both V_{OC} and P_{MPP} decrease, but the dark-storage curve of V_{OC} relaxes to a saturation level below its initial state. For P_{MPP}, however, the dark-storage curve saturates above its initial value before light soaking, as shown in figure 5.16.

It is clear from the results that the modules were not stable initially, nor were they after preconditioning or dark storage. They showed an increase in the level of degradation in open-circuit voltage, fill factor, and nominal power. This decrease in performance and high susceptibility to light soaking is characterized by a much higher metastable amplitude and a small time constant, as well as dark relaxation with a higher time constant. All field-installed modules showed nonmonotonic behavior under the pretreatment procedure, different from the unstabilized module, which was not subjected to any external treatment or degradation. All degraded modules exhibit redundant patterns, which are time-dependent under both light and dark soaking conditions. Within these redundant patterns, inconsistent behavior was observed in electrical parameters, particularly with light and dark soaking. The change in magnitude of electrical parameters during light and dark soaking is shown in table 5.5.

5.3.3 Pretreatment behavior of one sample with -15.9% degradation

The experimental results for the module with a degradation of -15.9% are shown in figure 5.16. The values in the graphs were normalized to the initial measurement point of the pretreatment cycle. In V_{OC} under light soaking, there was an increase of +1.2% that relaxes to -0.5% during dark storage below its initial measured value. P_{MPP} increased under illumination after 1 minute to a maximum of 3.5% above its initial value after pretreatment of 4 minutes. After reaching maximum, P_{MPP} again decreased under constant illumination to approximately 2% above the initial value of the illumination experiment.

In the dark soaking cycle shown in figure 5.16, the decrease continued, but with a different slope. The final saturation point was reached after 20 minutes of dark storage with -0.5% below the initial starting point of the light-soaking experiment. The change in P_{MPP} is the result of the change in the fill factor (FF) and V_{OC}. The FF amplitude increased by 2.5%. Other samples showed similar correlations, where sample 4 with -18.8% initial degradation exhibited the most substantial increase compared to sample 1 with -4.62% degradation. The maximum values for P_{MPP} and V_{OC} during light soaking were found to increase with decreasing module quality (see figure 5.15).

5.3.4 Pretreatment behavior of one sample with -22.11% degradation

In sample 5, power recovery was observed after light soaking from its initial degradation value -22.11% to -20.46%. A direct correlation of a reversible trend in the pretreatment of the highest degraded module of -22.11% in P_{MPP} is shown in figure 5.17. The module reached the highest metastable state during light soaking of +2.5%, followed then by a sharp negative slope and reverted back to almost its initial value. During the subsequent dark storage cycle, an increase to the previous maximum of +2.5% was observed.

An interesting finding was made when this metastable behavior in the degraded modules was compared with the results for the unstabilized module, shown in figure 5.14. In V_{OC} during light soaking, an increase of +0.6% occurred after a few minutes, and then a saturation occurred.

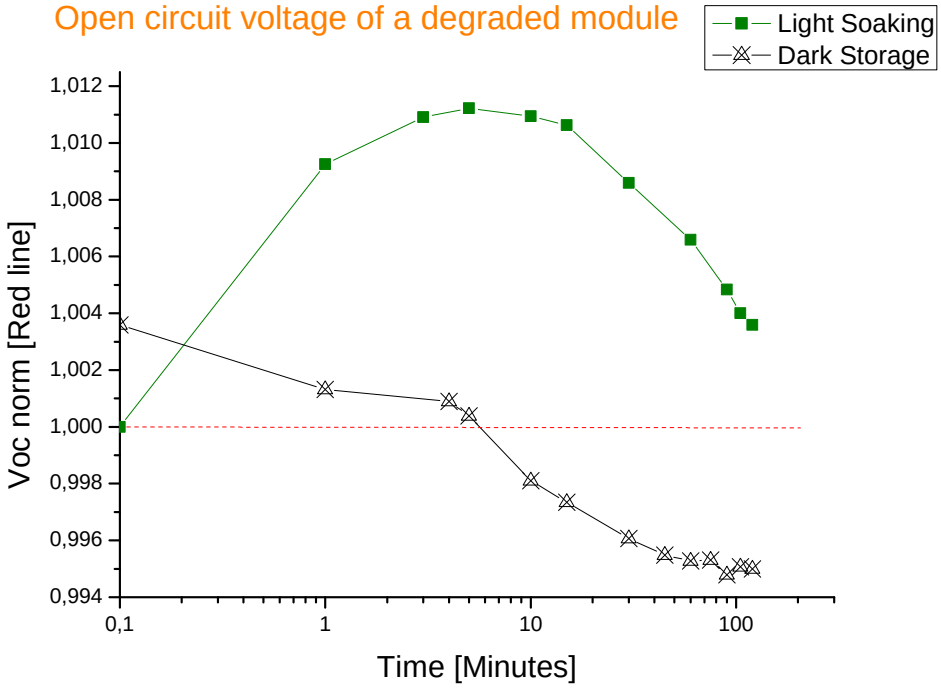

(a)

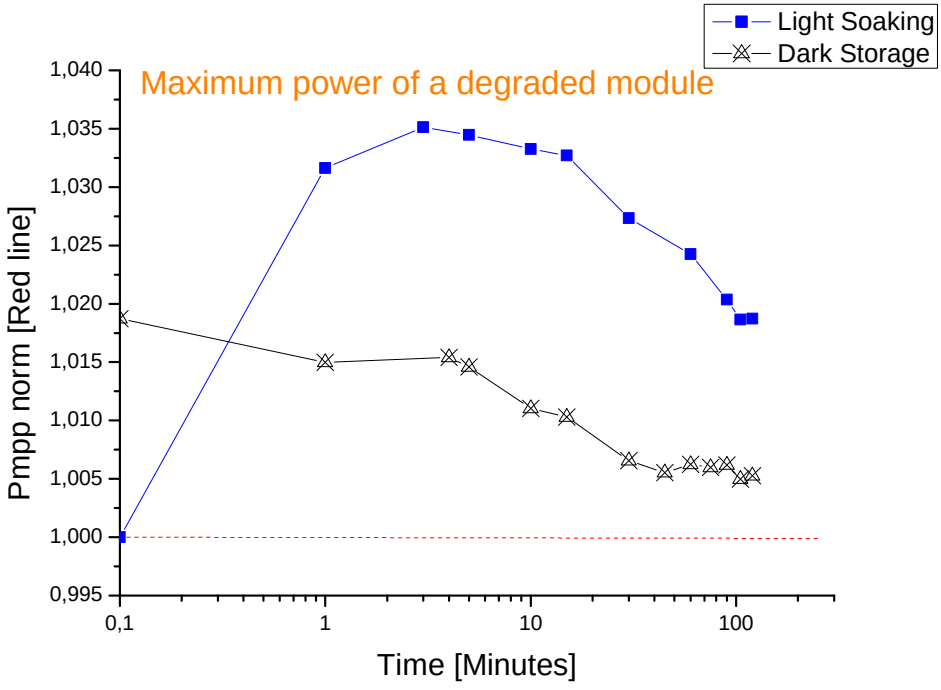

(b)

Fig. 5.16: Evolution of normalized V_{OC} and P_{MPP} for -15.9% degraded module during the light soaking and dark storage.

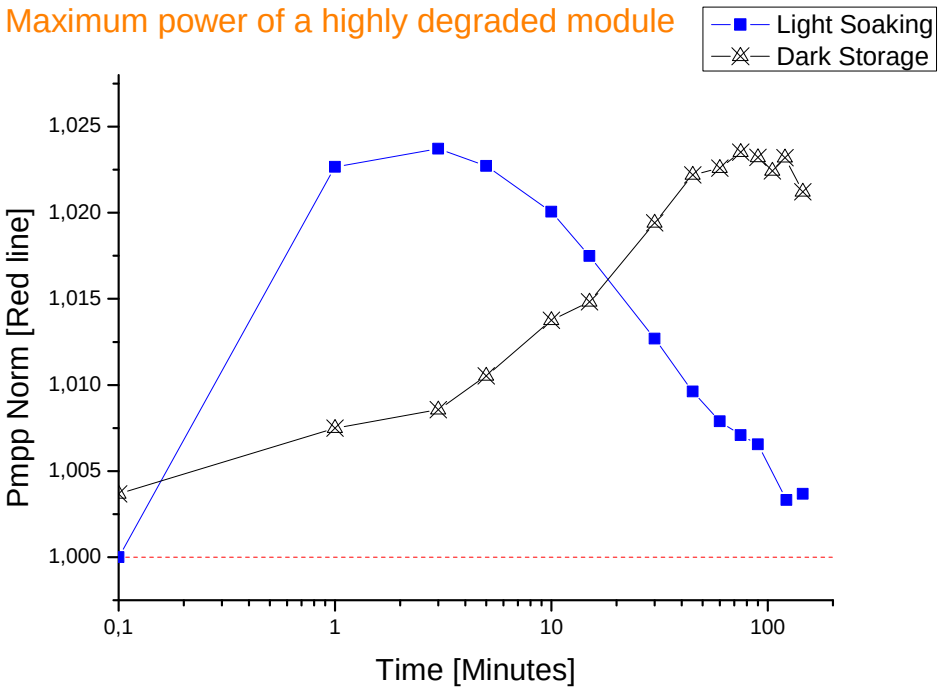

Fig. 5.17: Change in P_{MPP} pretreatment amplitude of sample 5 with highest degradation; the lines are guides to the eyes.

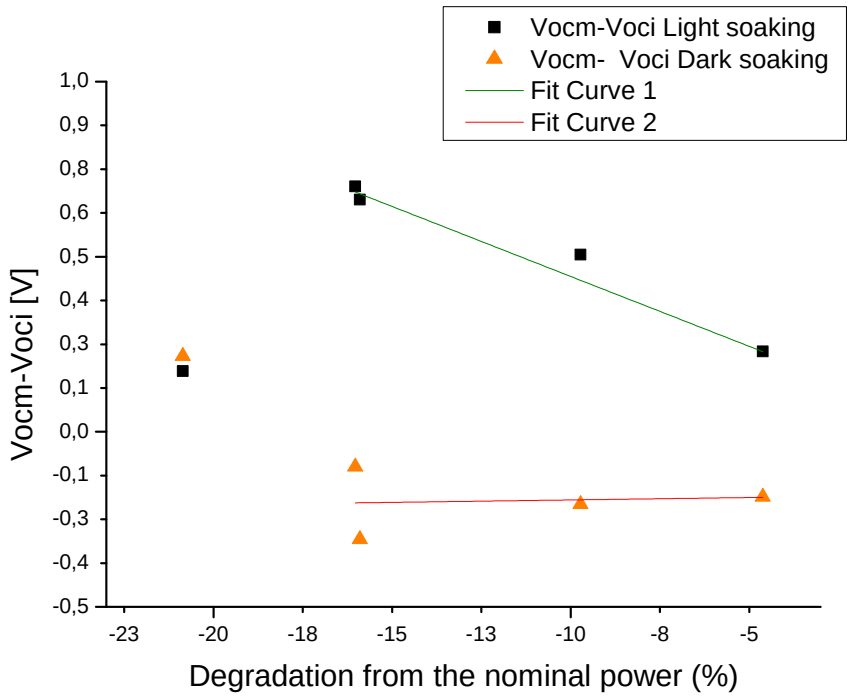

Fig. 5.18: Change in open-circuit voltage pretreatment amplitude in ascending order of degradation.

During dark storage, V_{OC} immediately started to decrease, and after 13 hours, V_{OC} relaxed to its initial measured state. P_{MPP} increased under illumination immediately after 5 minutes to a maximum of +1.5% above its initial value of the pretreatment and showed a saturation effect. However, during dark storage, P_{MPP} decreased and ended well below its initial measured point.

The measurements reveal that the higher the amount of degradation (in terms of deviation from its nominal power) of the modules, the higher is the degree of metastable behavior, as summarized in figure 5.18.

5.3.5 Degradation dependence

An increase in the pretreatment amplitude correlates with increasing degradation values, as shown in figure 5.18 for V_{OC}, depicting the maximum change during pretreatment versus the degradation level. Only sample 5 with the highest degradation showed a deviation from this correlation during pretreatment, i.e., reverting to its initial state of V_{OC} and P_{MPP} after storage in the dark. For degradation levels exceeding a certain threshold, this is no longer true. A similar behavior was already reported in CIGS [25] [42].

The increase in metastabilities with the level of degradation shows that the level of metastabilities is correlated with the level of defects within the material. The module with the highest defect level caused the metastabilities to reach a lower level than expected. This also shows that after a certain amount of microscopic defects, such as shunts, are introduced into the system, the metastable effect breaks down.

Typically, in an experiment investigating metastabilities, illumination changes a module from equilibrium towards a metastable state, while dark storage allows it to relax toward equilibrium [25]. Here, the initial value is already in a non-equilibrium state. This clearly indicates that the bias-based preconditioning procedure is insufficient to ensure a stable and reproducible power rating. This can be easily seen by the fact that sample 6 (reference without bias) exhibits normal metastable behavior. It is interesting to note that even a small change in external parameters, such as light and temperature, introduces a significant amount of variability in the data. The maximum power point of the module changed with light soaking and also with the preconditioning procedure. During light soaking of the preconditioned modules, it was observed that the power and voltage were unstable due to light soaking and then relaxed back to their initial state.

5.4 Kesterite: CZTSSe

Measurements of the photovoltaic (PV) activity of solar cells under low-light conditions using different wavelength-selective filters can provide useful information about the nature, location and activation of defects and possible recombination

mechanisms inside of the solar cell interfaces. In this work, we employ this approach for characterizing flexible monograin membrane kesterite (CZTSSe) PV devices. The time dependence of the open-circuit voltage, short-circuit current, fill factor, and maximum power under low-intensity white, red, and blue light is studied and related to carrier recombination processes in the bulk of the absorber and at the interface with the CdS buffer and the electrodes. The different illumination conditions cause metastabilities in the electrical parameters, which are reversible when the cell is stored in the dark for some hours. Reversible and irreversible contributions to the light-soaking effects are further analyzed.

5.4.1 Effects of the colored-light pretreatment

The CZTSSe cells were irradiated with different colors of light using red and blue filters, and also under white light to observe the overall influence of visible spectra on the cell's electrical behavior.

CZTSSe Cell

Figure 5.19 presents the evolution of the short-circuit current density (J_{SC}), open-circuit voltage (V_{OC}), fill factor (FF), and maximum power point (P_{MPP}) of a typical monograin CZTSSe cell 2x under white, blue, and red light of 80 W/m^2 intensity for approximately 4 hours. During the low-intensity light-soaking experiments, the temperature change was maintained within a range of $pm1$ K. The effects were reversible: the STC cell measurements before and after light-soaking experiments, when stored overnight in the dark, showed matching results. In table 5.6, the results obtained before and after LS of cells 1x, 2x, and 3x are tabulated. However, the graphical representation depicts only one cell here.

Figure 5.19 shows the impact of light soaking on the CZTSSe cell. During light soaking, cell 2x showed a decline in its electrical performance. V_{OC} decreased by -3.9% (-2.5% for 1x and -5.4% for 3x) after 100 minutes of white-light soaking. Under blue light (450 nm), the reduction was -3.67% (-3.83 for 1x and -6.2% for 3x), but under red light (650 nm), it increased by 0.7% after 10 minutes and then decreased by -1.8% (-1.7% for 1x and -4.2% for 3x) after 120 minutes.

An interesting behavior was observed during white and red-light soaking, as both showed a consistent increase in J_{SC} (current density), which was not observed for the CIGS and CdTe technologies. Under red light, J_{SC} increased by 4.2% during the first 10 minutes and then decreased, reaching a level of +1.62%. Under white light, it remained more stable and reached a J_{SC} of 0.72%. The J_{SC} decreased during the blue LS by -4.66%.

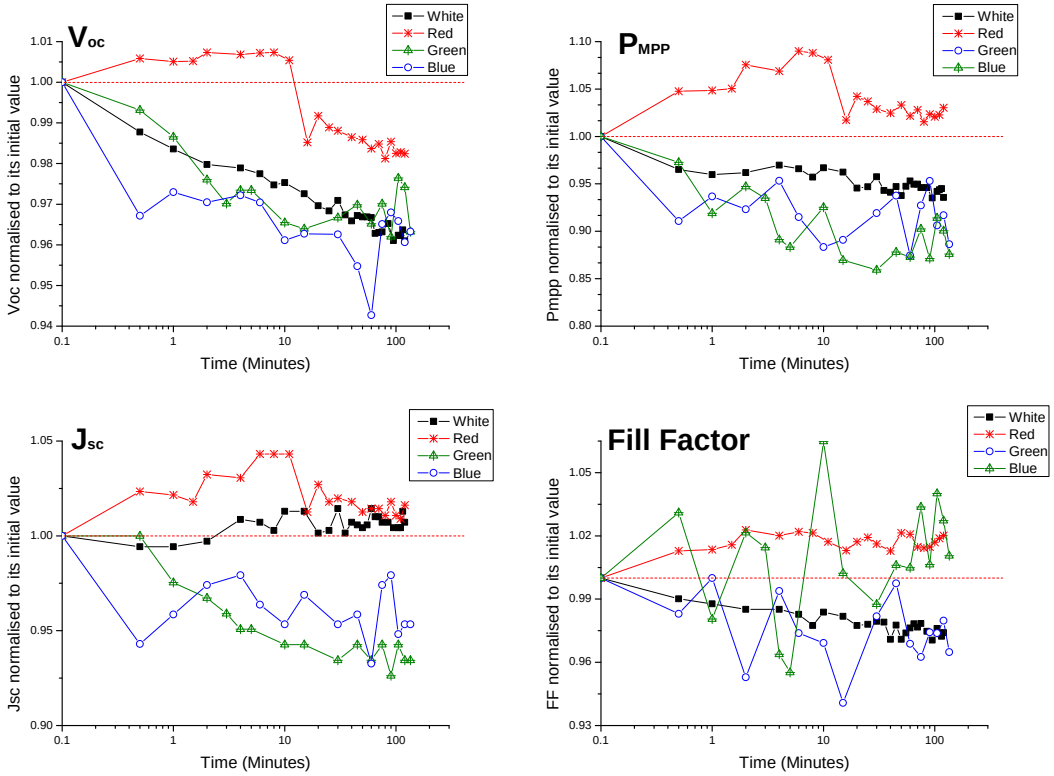

Fig. 5.19: Change in (a) V_{OC}, (b) I_{SC}, (c) P_{MPP}, (d) FF, during the colour-selective light soaking of the 2x CZTSSe monograin cell; lines are guides to the eyes.

P_{MPP} and FF showed the same decreasing behavior as V_{OC} under white and blue light, while for the red light, P_{MPP} and FF showed an increase in magnitude. P_{MPP} inverted its trend after reaching more than 9% after the initial 10 minutes of LS under red light, but then it started to decrease, reaching a final value of +3.03%. The amplitude of the FF increased during the first minute, but then stabilized at 1.8% to 2%, and finally reached a value of 2.01%. White LS showed a more monotonic behavior in P_{MPP} and FF, and reached a final decrease of -6.42% and -2.60%, respectively. In contrast, the blue LS fluctuated more, reaching the final relative value of P_{MPP} and FF by -11.37% and -3.51%, respectively.

Tab. 5.6: Absolute and relative changes in performance parameters of CZTSSe cells 1x, 2x, and 3x after light soaking.

Cell	Light	ΔV_{OC} (V)	ΔI_{SC} (A)	ΔFF (%)	ΔP_{MPP} (W)
1x	White (abs)	-0.010	$+2.0 \times 10^{-6}$	+0.32	-2.5×10^{-7}
	White (%)	-2.5	+1.24	+0.69	-0.85
	Red (abs)	-0.007	$+7.0 \times 10^{-6}$	-5.6	-4.8×10^{-6}
	Red (%)	-1.7	-4.5	-12.3	-18.6
	Blue (abs)	-0.015	$+4.0 \times 10^{-6}$	+0.45	-1.54×10^{-7}
	Blue (%)	-3.83	+3.05	+0.94	-0.62
2x	White (abs)	-0.019	$+1.0 \times 10^{-6}$	-1.31	-1.79×10^{-6}
	White (%)	-3.9	+0.72	-2.60	-6.42
	Red (abs)	-0.008	$+1.0 \times 10^{-6}$	+0.97	$+6.20 \times 10^{-7}$
	Red (%)	-1.8	+1.62	+2.01	+3.03
	Blue (abs)	-0.014	-2.0×10^{-6}	-1.53	-6.0×10^{-7}
	Blue (%)	-3.67	-4.66	-3.51	-11.37
3x	White (abs)	-0.018	$+1.0 \times 10^{-6}$	-0.14	-8.1×10^{-7}
	White (%)	-5.4	+0.62	-0.44	-4.70
	Red (abs)	-0.015	-4.0×10^{-6}	-1.37	-1.97×10^{-6}
	Red (%)	-4.2	-2.6	-4.17	-10.9
	Blue (abs)	-0.021	$+3.0 \times 10^{-6}$	-0.33	-8.9×10^{-7}
	Blue (%)	-6.2	-+2.14	-1.01	-5.79

CZTSSe modules

After investigating the fundamental behavior of cells under illumination, mini-modules were also examined. The electrical parameters under white, blue, and red light showed interesting behavior under different light conditions. The results presented in figure 5.19 are of V_{OC}, P_{MPP}, FF, and I_{SC} of the non-degraded CZTSSe module. Light soaking under white and blue (450nm) light showed a similar behavior for all electrical parameters except I_{SC}. The white and blue light soaking revealed a strong decrease in V_{OC}, P_{MPP}, and FF. Under red light, a slight decline was observed in V_{OC}, P_{MPP} and FF, while I_{SC} showed a slight increase.

Tab. 5.7: Changes in absolute and relative values in the performance parameter of a CZTSSe non-degraded module after light soaking.

Light Soaking	Voc [V]	Isc [A]	FF [%]	Pmpp [W]
White (absolute)	-0.29	1.30×10^{-4}	-2.47	-1.59×10^{-3}
White (relative %)	-4.4	1.94	-4.9	-7.33
Red (absolute)	-0.018	2.00×10^{-5}	-0.22	-9.00×10^{-5}
Red (relative %)	-0.2	0.3	-0.42	-0.38
Blue (absolute)	-0.385	2.00×10^{-5}	-1.78	-1.43×10^{-3}
Blue (relative %)	-6.12	0.38	-3.72	-9.18

All electrical parameters under red (650 nm) light showed a similar behavior for the first few minutes, as observed under white and blue light. However, after 300 minutes, they recover to their initial values. V_{OC} decreases by 2.7% after 3 minutes, and relaxes back to the initial value after 300 minutes, see figure 5.20(a). This is in contrast to the results of white and blue (450 nm) light illuminations, which cause a decrease of -4.4% and -6.2%, respectively.

An interesting trend was observed for I_{SC}, using white, blue, and red light in figure 5.20(b). All illuminations showed an increase in I_{SC} during the first 10 minutes. Subsequently, I_{SC} continued to increase under white light by approximately 2%, but decreased under blue and red light, relaxing to its initial value. Under white and blue light conditions, P_{MPP} showed a similar decrease of -8.9% and in FF a reduction of -4.5% from their initial values.

The V_{OC} amplitude was observed to decrease during blue and white light soaking. Under red light, it decreased for the first 10 minutes and then exhibited a reverse behavior. The P_{MPP} shows a significant decrease with time for white light. Interestingly, P_{MPP} decreased during the white and blue light soaking, but during the red light soaking, only a small change was observed.

In addition, a CZTSSe mini module was subjected to degradation by being kept in a climate chamber at 85% relative humidity and 85 °C for 1000 hours. After degradation, it was subjected to colored low-light soaking and a standard power rating. In figure 5.21 the V_{OC}, I_{SC}, P_{MPP}, and FF of the degraded module are shown.

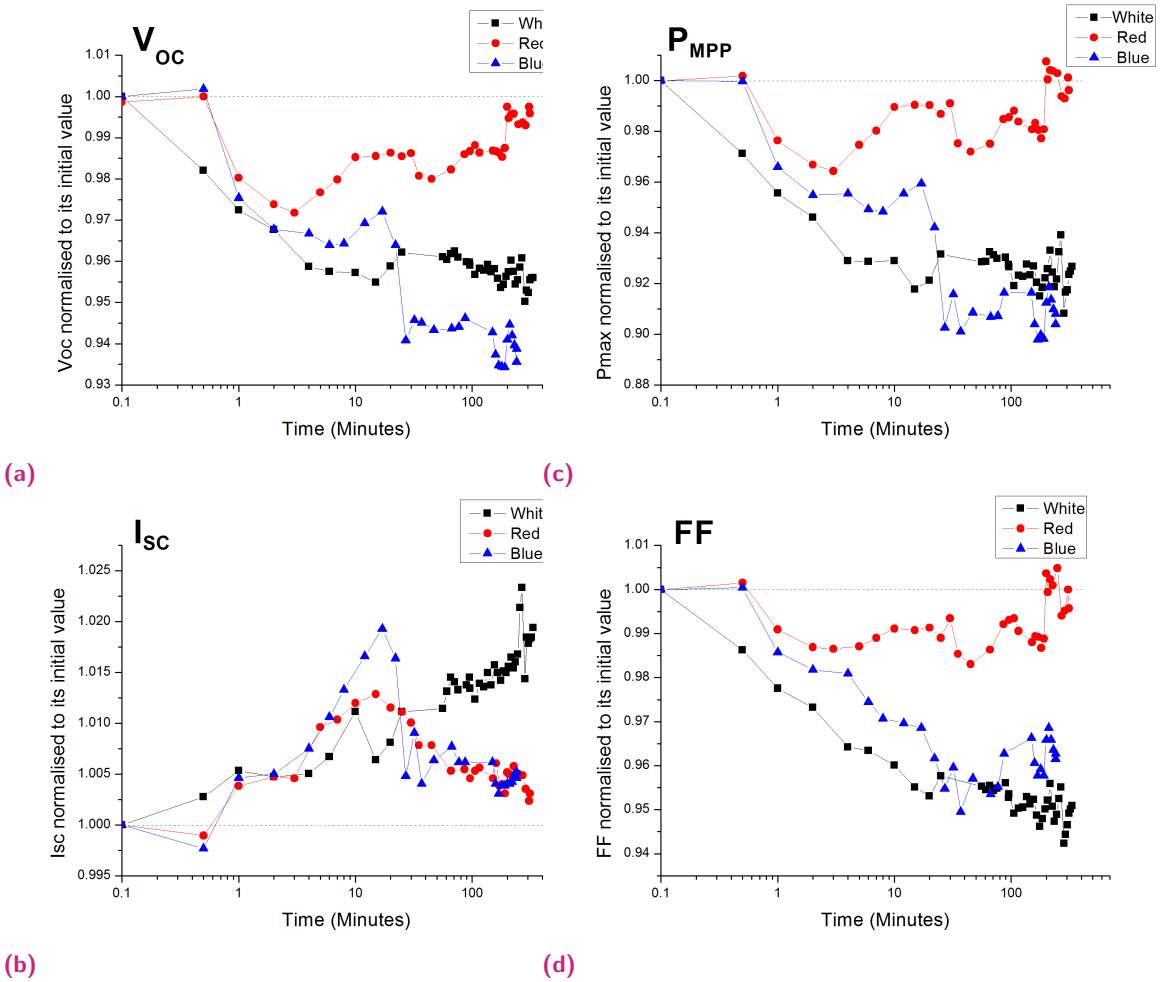

Fig. 5.20: Change in (a) V_{OC}, (b) I_{SC}, (c) P_{MPP}, (d) FF, during the color-selective light soaking of the non-degraded CZTSSe mini module.

Tab. 5.8: Changes in the performance parameter of a degraded CZTSSe module after light soaking in absolute and relative values.

Light Soaking	Voc [V]	Isc [A]	FF [%]	Pmpp [W]
White (absolute)	-0.32	$+7 \times 10^{-5}$	-0.89	-0.001
White (relative %)	-5.0	+1.0	-2.1	-6.1
Red (absolute)	-0.27	-2.0×10^{-5}	-1.52	-0.002
Red (relative %)	-4.11	-0.44	-3.48	-7.86
Blue (absolute)	-0.38	$+1 \times 10^{-5}$	-0.77	-0.001
Blue (relative %)	-5.8	+0.002	-1.7	-7.3

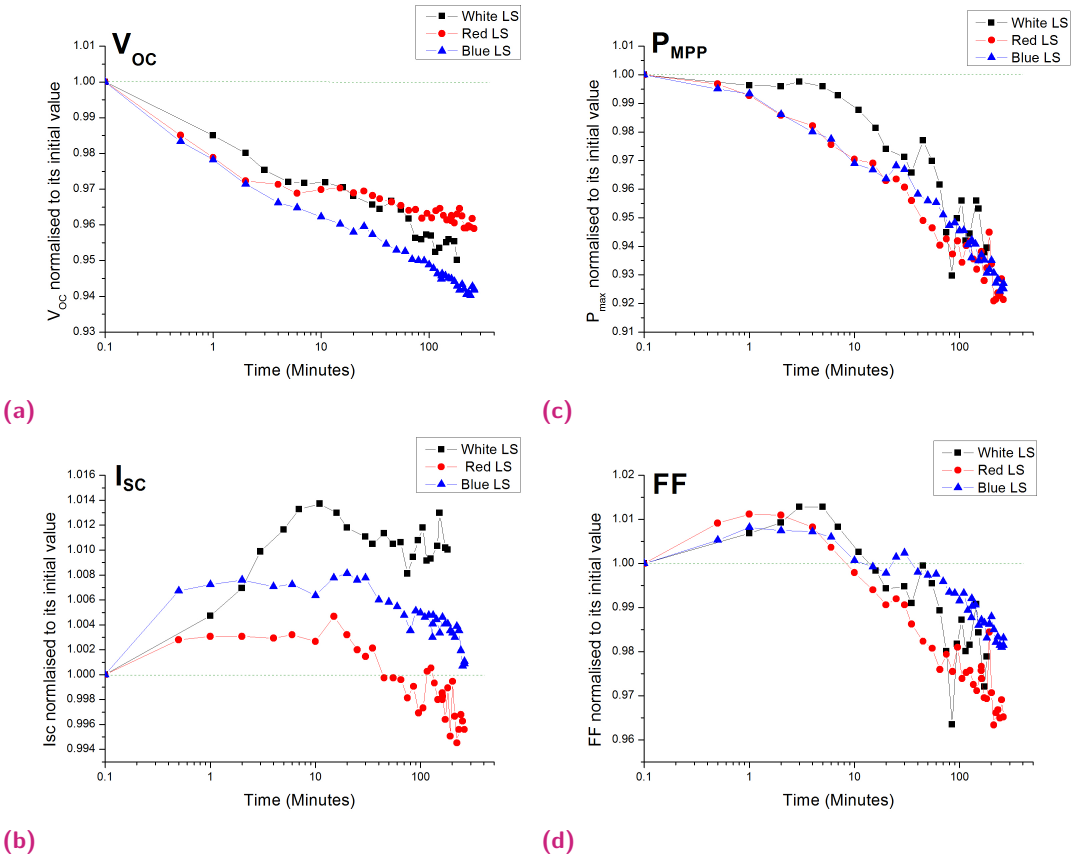

Fig. 5.21: Change in (a) V_{OC}, (b) I_{SC}, (c) P_{MPP}, (d) FF, electrical parameters during the colour-selective light soaking of the degraded CZTSSe mini module

The degraded module in figure 5.21 showed a decreasing trend in V_{OC} and P_{MPP} right after beginning the LS under colored and white light. The V_{OC} under white and blue light showed a decreasing trend until the end of LS, and the final relative values recorded were -5.0% and -5.8%, respectively. Conversely, in the red light, the decreasing slope becomes flatter after 100 minutes, and the final relative value was -4.11%.

The P_{MPP} under white light showed a negligible change during the first 10 minutes, but afterward, a steep decrease to -6.1% was measured. A similarity was observed between the red and blue LS in terms of P_{MPP}, both in trend and final value, with values of -7.86% for the red light and -7.3% for the blue light.

For I_{SC}, an increase was seen for white and blue LS. Under white LS it reached its peak after 10 minutes as +1.4% and later started to decrease, reaching +1% at the end; blue LS showed a similar increase until the first 20 minutes by +0.8% and relaxed to its initial value. For red LS the increase was maintained until the first 10

minutes by +0.5% and then a decrease in the trend followed, reaching the end at -0.44%.

Interestingly, for the FF, the trend appears to be reasonably similar for all colors, as shown in Figure 5.21(d), where FF initially increased until the first 5 minutes of LS and then decreased. The white, blue, and red LS reached final values of -2.1%, -3.48%, and -1.7%, respectively.

Comparison of I–V curves at the standard test conditions

All STC I–V curve performance parameters measured before and after light soaking of the CZTSSe cell 2x are tabulated in Table 5.9. The cell clearly shows differences in performance parameters after light soaking.

An interesting effect of the reversibility of the metastable state was observed after overnight dark relaxation of the CZTSSe cell. It is shown in figure 5.22, but since the initial and final IV curves at STC conditions are superimposed over each other, therefore, it is difficult to observe it in the graph.

The effect of CZTSSe mini-modules was investigated by comparing I-V curves under the standard test conditions before and after the illumination with white, red and blue light. Figure 5.23 presents the corresponding I-V curves, where the left-hand side, Figures 5.23(a)-(c), shows the behaviour of non-degraded module, whereas the right-hand side shows the behavior of degraded module. All STC I-V curves for the mini-module performance parameters, including V_{OC}, I_{SC}, P_{MPP}, fill factor (FF), and efficiency, measured before and after light soaking are tabulated in Tables 5.10 and 5.11, respectively.

For the non-degraded module, the light soaking shows only a slightly change in the performance of the module, indicating a stable operating state. During the white light soaking, a slight increase in V_{OC} by 0.05% while P_{MPP} decreased by -1.75%. This reduction is accompanied by a decrease in FF by -2.96% and a drop in efficiency by -1.92%, indicating a drop in series resistance. Blue light soaking causes the reduction in V_{OC} by -1.53%, P_{MPP} by -1.76% and a decrease in efficiency by -1.54%, showing clearly a leftward shift in the I-V curve, mainly caused by the enhanced recombination or limitation of charge carrier transport due to high energy photons. Contrarily, the red light soaking lead to an increase in P_{MPP} from +0.6% and an improvement in FF by +2.57%, with a net efficiency gain by +0.4%, despite a decrease in V_{OC} of -2.01%.

(a)

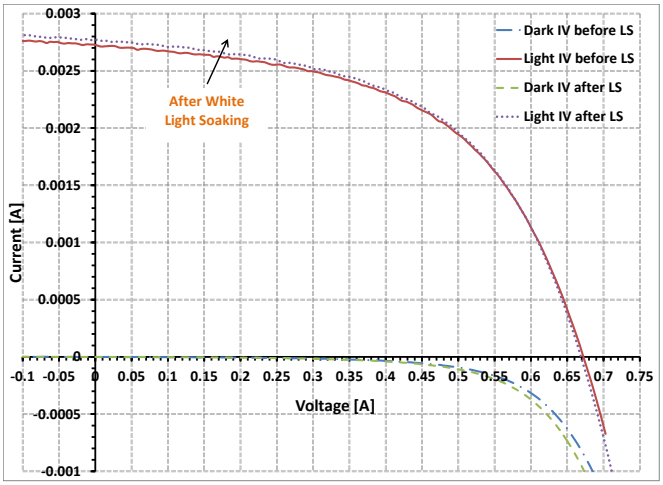

(b)

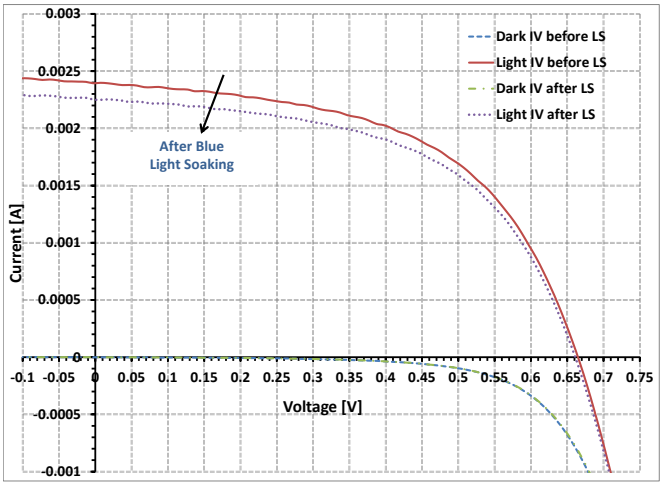

(c)

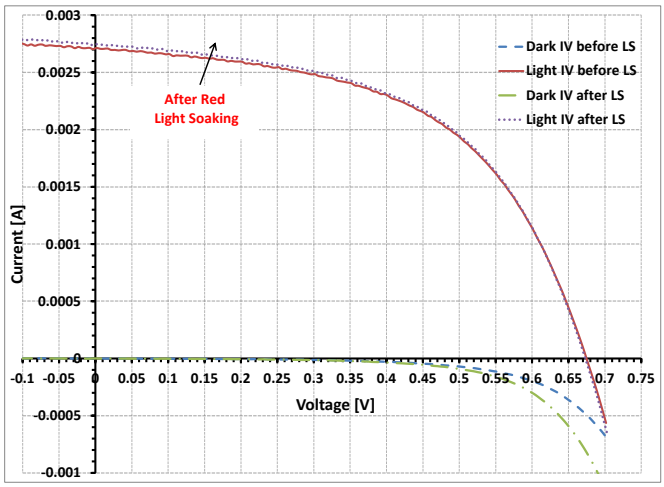

Fig. 5.22: Comparison of the I–V curves of cell 2x at STC before and after light soaking under (a) white light, (b) blue light, and (c) red light.

The degraded module exhibits a stronger response to the different light soaking. After white light soaking, P_{MPP} increases by +2.22%, while the efficiency improves from +2.73% accompanied by an increase in I_{SC} of +2.84%. During the red light soaking the recovery of the electrical performance of the module was more pronounced, gaining a +4.47% increase in efficiency. The P_{MPP} increased by +4.05% and I_{SC} by +5.75%, while the V_{OC} decreased by +1.52%, showing a overall improvement due to improved charge collection and reduction in transport losses of charge carriers. Blue light soaking, showed also an improvement in P_{MPP} by +2.48% and efficiency by +2.62%, accompanied by an increase in I_{SC} by +3.68% and a reduction in V_{OC} by -1.38%.

Overall, the quantitative analysis demonstrate that spectrally selective light soaking has small impact on the non degraded modules, whereas it induces a clear recovery in the degraded module. The main contribution in improvement of the performance parameters is due to the increase in I_{SC} and FF rather than V_{OC}, which decreases after light soaking. A strong recovery under red light is indicating a role of reversible nature of metastabilities, due to reconfiguring of the metastable defects.

These measurements help reveal the locations of defects related to changes in the electrical state of the cell heterojunction or interfaces. This study can help determine the location of defects that lead to the metastable state and the quality of the thin-film PV device for further use.

Tab. 5.9: Effect of white and colored light soaking (LS) on the I–V curves at the standard test conditions before and after light soaking of the CZTSSe cell 2x. Percentage changes are calculated relative to the initial values.

Parameter	**White**		**Red**		**Blue**	
	Initial	*Final*	*Initial*	*Final*	*Initial*	*Final*
Voc [V]	0.671	0.668	0.674	0.672	0.663	0.660
Change (%)	-0.45		-0.30		-0.45	
Isc [mA]	2.720	2.766	2.705	2.743	2.395	2.254
Change (%)	+1.69		+1.40		-5.88	
Pmpp [mW]	0.980	0.991	0.976	0.986	0.854	0.804
Change (%)	+1.12		+1.02		-5.85	
FF [%]	53.67	53.62	53.37	53.46	53.75	54.04
Change (%)	-0.09		+0.16		+0.54	
Efficiency	6.13	6.19	6.10	6.16	5.34	5.02
Change (%)	+0.98		+0.98		-5.99	

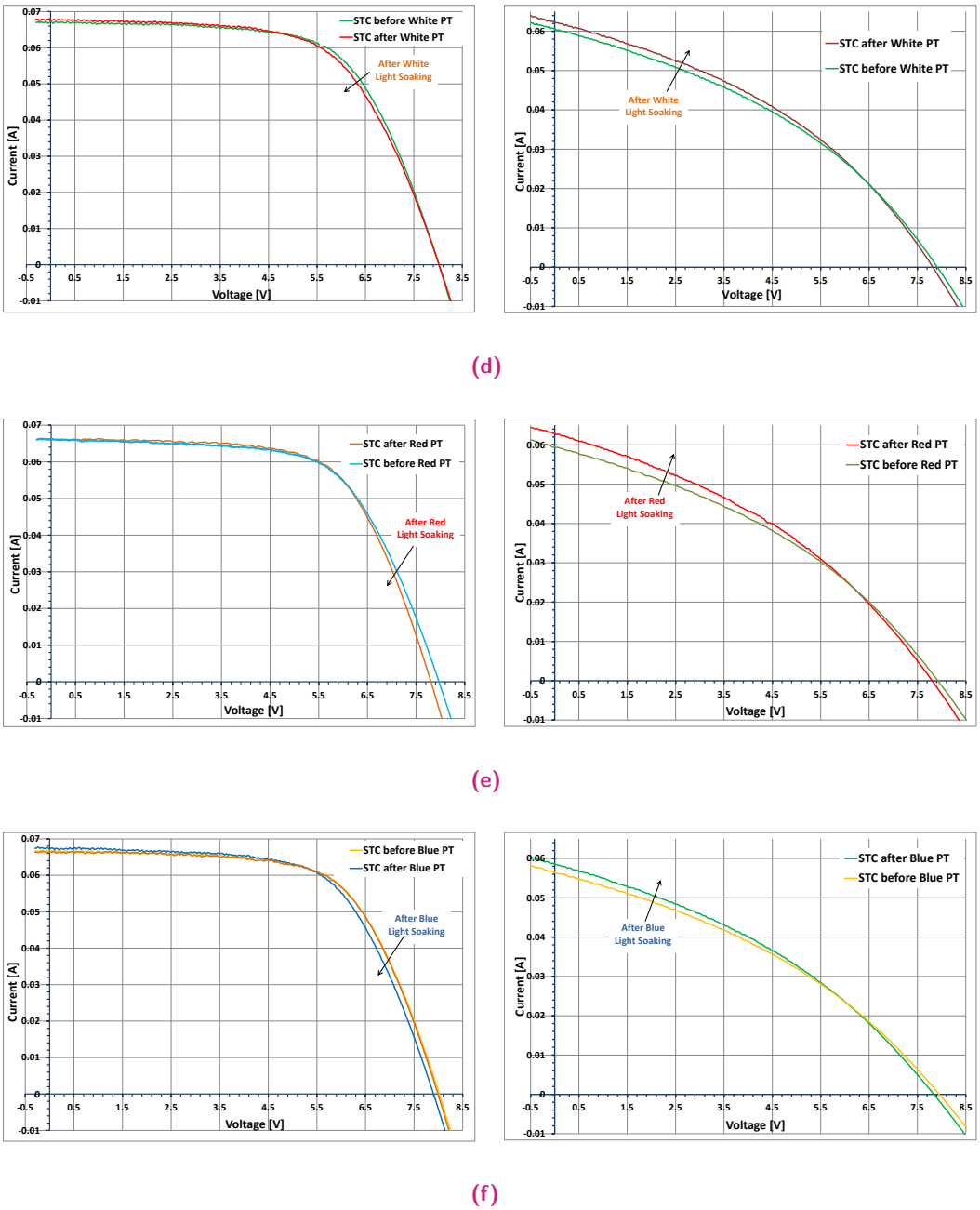

Fig. 5.23: Comparison of I–V curve at the STC before and after the light soaking under white, blue, and red light of the non-degraded and degraded CZTSSe module. The three plots on the left side (labeled as a, b, and c) represent the I–V curves for the non-degraded module. The three plots on the right side (labeled as d,e,f) are the I–V curves for the degraded module.

Tab. 5.10: Effect of white and coloured light soaking (LS) on the IV curves at standard test conditions before and after light soaking of the non-degraded CZTSSe mini-module. Percentage changes are calculated relative to the initial values.

Parameter	**White**		**Red**		**Blue**	
	Initial	*Final*	*Initial*	*Final*	*Initial*	*Final*
Voc [V]	8.010	8.014	7.960	7.800	8.013	7.890
Change (%)	+0.05		-2.01		-1.53	
Pmpp [W]	0.342	0.336	0.331	0.333	0.341	0.335
Change (%)	-1.75		+0.60		-1.76	
Isc [mA]	67.03	67.70	66.10	66.10	66.80	67.40
Change (%)	+1.00		0.00		+0.90	
FF [%]	63.84	61.95	62.95	64.57	63.90	63.05
Change (%)	-2.96		+2.57		-1.33	
Efficiency	5.22	5.12	5.05	5.07	5.19	5.11
Change (%)	-1.92		+0.40		-1.54	

Tab. 5.11: Effect of white and colored light soaking (LS) on the I–V curves at the standard test conditions before and after illumination of the CZTSSe degraded mini-module.

Parameter	**White**		**Red**		**Blue**	
	Initial	*Final*	*Initial*	*Final*	*Initial*	*Final*
Voc [V]	7.91	7.82	7.92	7.80	7.95	7.84
Change [%]	-1.14		-1.52		-1.38	
Pmpp [W]	0.180	0.184	0.173	0.180	0.161	0.165
Change [%]	+2.22		+4.05		+2.48	
Isc [mA]	60.56	62.28	59.45	62.87	56.48	58.56
Change [%]	+2.84		+5.75		+3.68	
FF [%]	37.62	37.92	36.72	36.73	35.91	36.01
Change [%]	+0.80		+0.03		+0.28	
Efficiency	2.56	2.63	2.46	2.57	2.29	2.35
Change [%]	+2.73		+4.47		+2.62	

This study can help determine the location of defects that lead to the metastable state and the quality of the thin-film PV device for further use. For industrial standards, the power rating plays an important role. If the device under test (solar cells) changes its electrical behavior over time under the influence of irradiation, it can lead to the measurement of an erroneous power.

The present work demonstrates how low-light conditions can introduce moderate changes in the electrical parameters of monograin-CZTSSe technology within a short time interval. It was found that the observed metastabilities are most likely to originate near the heterojunction in the CZTSSe solar cells. This was revealed by colored-light soaking. It was also found that light-induced metastabilities are reversible. All of these changes are reflected in the electrical parameters of the solar cells.

In all technologies, V_{OC} increased but tended to decrease in some samples, indicating that the shunt resistance decreases, reflecting more recombinations and a lower voltage.

5.5 Two-diode model parameters of CZTSSe and CIGS

Two-diode models of the CZTSSe and CIGS samples can reveal some intrinsic aspects of the cells. All results are summarized in table 5.12 (CZTSSe), table 5.13 (CIGS with CdS buffer layer), and table 5.14 [CIGS with Zn(O,S)] buffer layer.

Cells of the CZTSSe monograin technology were previously used for the pretreatment cycle. To compare with its closest similar technology, some CIGSSe cells were used, which were already part of another research study for the same colored low-irradiance pretreatment process [42]. Since CZTSSe may potentially serve as a replacement for the CIGS technology in the future, it would be interesting to compare. The model was applied to the dark I–V curves. To easily understand the I–V curves, a semi-logarithmic plot provides better visibility for interpreting the linear portions of the diode.

5.5.1 Monograin CZTSSe

In the case of the fitting of the 2-diode model of the CZTSSe cells, all data fit well to the raw dark I–V data. Figure 5.22 shows dark I–V curves together with fits.

The ideality factor of the first diode n_1 showed an ideal behavior in cells 1x and 3x with $n1|_{1x} = 1.02$ and $n1|_{3x} = 1.02$, but in cell 2x it had a slightly higher value of $n1|_{2x} = 1.37$. The ideality factors of the second diode generally had higher values than for the first diode. Also, for the second diode, the ideality factor n_2 for cells 1x and 3x are $n2|_{1x} = 2.63$ and $n2|_{3x} = 2.77$, respectively. However, for cell 2x, the ideality factor n_2 was $n2\ |_{1x} = 3.59$. A large ideality factor of the second diode could be interpreted as multi-level recombination.

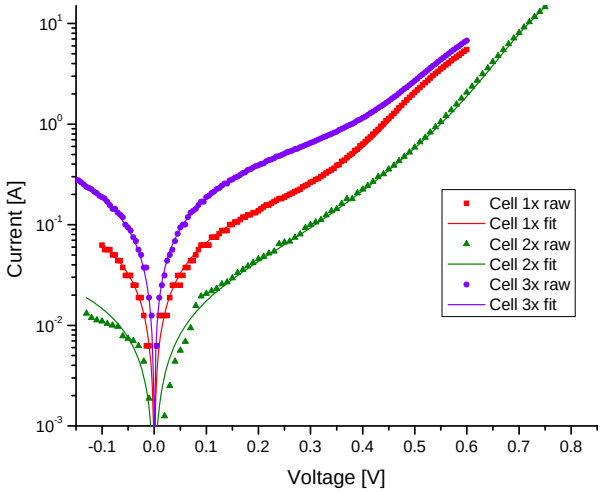

Fig. 5.24: The 2-diode model fits of the CZTSSe monograin technology.

The reverse saturation currents, J_{01} and J_{02}, describe the current from the first and second diodes. In CZTSSe monograin cells, the samples showed a higher value of the recombination current (J_{02}) than the diffusion current (J_{01}). This indicates the presence of more defects inside the solar cells.

The data for cells 1x and 3x follow the 2-diode behavior well. Cell 2x deviates from the 2-diode model, as seen in Figure 5.24.

Tab. 5.12: Parameters of CZTSSe cells extracted from the 2-diode model of dark-I–V curves.

Device	**J_{01} [A/cm^2]**	**n1**	**J_{02} [A/cm^2]**	**n2**	**R par [Ω*cm^2]**	**R ser [Ω*cm^2]**
Cell 1x	2.32×10^{-11}	1.02	9.24×10^{-7}	2.63	1553.6	18.24
Cell 2x	2.05×10^{-11}	1.37	2.14×10^{-6}	3.59	7560.4	3.21
Cell 3x	1.21×10^{-11}	1.03	1.97×10^{-6}	2.77	548.24	12.78

The parasitic resistances were extracted from the fits. The shunt resistance R_{SH} was relatively smaller for cells 1x and 3x as 1.553 kΩ and 548.24 Ω, respectively. Cell 2x had the highest R_{SH} among all cells as 7.56 kΩ. The same holds for the series resistances, where R_S was found to be high, at 18.24 Ω and 12.78 Ω for cells 1x and 3x, respectively, but the lowest R_S of 3.21 Ω was observed for cell 2x.

5.5.2 CIGS

These cells were selected based on their V_{OC} and P_{MPP} values. Among cells 4, 8, 28, and 32 that have CdS as the buffer layer, cells 4 and 28 were rated 'poor' in quality because their V_{OC} and P_{MPP} were lower, cell 8 being 'medium' in quality, and 32 being 'good' as its V_{OC} and P_{MPP} were the highest. Among cells 5 and 25 with Zn(O,S) as buffer layer, cell 5 had the lower V_{OC} and P_{MPP} values than cell 25. Hence, cell 5 is considered poor quality and cell 25 as of good quality. All results are tabulated in table 5.13 for CIGS with CdS as buffer layer, and in table 5.14 for CIGS with Zn(O,S) as buffer layer.

Looking at figure 5.25(a) it can be seen that cells 4 and 28 did not have a good raw dark I–V curve. All cells had a low series resistance R_S. The fit parameters of cells 4 and 28 had considerably low J_{01} of 7.6×10^{-14} A/cm^2 and 4.59×10^{-13} A/cm^2, whilst the J_{02} had a higher value of 1.85×10^{-6} A/cm^2 and 1.61×10^{-6} A/cm^2. Their ideality factors were in accordance with the standard values. In addition, the shunt resistances R_{SH} of cells 4 and 28 were 1.183 kΩ and 642.75 Ω, which is higher than that of cells 8 and 32.

CIGS cells 5 and 25 with Zn(O,S) as a buffer layer showed good fits with the two-diode model, illustrated in figure 5.25(b). Here, the R_{SH} is quite small compared to cells with a CdS buffer layer. The ideality factors were in accordance with the standard values. A low shunt resistance R_{SH} was observed in both cells 5 and 25, 150.45 Ω and 20.66 Ω, respectively. The reverse saturation current J_{01} was lower than J_{02} in both cells. Cell 5 had J_{01} of 1.03×10^{-25} A/cm^2 and J_{02} of 1.01×10^{-7} A/cm^2, and cell 25 had J_{01} of 2.17×10^{-24} A/cm^2 and J_{02} of 5.16×10^{-8} A/cm^2. In both cases, a higher recombination current than diffusion current was found.

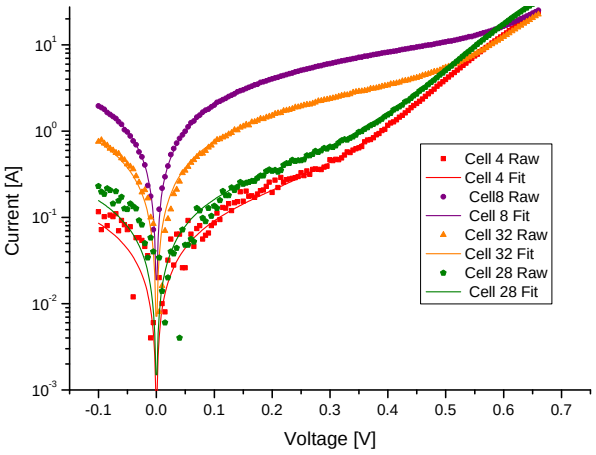

(a)

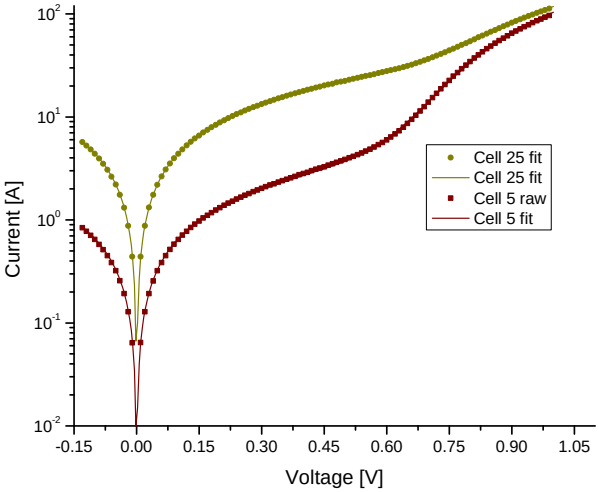

(b)

Fig. 5.25: The 2-diode model fitting of (a) CIGSSe cells with a CdS buffer layer and (b) CIGSSe cells with a Zn(O,S) buffer layer.

Tab. 5.13: Parameters of CIGSSe cells with a CdS buffer layer extracted from the 2-diode model of dark I–V curves.

Device	J_{01} [A/cm^2]	n1	J_{02} [A/cm^2]	n2	R par [Ω*cm^2]	R ser [Ω*cm^2]
Cell 4	7.60×10^{-14}	0.98	1.85×10^{-6}	2.51	1183.1	2.11
Cell 8	1.18×10^{-8}	1.75	7.56×10^{-3}	64.90	62.7	1.47
Cell 28	4.59×10^{-13}	1.05	1.61×10^{-6}	2.42	642.8	1.46
Cell 32	5.07×10^{-9}	1.60	5.17×10^{-6}	3.56	131.9	2.03

The parameters of the 2-diode model in cell 8 were not realistic, as the fits showed the ideality factor n_2 to be 64.9, which is not physically plausible. The two reverse saturation currents showed that the recombination current J_{02} was really high (7.56×10^{-3} A/cm^2) compared to J_{01} (1.18×10^{-8} A/cm^2). J_{02} was found to be the highest among all cells containing the CdS buffer layer. The shunt resistance R_{SH} was the lowest among all cells, with a value of 62.706 Ω.

When analyzing cell 32, the reverse saturation current, the diffusion current J_{01} of value 5.07×10^{-9}, was the highest compared to all other cells. The recombination current J_{02} was still higher than J_{01}. The ideality factors n_1 at 1.60 and n_2 at 3.56 were slightly higher than the expected values.

Tab. 5.14: Parameters of CIGSSe cells with a Zn(O,S) buffer layer extracted from the 2-diode model of dark-I–V curves.

Device	J_{01} [A/cm^2]	n1	J_{02} [A/cm^2]	n2	R par [Ω*cm^2]	R ser [Ω*cm^2]
Cell 5	1.03×10^{-25}	1	1.01×10^{-7}	2.30	150.45	1.80
Cell 25	2.17×10^{-24}	1	5.16×10^{-8}	2.09	20.66	1.97

5.6 Impedance spectroscopy

The CZTSSe monograin and the CIGSSe cells were analyzed for their dependence of capacitance on voltage. For this experiment, 1 kHz modulation frequency and 25 mV amplitude were used. The results were plotted in the Mott-Schottky diagram to extract the carrier density in the device. The Mott-Schottky plot of the CZTSSe monograin devices used for the pretreatment is shown in Figure 5.26. All results are tabulated in table 5.15 together with the measured carrier density.

The linear fit from the $1/C^2$ slope is used to extract the carrier density of the bulk material. The built-in voltage can also be extracted from it when the intercept with the x-axis is extended toward the linear region. In this case, it could not provide realistic results, as a uniform space-charge profile might not be present, and an extrapolated intercept on the voltage axis does not relate to the built-in voltage.

When the carrier density is compared between the three cells of the monograin CZTSSe, obtained from the Mott-Schottky plot, cell 2x has the highest at 1.01×10^{15} cm^{-3}. The carrier densities of cells 1x and 3x were determined to be 7.26×10^{14} cm^{-3} and 6.50×10^{14} cm^{-3}, respectively.

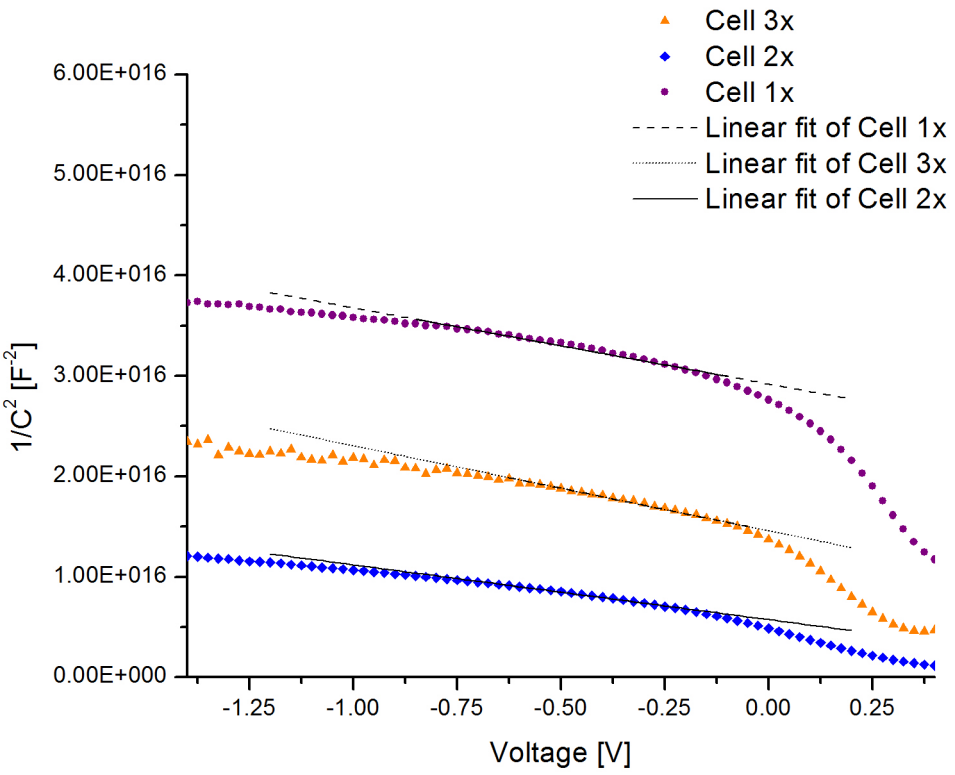

Fig. 5.26: Mott-Schottky plot of the CZTSSe monograin cells to extract the carrier density through a linear fit of the slope in the negative bias region.

Figure 5.27 presents the Mott-Schottky plots of the CIGSSe devices used for comparative purposes with the CZTSSe devices. Cells with CdS buffer are shown in the figure 5.27(a),(b), and cells with Zn(O,S) buffer are shown in figure 5.27(c).

When looking at the Mott-Schottky graph of CIGS cells with CdS buffer layer, it is observed that cells 4 and 28 show a similar carrier density of 1.75×10^{13} cm^{-3} and 1.47×10^{13} cm^{-3}, as their quality is also considered the same due to their poor V_{OC} and P_{MPP}. Cells 8 and 32, labeled medium and higher quality, also show a higher carrier density of 6.64×10^{13} cm^{-3} and 3.76×10^{14} cm^{-3}, respectively.

In CIGS cells with the Zn(O,S) buffer layer, it is observed that they show a higher carrier density due to their low V_{OC} and high I_{SC}. Cell 5 has a carrier density of 2.38×10^{14} cm^{-3}, and cell 25 has 6.73×10^{14} cm^{-3}.

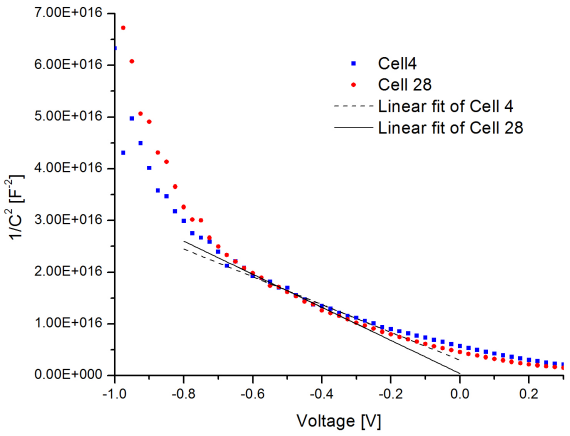

(a)

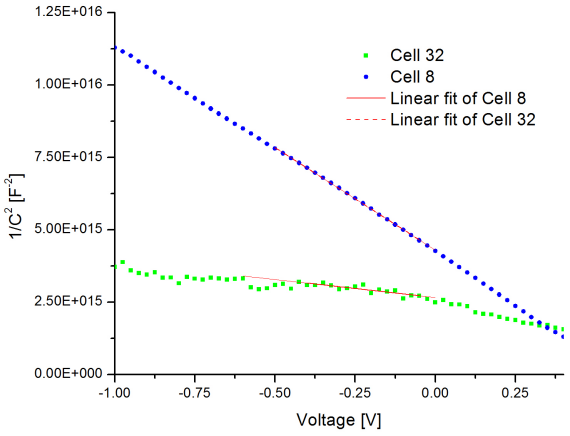

(b)

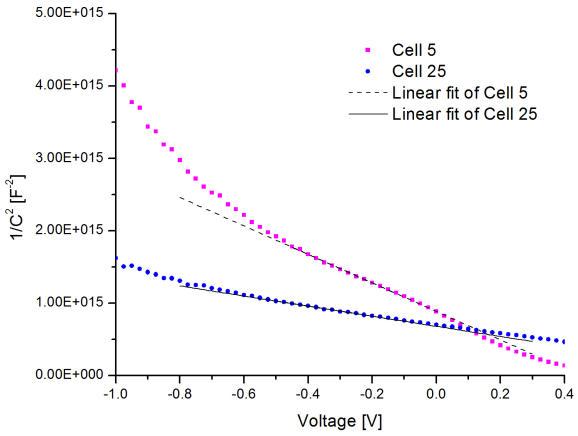

(c)

Fig. 5.27: Mott-Schottky plot of (a) cell 4s and 28 (CIGSSe with a CdS buffer layer), (b) cells 8 and 32 (CIGSSe with a CdS buffer layer), and (c) cell 5 and 25 (CIGSSe with a Zn(O,S) buffer layer).

All cells selected from both technologies were also analyzed by impedance spectroscopy. Interestingly, when the CIGS cells were analyzed using impedance spectroscopy, it was observed that the Nyquist plots overlapped and superimposed on each other at higher biases, except at zero bias; therefore, these results are not shown here, as they lack physical significance. The results of CZTSSe monograin cells are shown at different biases, where they seem to show a lot of change to varying biases, as can be seen in Fig. 5.28. The derived values for R_S and R_{SH} are tabulated in table 5.15.

The R_S and R_{SH} for CZTSSe from impedance spectroscopy were found to be higher than from I–V characterization in the STC measurement. In figure 5.28 (a), (b), and (c), the Nyquist plots for cells 1x, 2x and 3x gave a high shunt resistance R_{SH} of 1.536 kΩ, 5.333 kΩ, and 3.195 kΩ. Even the series resistance R_S showed a high value. The value of R_S in all cells 1x, 2x and 3x was 58.2 Ω, 12.5 Ω and 40.09 Ω.

Tab. 5.15: Carrier density and resistance values of CZTSSe monograin cells calculated from the Mott-Schottky and Nyquist plots.

Device	N_a **(cm^{-3})**	R_S **(Ω)**	R_{SH} **(kΩ)**
Cell 1x	7.26×10^{14}	58.20	1.54
Cell 2x	1.01×10^{15}	12.50	5.33
Cell 3x	6.50×10^{14}	40.09	3.20

Tab. 5.16: Carrier density and resistance values of CIGSSe solar cells calculated from the Mott-Schottky and Nyquist plots.

Device	N_a **(cm^{-3})**	R_S **(Ω)**	R_{SH} **(kΩ)**
Cell 4	1.75×10^{13}	4.01	1468.69
Cell 8	6.64×10^{13}	10.04	2346.76
Cell 28	1.47×10^{13}	2.74	1048.16
Cell 32	3.76×10^{14}	–	–
Cell 5	2.38×10^{14}	3.08	291.57
Cell 25	6.73×10^{14}	2.58	47.35

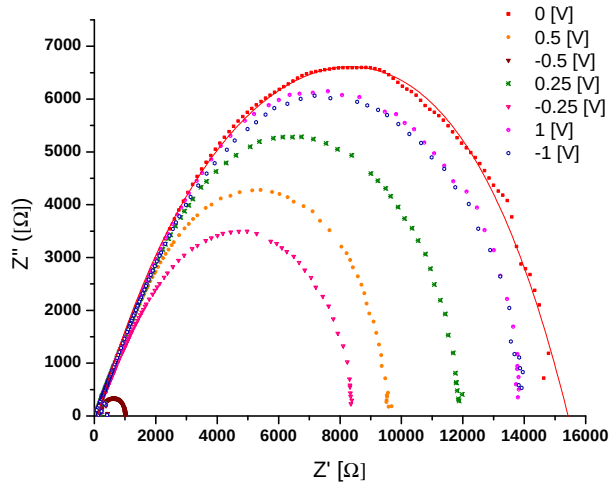

(a)

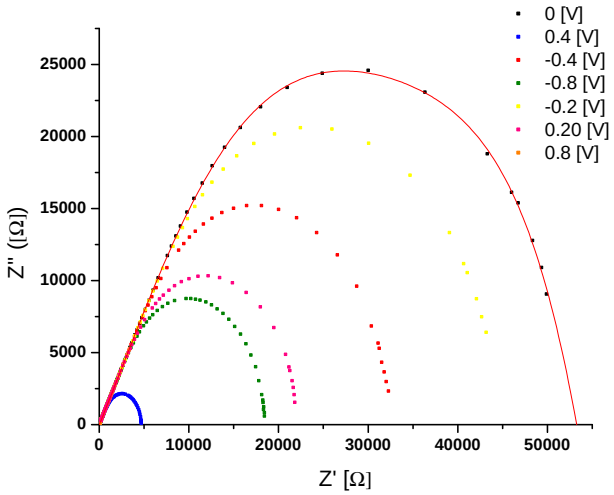

(b)

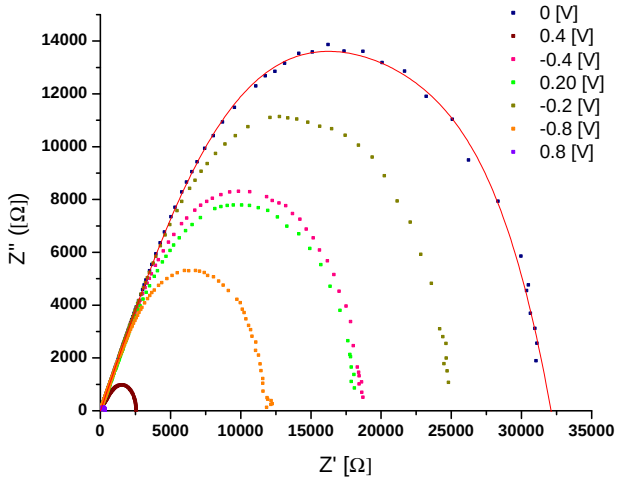

(c)

Fig. 5.28: Nyquist plots of the CZTSSe cells at different voltage bias (a) cell 1x, (b) cell 2x, and (c) cell 3x.

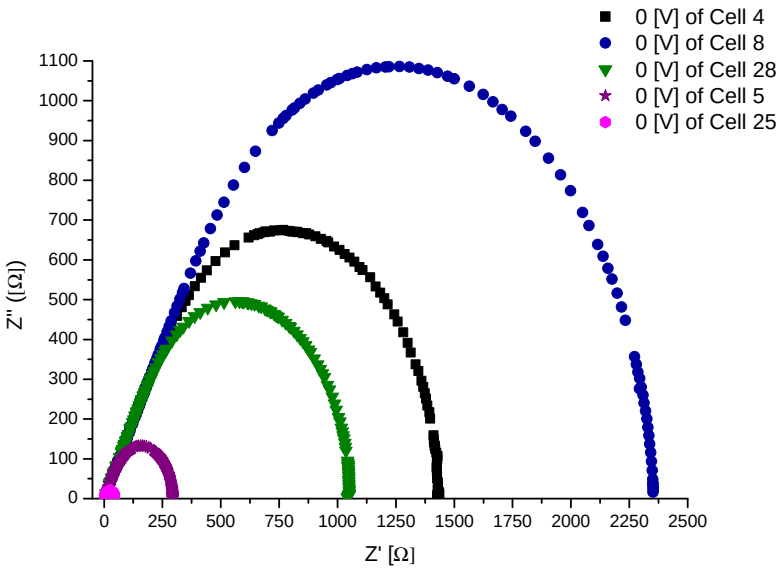

Fig. 5.29: Nyquist plot of all CIGS cells at zero bias.

For the CIGS cells, the results are shown only at zero bias in figure 5.29. The results of data evaluation are summarized in tab. 5.16. When looking at the cells with the CdS buffer with poor and medium quality, it was observed that cells 4 and 28 had a lower R_S of 4.01 Ω and 2.74 Ω, respectively, while cell 8 showed a R_S of 10.04 Ω. Cell 8 has a higher R_{SH} of 2.34 kΩ compared to cells 4 and 28 of 1.46 kΩ and 1.05 kΩ.

Apparently, the cells with Zn(O,S) buffer layer, for instance, cell 5, showed a higher R_{SH} than cell 25, despite cell 25 having better performance than cell 5. Cell 5 had 291.57 Ω and cell 25 had 47.35 Ω of R_{SH}, whereas the series resistance was close to each other, 2.58 Ω for cell 28 and 3.08 Ω for cell 5.

Chapter 6

DISCUSSION

> *In science, there are no shortcuts to truth.*
>
> **— Karl Popper**
> (Austrian-British philosopher of science,
> 1902–1994)

According to the chemical kinetics, at higher temperatures, the reaction rate of all thermally driven mechanisms increases [21, 22]. Further, different forms and energy levels of activation change the behavior of devices in accordance with their thermal state. The driving effects are illumination level (i.e., photons/sec or light wavelength (photon energy).

It is observed from the pretreatment results that metastability occurs under low-light conditions, and its effects are evident in the performance parameters of the PV device.

The a-Si:H and CdTe modules have spectral responses in the range of 350 to 800 nm, whereas CIGS and CZTS have a wide spectral response; thus, the latter technologies can absorb more photons [43]. However, regardless of better outdoor performance, one factor still hinders the measurement of the correct power rating under STC [44]. This makes it challenging to estimate the power generated by thin-film photovoltaics accurately.

6.1 Amorphous silicon

In a-Si:H, it is generally mentioned that recovering all power at low temperatures is not possible unless it is 150 °C, as there has to be a structural change in the material for recovering the original power, which is directly related to healing of the dangling bonds. In contrast to the theory mentioned above, power could be recovered from low-temperature annealing, which does not provide enough energy to affect a structural change. It can only be related to the healing of weak bonds, as they have a low activation energy, which can be recovered sufficiently with the application of low-temperature annealing [45, 46, 47].

The defect annealing in a-Si technology has been investigated in detail regarding power recovery under low temperatures. When doping is carried out in intrinsic a-Si:H, the magnitude of the defect density increases by two or three orders of

magnitude [48]. The hole trapping and the electron trapping activation energy are found to be 0.4-0.8 eV in [49, 50, 51, 52].

6.1.1 a-Si:H Pretreatment

Pretreatment is performed to observe the saturation of the metastable behavior of the trapping sites in one direction. V_{OC} depends on the ideality factor n, which depends on the type of recombination. Usually, its value is one under radiative recombination. A higher value of n degrades the FF, as high recombination of charge carriers generates low V_{OC} [53].

$$W(\mathrm{Si}-\mathrm{Si})+\mathrm{Si}-\mathrm{H}+e+h \longrightarrow 2\mathrm{Si}-db+\mathrm{Si}-\mathrm{H}$$

where W(Si-Si) refers to a weak Si-Si bond, and db refers to a dangling bond. The nonradiative recombination of charge carriers has been proposed as a cause of H emission during light-induced degradation of a-Si: H [54][55].

6.1.2 a-Si vs μcSi

The results show that measuring a module in a stable state under parasitic illumination might be impossible without proper treatment. The power rating is explicitly affected by exposure to light and changes in temperature. As presented in section 5.1.1 for the a-Si:H type module S1 (in fig. 5.1), under pretreatment at a variable temperature, V_{OC} and P_{MPP} increased from their initial value to 0.42% and 2.8% and declined with almost the same rate when stored in the dark. During the first 10 minutes of illumination, no V_{OC} change is measured for the a-Si:H modules. After that, the value increases in amplitude for an hour and attains saturation. However, for the P_{MPP}, the change occurred right after the LS. This observation could indicate a superposition of at least two dynamics that refer to different time scales. Stabilization of the electrical parameter values was obtained after the first hour of LS [56, 57].

When the same pretreatment procedure was applied to the S1 module at a stable temperature close to 25 °C, as shown in Fig. 5.1(a), a similar effect was observed in V_{OC} and P_{MPP}. Still, the change in pretreatment amplitude was substantially minor. The V_{OC} showed an increase of +0.21% during LS at the stable temperature, almost half of the magnitude achieved during LS with variable temperature. Interestingly, I_{SC} remained constant during pretreatment. A similar effect was observed in the CdTe technology (cadmium telluride) [27, 40]. Studies on CIS/CIGS technologies under low irradiance have shown a direct correlation with a metastable change in the electrical parameters, as reflected in the power rating [58, 59].

In a photovoltaic device, the open-circuit voltage, V_{OC}, depends on the ratio I_{SC}/I_0 in a logarithmic way; I_0 is the reverse saturation current of the diode [60]. Since

I_{SC} shows changes during pretreatment, this indicates that both I_{SC} and I_0 of the p-i-n junctions contribute to this behaviour. Since both FF and P_{MPP} are more directly affected by a change of I_0, the more substantial variety observed in these two parameters, due to I_0, could be expected. In Fig. 5.1 (a) and (b), after 10 min, V_{OC} increases strongly, while the changes in FF and P_{MPP} continue to follow the same trend. This can be explained by the effect of elevated temperature and irradiance during the pretreatment, and the assumption of a typical single-diode reverse saturation current, I_0, for the whole module.

Micromorph modules exhibited a reversal behavior during pretreatment at variable temperatures compared to the a-Si:H technology. However, the final value of P_{MPP} is below the initial value and the module's evolution toward the final stable equilibrium point. In this case, the dark relaxation curve would end again at approximately 0.94 (normalized value in Fig.5.2 (a)), also assuming that the main fraction of changes in P_{MPP} are attributed to changes in I_{SC}, V_{OC}, and FF in their final saturation values. Sudden elevated temperatures also cause a change in P_{MPP}. External conditions, such as stray fields and biasing, may contribute to an additional impact that drives the module away from its equilibrium point. Furthermore, the a-Si modules are composed solely of amorphous silicon in a double-junction (tandem) cell configuration.

In contrast, micromorph modules feature a tandem cell configuration with different material structures. This might have resulted in a difference in the behavior of the counteracting metastable effects. The plateau-like behavior of the double junction a-Si structure and micromorph modules for the initial period of LS may represent a link between the behaviors of both technologies, or may pertain to layers of different material structures.

Summarizing the experimental findings, the investigated effects alter the precision of power rating in the laboratory in various ways. The illumination at low-light levels alters the measured power values for $\pm 2.8\%$ at a variable temperature and $\pm 0.42\%$ at a stable temperature in a-Si modules, and $\pm 3.29\%$ in a micromorph module at a variable temperature. The result depends on the illumination time, dark storage, and temperature, and therefore is directly influenced by handling before the STC measurement.

Additionally, subject to temperature and light soaking, it is evident that the measured effects of electrical changes are relevant when considering the superposition of both factors. This experiment confirmed that LS affects the modules.

6.1.3 Annealing

All modules annealed showed an increase in their STC power. The increase depends on the module's history and the annealing temperature. The power of S5 (table 5.3), before degraded outdoors, increased by 16.5% from its degraded state, as

shown in fig. 5.11, along with its series resistance. Series resistance is generally caused by the intrinsic resistance of the a-Si cell and all successive contact resistances (e.g., between the metal contact and silicon). Its increase causes a decrease in the module's performance. In sample S5, the series resistance decreased from 0.58 Ω to 0.51 Ω, as shown in fig. 5.11. Also, the shunt resistance is caused by manufacturing defects. A low shunt resistance in a solar cell causes a loss in power by providing an alternate current path. Here, the shunt resistance and the power increased from 42.8 Ω to 64.3 Ω. A different behavior was observed for the flexible thin-film module, sample 3, as shown in Figure 5. Performance at the first measurement point was 1.82 Wp (stabilized value).

After about 553 h at 60 °C, the power increased to 1.93 Wp (±0.8%). This results in an increase of 0.11 Wp (6.2%). During the 65 °C and 70 °C runs, no further change in power was registered. Through stepwise temperature control at different temperatures, it was found that no further parameter changes occurred over a certain period of time. Thus, all weakly bound defects that have healed with this energy level have healed. The short-circuit current, for example, remained nearly constant throughout the experiment. Only the open-circuit voltage and the fill factor have increased with the power.

The above statement about the short-circuit current contradicts the theory that only weakly bound defects (dangling bonds) are healed [61], which are in the material (defect) structure (i.e., a change in the mobility or the lifetime of the charge carriers and thus the photocurrent). If weak bonds, such as dangling bonds, are filled, they change the levels of the band transitions. The fill factor and the power also change.

Figures 5.6, 5.7 and 5.8 show that the influence of temperature due to degradation or annealing is quite strong. Taking a module from a facility at an undefined time during the year will result in an undefined state of the module due to the Stabler-Wronski effect. Then, no power rating determination is possible compared to its value at the time of installation. In the annealing experiment, the a-Si module was subjected to low temperature under illumination [62, 63]. This temperature deviates from the conventional temperature of 160 ° C to reverse light-induced degradation, that is, to contribute to structural change in the material [64]. An overall power change of 3% in the module was obtained after annealing. This change remained stable when the module was at room temperature and did not relax due to long dark storage. In a previous experiment conducted outdoors, it was observed that power recovery was slow in a-Si technology. The annual outdoor annealing cycle shows a similar behavior, leading to a variation in module power between partially degraded (Winter) and partly annealed (Summer) [65].

Interestingly, the amplitude of the pretreatment effect of the S6 module, as shown in section 3.2, became much smaller after annealing. The module S6 experienced a temperature variation of +5 °C during the LS of pretreatment before and after

annealing. The absolute change in P_{MPP} during pretreatment of the degraded module increased for about 2.2 W under illumination, while after annealing, the change during pretreatment was only 0.77 W. A module can vary up to $\pm$ 3% from its mean value at a random amount. Although the pretreatment amplitude was smaller after annealing, the variation of P_{MPP} due to illumination still gave $\pm$0.8% change. As a consequence, the module was still in a phase of not being fully recovered, which acts as an indicator that some metastable behavior affecting the power rating in the a-Si structure might still be present. The full recovery might also never be possible. Therefore, with low-temperature annealing, the metastabilities were reduced, directly impacting the quality of the power rating.

The power rating of a-Si is not easy until a fast and reliable method is formulated for the a-Si family. The device under test is subject to measurement error due to limitations of the accuracy of electronic load measurement and the elevation of temperature, which could lead to a significant error in the electrical parameters (excluding metastable effects). This can deviate the power rating from its original value. Therefore, reliable power rating standards are necessary and find their relevance for the quality assurance of existing PV parks.

Arrhenius Plot of Defect Annealing

Annealing is a thermally driven reaction mechanism that involves discrete particles colliding when subjected to heat. These collisions help disrupt existing bonds and facilitate the formation of new ones. The bond absorbs the energy during the heating and reaches a higher vibrational state. This weakens the bond, allowing it to interact with other reactants and form new bonds.

The reaction process from the reactant to the product corresponds to the stretching or breaking of the bond. The activation energy diagram depends on the thermodynamics of the process, regardless of the reaction path. It depends on thermal activation, which accounts for the distribution of the molecules possessing sufficient kinetic energy to participate in the reaction at a particular temperature. The process of retrieving the initial power of a-Si:H modules through low-temperature annealing demonstrates that the same response can be achieved with different activation energies by following an alternative path.

Arrhenius law for a general parameter X:

$$X = A \exp^{-t/\tau} + y_0, \tag{6.1}$$

where X is a parameter considered to describe the module parameters, that is, V_{OC}, P_{MPP}, or R_{SH}. Using equation (6.1), τ is obtained, the decay time constant, applied in the Arrhenius equation and plotted to obtain the activation energy.

$$1/\tau_{\text{gen}} = k \exp^{-E_a/kT} \tag{6.2}$$

where E_a is the activation energy, k is the Boltzmann constant and T is the temperature.

The results of pretreatment and annealing showed that the increase in V_{OC} amplitude during both experiments was relatively similar, but pretreatment caused reversibility in the dark [66]. The rate of recombination in a-Si:H, causing defect generation, is determined by the light intensity. In these materials, the dangling bonds are associated with the deep levels in the bandgap, which act as trapping or recombination sites. In a-Si:H the structural disorder causes the formation of localized states in the material's bandgap. The localized states trap the charge carriers, reducing the mean free path and thus resulting in loss of mobility. This behaviour is defined by the equation of the carrier mobility:

$$\mu = e\tau/m* \tag{6.3}$$

where μ is the carrier mobility, τ is the scattering time (average time between collisions, e the absolute value of the elementary charge, and m is the effective mass of the free carriers.

The physical process correlated with this activation energy can be described as follows [67], which reports on the $CuInSe_2$/CdS time dependent behaviour of V_{OC} and activation energy energy aligns with the processes in the a-Si:H modules. In a-Si:H, it was found that under illumination, there is a reduction of photoconductivity and an increase in g-factor, g = 2.005, which indicates a paramagnetic defect, confirming that the SW effect is the result of the creation of dangling bonds [68]. The photoconductivity is recovered in 30 min when annealed at 100 °C, but the dangling bond defects can be annealed only at about 180 °C. The instability in the a-Si:H device is due to the formation of dangling bonds [55] in the intrinsic layer or the degradation of the p-i interface [69]. These dangling bonds affect the charge carrier significantly affecting the material electrical performance. It is not fully understood how the healing of the dangling bond occurs in a-Si:H when a deviation from its metastable state (pseudo-equilibrium) occurs. It has been demonstrated that the annealing rate increases when subject to high irradiance and temperature [70].

In the experiment presented here, it was determined that the carrier trapping effects are more pronounced than the metastable structural changes. The results show that the activation energies extracted from the Arrhenius plots are closer to the values associated with trap-assisted recombination processes than those typically linked to structural reordering or hydrogen movement in a-Si:H. Most metastable effects must work in the i-layer or at the interfaces. Electrons and holes generated in the doped layer do not contribute to the output current because of their short lifetime. Defects in the bandgap and midgap states can cause the recombination of charge carriers before they are separated from the external terminals. Tail states (a-Si) cause the

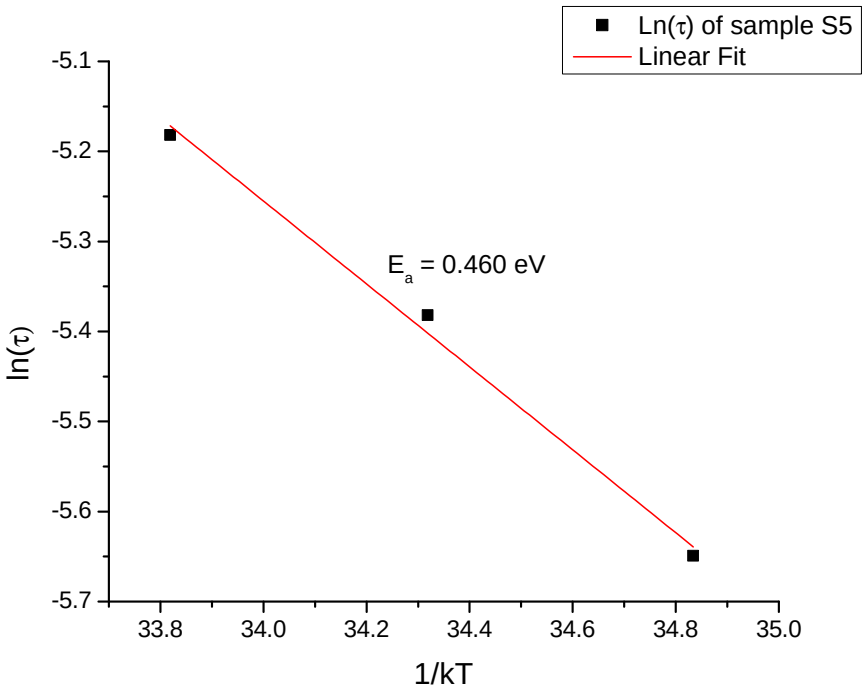

Fig. 6.1: Arrhenius plot of sample S5 annealed at low temperature in the dark.

trapping of the charge carriers, which can release the charge carriers when subjected to a certain amount of energy. Similar behavior was found in a-Si/μSi and CdTe. Defect clusters cause the annihilation or trapping of charge carriers in the CIGS, CdTe, and CZTS types of solar cells.

6.1.4 Power rating

This study highlights the level of uncertainty that can be introduced when performing standard power measurements. The power rating protocol has a lot of ambiguity, as it does not account for metastable effects when handling the modules. This can lead to significant discrepancies during the measurement stage, resulting in numerous erroneous photovoltaic system designs, which can further impact the levelized cost of electricity. Considering the metastable change in electric parameters, the level of degradation, and the module history, a maximum uncertainty in power rating is given. Therefore, it is best to measure the modules immediately after the light-induced stabilization (preconditioning) procedure. It will also be beneficial to perform low irradiance pretreatment to assess module stability and determine the range of response of metastabilities [71].

Furthermore, experience in the field of international comparison campaigns (Round Robins) indicates that the problem of reliably measuring module parameters after more than 12 years remains unsatisfactory, rather than being resolved. The future

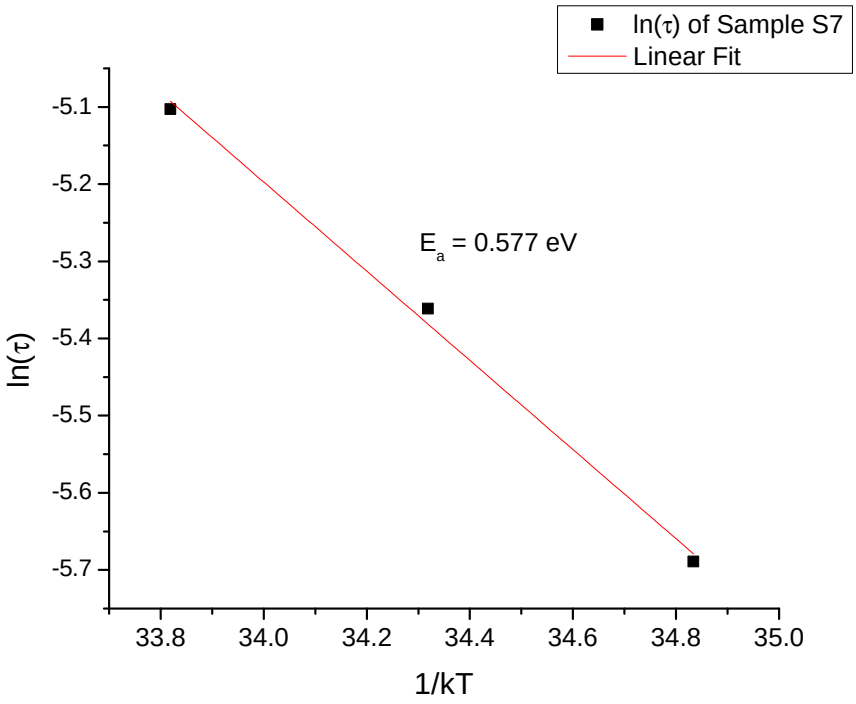

Fig. 6.2: Arrhenius plot of Sample S7 annealed at low temperature in the dark.

of investment in these high-potential technologies depends on the development of reliable international standards for measurement, including accredited testing, quality assurance, and re-powering of PV parks. Detailed studies could further optimize thin-film modules and harmonized power rating procedures.

6.2 CdTe

As shown in section 5.3, even a small change in external parameters, such as light and temperature, can introduce significant variability in the data. The maximum power point of the investigated modules changed with light soaking and the preconditioning procedure. During light soaking of the preconditioned modules, it was observed that the power and voltage were unstable due to light soaking and then relaxed back to their initial state. These intrinsic metastabilities lead to non-stable behavior of the electric parameters of the modules when illuminated before STC power rating, according to IEC 61215-1-5:2015 [72]. In low light, it is easier to observe the influence of metastability on the fill factor, which is primarily influenced by the series and shunt resistances. This generally affects the open-circuit voltage and the maximum output power. The dynamic change makes it tedious to measure the nominal power.

First, this can be interpreted in a way that the modules were not stable (not in their thermodynamic equilibrium), but they are approaching equilibrium. Second, in dark storage: (a) the decrease in the electrical parameters continues, and (b) the values decrease and evolve toward an equilibrium state, considering the initial value in pretreatment.

Neither preconditioning method, with light-induced stabilization or stabilization using bias, correlated in terms of performance measurement. Both methods produce different results. The degraded modules, when brought from the field, showed an improvement in their performance after dark biasing (a new preconditioning method). However, the modules that initially looked stabilized showed further degradation after 30 days of dark soaking. The new method introduced irrecoverable damage to the modules, as seen in table 5.4 in section 5.3. This dark bias-based preconditioning procedure, one of the standard methods of stabilization, should be considered to produce consistent results [18, 73].

The effect seen during the first initial minutes of the pretreatment could be an effect of stored charge in the defect states, which might be introduced by operation in the field or the biasing. The defects are either deep states or located at the interfaces. In the CdTe material, many point defects lie within the material and form many complexes at the interface when the CdS buffer layer is deposited on top of it [74]. Also, the high sheet resistance of the transparent conductive oxide and an increase in shunt formation in the cell material could be some possible causes, resulting in the formation of metastabilities.

When the nondegraded module was compared with the degraded modules, it showed a high amplitude of metastability. However, only in the module with the highest degradation did it exhibit different behavior from the other degraded modules. The direct influence of defects is also shown in [74] and was not measured in the pretreatment work. Furthermore, no information about the type, origin or position of the defect in the degraded modules (e.g., in [73]) could be obtained. Nevertheless, from a macroscopic view of module technology, the correlation holds that an increase in defects due to degradation (also visible in EL) leads to an increase in metastable behavior. Furthermore, an excessively high number of defects leads to a reversal of the metastable effect, as was also found in CIGS technology [42].

First, the increase and then decreasing slope under light soaking seems to indicate two possible processes working simultaneously, the creation and annihilation of metastabilities. Second, this appears to be the case, as the dark relaxation curve leads to a further equilibrium state, which seems to be different from its initial state. The origin might be the formation of metastabilities due to parasitic exposure or treatment by light or bias before pretreatment.

A similar increase in metastable effect was already observed with a decrease in module (or cell) quality for CIGS cells [25], followed by a sudden decrease in

the significance of the effect for extremely high degradation values. This behavior appears to be closely related to defect dependence and will need to be emphasized in future work. Further material characterization at the cell level could give more detailed information about the cause of the metastable effect under low irradiance and different initial conditions.

Since I_{SC} did not change during pretreatment, this is related to the origin of the behavior, specifically the charge carrier effect associated with the number of defects in its most general sense [75]. It is more precisely linked to the location (bulk, buffer, and interface) and the types of defects found in CIGS. Several defects have a charging and discharging nature, which, when subjected to light soaking, provide a channel for the respective charge carriers to annihilate.

This study highlights the uncertainty level that can be introduced when performing standard measurements. Considering the metastable change in the electric parameters, the level of degradation, and the history of the module gives the maximum uncertainty of the power rating. Therefore, it will be best to measure the modules immediately after the light-induced stabilisation (preconditioning) procedure [76]. It will also be beneficial to perform low-light pretreatment to assess module stability and determine the range of response of metastabilities [77].

The experimental work presented here on indoor and outdoor operated CdTe modules shows how low-light conditions can considerably influence the power rating of modules over a short time interval [42, 78]. This can lead to a significant discrepancy in determining energy yield. Additionally, the dark bias-based stabilization procedure proved inadequate as a replacement for the light-based stabilization method. This calls for a stabilization procedure to rule out the metastable effect, which can produce repeatable and reliable performance parameters as modules will see outdoors.

Considering the metastable change in electric parameters, the level of degradation, and the module history gives a maximum uncertainty of power rating. Furthermore, experience in international comparison campaigns (Round Robins) shows that the problem of reliably measuring module parameters remains unsatisfactory, even after more than 12 years. The future of investment in these high-potential technologies depends on the development of reliable international standards for measurement, including accredited testing, quality assurance, and repowering of PV parks.

6.3 CZTSSe and CIGSSe comparison

In the CZTSSe and the CIGSSe devices, low-formation energy defects exist deep within the bandgap. Still, they may not have any detrimental effect due to the defect complexes [15]. One of the most common metastable changes in CIGS and CdTe is a change in V_{OC} and fill factor during light soaking or reverse biasing of the

junction [74]. The 'red light soaking' effect contributes to the increase in open circuit voltage and capacitance, since it increases the net acceptor concentration in the absorber [26]. The 'blue light soaking' process decreases the junction capacitance as it interacts with the CdS layer, thereby reducing the net acceptor density in the absorber. It shows that the proximity of the heterojunction mainly contributes to the significant change in metastability of the power with light soaking.

This similar decreasing trend under blue- and white-light conditions indicates that the majority of the metastabilities might originate from the blue-light component. Because blue light contributes to absorbance in the buffer, red light is absorbed mainly by the absorber of the CZTSSe device. When the negative slope under white light is compared with the slope under blue light, it can indicate the defects that are more prevalent at the heterojunction, causing these transient metastabilities. Therefore, it is crucial to consider light-induced metastability before initiating the measurement routine of the cell and modules to ensure a reliable power rating.

The kesterite CZTSSe is a suitable alternative for replacing CIGS-based PV devices [79]. A series of measurements were performed under color-filtered light conditions to observe the temporal stability of monograin CZTSSe cells. These measurements help reveal the location of the defects in relation to the change in electrical state of the heterojunction or cell interfaces [80].

In contrast to CIGS and CdTe, the CZTSSe mini-module exhibits well-defined logarithmic behavior in both time domains. Two time domains suggest a minimum of two mechanisms of different time scales and activation energies [81].

The copper vacancy (V_{Cu}) has a low formation energy of 0.024 eV, and the indium vacancy has multiple formation energies of 0.165, 0.4, and 0.659 eV. Many other defects can be found in CIGS, including (Cu over In), (In over Cu), copper interstitials, and the pair of (In over Cu) and copper vacancies. The information on the performance parameters of the cells depends on their V_{OC} and FF [42].

6.3.1 Impedance Spectroscopy

Each cell of CZTSSe and CIGS technology showed similar impedance spectra. It is a suitable method for determining the defect levels [82]. However, degraded or poor quality samples show a lower value in shunt resistance [83].

Cell 2x shows that the carrier density (N_a) was highest (1.01×10^{15} cm^{-3}), implying higher doping compared to cell 1x and 3x (7.26×10^{14} and 6.50×10^{14} cm^{-3}, respectively). Cells 1x and 3x exhibit higher metastabilities, as indicated by higher V_{OC} and P_{MPP} degradation under light soaking, and lower R_s and R_{sh} values. The high ideality factor ($n_2 = 3.59$) and the large recombination current J_{02} (2.14×10^{-6} A/cm^2) indicate complex recombination dynamics, which can suggest a shorter carrier life of the minority. Cell 2x also had the lowest area-normalized series resistance

(3.21 Ωcm^2) and highest shunt resistance (5.33 kΩ), suggesting good contacts and a junction with only modest performance losses as compared to the samples 1x and 3x.

Dopants are classified as donors or acceptors; donors donate an electron to the conduction band, whereas acceptors accept an electron from the valence band [84]. Deep traps generally act as recombination or generation centers and are not classified as donor or acceptor levels, a hallmark of Shockley–Read–Hall (SRH) recombination mechanisms. The effectiveness of a deep trap in facilitating these processes depends on several factors:

1. Whether the interaction involves **carrier capture** or **emission**;
2. The **ionization energy** of the trap level;
3. The **charge state** of the trap—neutral, positively, or negatively charged;
4. Its **spatial location**—embedded in the bulk material or positioned at an interface.

Several studies have been conducted on the capacitance spectroscopy of CZTS, and an asymmetric PL band at 1.3 eV has been reported in numerous studies [85, 86, 87, 88, 89, 90]. This is related to the presence of some shallow defect of <30 meV. The second diode had a higher amplitude than the first diode, as shown in figures 5.24 and 5.25. This highlights the more significant influence of the recombination mechanism, or, in other words, SRH recombination [58, 91]. The Nyquist plot of all cells has been shown to be semicircular, a signature of RC-like behavior. However, for CIGS cells the impedance at the different biases was superimposed and crossed with each other, suggesting bias-dependent metastable behavior.

Generally, the C-–f curves of a thin-film solar cell show a low-frequency capacitance C_{LF} to a high-frequency capacitance C_{HF} decay. It can be interpreted as the most straightforward case consisting of a single time constant t_0 and an activation energy E_A of t_0. Several phenomena can lead to such a simple mechanism, including one single deep trap level, an energy barrier at a contact, dielectric relaxation in a bulk layer, and interface states [92]. The diode conductance can be used to identify traps [93]. C–f measurements in an equilibrium state (zero bias) can help determine the trap densities, and performing them at different temperatures can help determine trap energy levels. The dielectric relaxation frequency refers to the relaxation response of the oscillating frequency [59]. The dielectric polarization at high frequency is related to the geometric capacitance of the material, while the dielectric relaxation is related to the frequency-dependent polarization. The complex dielectric constant varies from low-frequency to high-frequency (geometric) values.

Chapter 7

CONCLUSION

The thesis concludes that metastabilities affect various thin-film photovoltaic technologies. The research has revealed that all of the technologies studied exhibit a short-term metastable effect that is reversible in the dark. Although the time constant of the decrement of persistent photoconductivity varies for each technology, it declines back to its initial starting value in every technology.

The main specific findings of the thesis are summarized for an overview:

1. For the investigated materials, it could be shown that the metastabilities were formed under illumination of white light or different monochromatic colors. The metastabilities lead to changes in the electrical parameters of illuminated solar devices. These were voltage, current, fill-factor and power. All changes followed saturation dynamics while the sample was illuminated and were reversible in the dark.
2. For all samples, it was found that the working point along the diode I–V curve has a significant impact on the formation of metastabilities and the changes of the electrical parameters by metastabilities. The metastable amplitude was significantly lowered by shifting the operation point from open-circuit to short-circuit.
3. In general, all experiments showed, independently of the cell materials, a clear separation of metastable effects from kinematic or dynamic effects like degradation. It was observed that different operating regimes of order parameters, such as temperature and illumination, separate these effects. For some samples, these regimes overlapped or additional driving mechanisms were operational, e.g., for a particular combination of material class and wavelength of the light, or very high amounts of volumetric defects.
4. Amorphous silicon (a-Si:H) exhibits the well-known Staebler-Wronski effect on a longer time scale, with evidence showing that power recovery is possible through low-temperature annealing. Power rating is explicitly affected by exposure to light and changes in temperature. Measuring a module in a stable state under low-light illumination might be impossible without proper treatment. The illumination at low light levels alters the measured power values for $\pm 2.8\%$ at a variable temperature and $\pm 0.42\%$ at a stable temperature in a-Si module, and $\pm 3.29\%$ in a micromorph module at a variable temperature. The

findings align well with the literature, stating that weak-bonded defects with binding energies smaller than 200 meV are a reason for the metastabilities.

5. Cadmium telluride (CdTe) shows a clear correlation between metastability amplitude and degradation level, ranging from 4.62% to 22.11%, reinforcing the need for optimized preconditioning strategies. For moderately degraded modules, P_{MPP} initially increased by up to 3.5%, followed by a subsequent decline with prolonged illumination. For higher levels of degradation exceeding 22%, the metastable effect breaks down, most likely due to the high density of defects.

6. Copper-zinc-tin-sulfide-selenide (CZTSSe) displays a complex metastable behavior similar to CIGS devices. The devices show clear wavelength-dependent degradation. In cell 2x, P_{MPP} decreased by up to 9% and V_{OC} dropped by 3.9% under white light soaking. Spectral dependence played a key role: while blue (450 nm) light resulted in -3.67% V_{OC}, red (650 nm) light initially enhanced V_{OC} by +0.7%, followed by a decline. The mini-modules exhibited performance degradation under all colored lights, with blue light causing the most significant degradation (up to -7.33% in power). Due to secondary phase formation and charge trapping, impacting voltage and current stability, metastability formation is present even at room temperature. The studied effects were reversible: the STC cell measurements before and after light soaking experiments, when subsequently dark stored, showed matching results.

7. Impedance spectroscopy gave insight about the similar defect behavior in CZTSSe and CIGS cells, with degraded samples exhibiting lower shunt resistance. Deep traps, central to SRH recombination, vary by energy, charge, and location. Metastable effects in CIGS cause overlapping impedance curves at different biases.

The insights gained from this study are valuable to manufacturers, testing laboratories, and solar farm operators. Accurate initial measurements under STC conditions not only verify product claims but also form the foundation for future performance monitoring and degradation analysis. Moreover, the study should lead to a more and deeper analysis of metastable effects also for future photovoltaic material or devices, such as perovskite and perovskite-silicon tandem devices.

Bibliography

[1] IRENA. *Renewable Capacity Statistics 2016*. Tech. rep. International Renewable Energy Agency, 2016 (cit. on p. 1).

[2] Solar Power Europe. *Global Market Outlook (GMO) 2019–2023*. Tech. rep. Solar Power Europe, 2019 (cit. on p. 1).

[3] GTM Research. *Global Solar Demand Monitor*. Tech. rep. GTM Research, 2017 (cit. on p. 1).

[4] M. L. Garcia and O. H. Bray. *Fundamentals of Technology Roadmapping*. Tech. rep. Strategic Business Development Department, Sandia National Laboratories, 1997 (cit. on p. 3).

[5] C. T. Sah, R. N. Noyce, and W. Shockley. „Carrier Generation and Recombination in P-N Junctions and P-N Junction Characteristics“. In: *Proceedings of the IRE* 45 (1957), pp. 1228–1243 (cit. on pp. 14, 19).

[6] PVEducation. *Shunt Resistance | PVEducation*. Available online at: `https://www.pveducation.org/` (cit. on p. 15).

[7] PVEducation. *Quantum Efficiency | PVEducation*. Available online at: `https://www.pveducation.org/` (cit. on p. 15).

[8] Wikipedia. *Monochromator*. `http://en.wikipedia.org/wiki/Monochromator`. [Online; accessed 02-June-2015]. 2015 (cit. on p. 15).

[9] W. Shockley. „The Theory of p-n Junctions in Semiconductors and p-n Junction Transistors“. In: *Bell Systems Technical Journal* 28 (1949), p. 435 (cit. on p. 17).

[10] M. Green. *Solar Cells: Operating Principles, Technology and System Applications*. UNSW, Sydney, Australia, 1998 (cit. on p. 19).

[11] W. Shockley. „The Theory of p-n Junctions in Semiconductors and p-n Junction Transistors“. In: *Bell Systems Technical Journal* 28 (1949), p. 435 (cit. on p. 19).

[12] B. G. Streetman and S. Banerjee. *Solid State Electronic Devices, Chapter 5.6.2: "Recombination and Generation in the Transition Region"*. Prentice Hall, 2000 (cit. on pp. 19, 21).

[13] O. Breitenstein. „Nondestructive Local Analysis of Current-Voltage Characteristics of Solar Cells by Lock-in Thermography“. In: *Solar Energy Materials and Solar Cells* 95 (2011), pp. 2933–2936 (cit. on p. 19).

[14] IEC 61646. *Thin-film Terrestrial Photovoltaic (PV) Modules – Design Qualification and Type Approval*. 2008 (cit. on p. 19).

[15] A. Niemegeers and M. Burgelman. „Effects of the Au/CdTe Back Contact on Characteristics of Au/CdTe/CdS/TCO Solar Cells“. In: *Journal of Applied Physics* 81 (1997), pp. 2881–2886 (cit. on pp. 22, 114).

[16] H. Bayhan and A. S. Kavasoğlu. „Admittance and Impedance Spectroscopy on Cu(In,Ga)Se_2 Solar Cells“. In: *Turkish Journal of Physics* 27 (2003), pp. 529–535 (cit. on p. 22).

[17]William Shockley and Hans J. Queisser. „Detailed Balance Limit of Efficiency of p-n Junction Solar Cells“. In: *Journal of Applied Physics* 32 (1961), pp. 510–519 (cit. on p. 22).

[18]National Renewable Energy Laboratory. *Cadmium Telluride Solar Cells*. Available at: `https://www.nrel.gov/pv/cadmium-telluride-solar-cells.html` (cit. on pp. 31, 48, 113).

[19]S. M. Sze. *Physics of Semiconductor Devices*. 2nd. John Wiley & Sons Inc., New York, 1981 (cit. on p. 31).

[20]K. L. Chopra and S. R. Das. *Thin Film Solar Cells*. Plenum Press, New York, 1983 (cit. on p. 31).

[21]K. Weiss et al. „Light-soaking and Power Measurements of Thin Film Modules“. In: *Proceedings of the SPIE*. Vol. 7409. 2009 (cit. on pp. 31, 105).

[22]J. Kuurne et al. „Sweep Time, Spectral Mismatch and Light Soaking in Thin Film Module Measurement“. In: *33rd IEEE PVSEC*. 2008 (cit. on pp. 31, 105).

[23]J. A. del Cueto and B. von Roedern. „Long-term Transient and Metastable Effects in Cadmium Telluride Photovoltaic Modules“. In: *Progress in Photovoltaics: Research and Applications* 14 (2006), pp. 615–628 (cit. on p. 32).

[24]A. Mittal and M. Rennhofer. „Influence of Degradation on the Power Rating of the CdTe Modules“. In: *PV Symposium*. Staffelstein, Germany, 2016 (cit. on p. 32).

[25]S. Novalin, M. Rennhofer, and J. Summhammer. „Electrical metastabilities in chalcogenide photovoltaic devices,“ in: *Thin Solid Films, TSF- 31112, 535; S. 261 - 264* (2013) (cit. on pp. 32, 82, 113).

[26]G. Friesen, R. Gottschalg, and H. G. Beyer et al. „Results of the 3rd Modelling Round Robin within the European Project 'PERFORMANCE'—Comparison of Module Energy Rating Methods“. In: *Proceedings of the 22nd European Photovoltaic Solar Energy Conference and Exhibition*. Milan, Italy, 2007, pp. 2659–2663 (cit. on pp. 32, 115).

[27]J. A. del Cueto, C. A. Deline, D. S. Albin, S. R. Rummel, and A. Anderberg. „Striving for a Standard Protocol for Preconditioning or Stabilization of Polycrystalline Thin Film Photovoltaic Modules“. In: *Proceedings of the SPIE 2009 Solar Energy + Technology Conference*. San Diego, California: National Renewable Energy Laboratory (NREL), 2009 (cit. on pp. 34, 106).

[28]Dirk C. Jordan and Sarah R. Kurtz. *Photovoltaic Degradation Rates—An Analytical Review*. Tech. rep. National Renewable Energy Laboratory (NREL), 2012 (cit. on p. 34).

[29]Q. Guo, G. M. Ford, W.-C. Yang, et al. „Fabrication of 7.2% Efficient CZTSSe Solar Cells Using CZTS Nanocrystals“. In: *Journal of the American Chemical Society* 132 (2010), pp. 17384–17386 (cit. on p. 34).

[30]K. Wang, O. Gunawan, T. Todorov, et al. „Thermally Evaporated Cu_2ZnSnS_4 Solar Cells“. In: *Applied Physics Letters* 97 (2010), p. 143508 (cit. on p. 34).

[31]A. Willoughby. *Solar Cell Materials: Developing Technologies*. Wiley Series in Materials for Electronic & Optoelectronic Applications. Wiley, Chichester, 2014, p. 186 (cit. on p. 34).

[32]I. D. Olekseyuk, L. D. Gulay, I. V. Dydchak, et al. „Single Crystal Preparation and Crystal Structure of the $Cu_2Zn/(Cd,Hg)/SnSe_4$ Compounds“. In: *Journal of Alloys and Compounds* 340 (2002), pp. 141–145 (cit. on p. 34).

[33]I. Repins, C. Beall, N. Vora, et al. „Co-evaporated $Cu_2ZnSnSe_4$ Films and Devices“. In: *Solar Energy Materials and Solar Cells* 101 (2012), pp. 154–159 (cit. on p. 34).

[34]International Organization for Standardization. *Guide to the Expression of Uncertainty in Measurement*. ISO: Geneva, ISBN 92-67-10199-9. 1993 (cit. on p. 39).

[35]B. N. Taylor and C. E. Kuyatt. *Guidelines for Evaluating and Expressing the Uncertainty of NIST Measurement Results*. Tech. rep. Gaithersburg, MD: National Institute of Standards and Technology, Technical Note 1297, 1994 (cit. on p. 39).

[36]D. L. King, J. A. Kratochvil, W. E. Boyson, and W. Bower. „Field Experience with a New Performance Characterization Procedure for Photovoltaic Arrays“. In: *Proceedings of the 2nd World Conference and Exhibition on Photovoltaic Solar Energy Conversion*. Vienna, Austria, 1998 (cit. on p. 41).

[37]D. L. King, J. A. Kratochvil, and W. E. Boyson. „Temperature Coefficients for PV Modules and Arrays: Measurement Methods, Difficulties, and Results“. In: *26th IEEE Photovoltaic Specialists Conference*. Anaheim, CA, 1997, pp. 1183–1186 (cit. on p. 41).

[38]H. Field. „Solar Cell Spectral Response Measurement Errors Related to Spectral Band Width and Chopped Light Waveform“. In: *Proc. 26th IEEE Photovoltaic Specialists Conference*. Anaheim, 1997, p. 471 (cit. on p. 42).

[39]S. Novalin, M. Rennhofer, and J. Summhammer. „Electrical Metastabilities in Chalcogenide Photovoltaic Devices“. In: *Thin Solid Films* 535 (2013), pp. 261–264 (cit. on p. 48).

[40]J. A. del Cueto and B. von Roedern. „Long-Term Transient and Metastable Effects in Cadmium Telluride Photovoltaic Modules“. In: *Progress in Photovoltaics: Research and Applications* 14 (2006), pp. 615–628 (cit. on pp. 48, 106).

[41]IEC 60891. *Photovoltaic Devices – Procedures for Temperature and Irradiance Corrections to Measured I-V Characteristics*. 2009 (cit. on p. 48).

[42]D. Menz. „Light Soaking of Thin-Film Solar Cells under Colored Light“. MA thesis. Technische Universität Wien, 2015 (cit. on pp. 82, 94, 113–115).

[43]N. H. Reich and R. W. Lof. „Weak Light Performance and Spectral Response of Different Solar Cell Types“. In: *Proceedings of the 20th European Photovoltaic Solar Energy Conference (EUPVSEC)*. 2005 (cit. on p. 105).

[44]M. Rennhofer, S. Zamini, K. Berger, et al. „Thin Film PV-Module Performance Under Varying Weather Conditions“. In: *6th User Forum - Thin Film Photovoltaics, International Conference*. OTTI, 2010, pp. 120–126 (cit. on p. 105).

[45]D. E. Carlson and C. R. Wronski. „Amorphous Silicon Solar Cell“. In: *Applied Physics Letters* 28 (1976), pp. 671–673 (cit. on p. 105).

[46]D. E. Carlson. „Amorphous Silicon Solar Cells“. In: *IEEE Transactions on Electron Devices* 24 (1977), pp. 449–453 (cit. on p. 105).

[47]G. Friesen, R. Gottschalg, and H. G. Beyer et al. „Results of the 3rd Modelling Round Robin within the European Project 'PERFORMANCE'—Comparison of Module Energy Rating Methods". In: *Proceedings of the 22nd European Photovoltaic Solar Energy Conference and Exhibition*. Vol. 22. Italy, 2007, pp. 2659–2663 (cit. on p. 105).

[48]W. E. Spear and P. G. LeComber. „Substitutional Doping of Amorphous Silicon". In: *Solid State Communications* 17.9 (1975), pp. 1193–1196 (cit. on p. 106).

[49]M. Rennhofer, K. Berger, R. Leidl, et al. „Photometric Evaluation of Photovoltaic Thin-Film Shading Elements". In: *Proceedings of the 27th European PVSEC and Exhibition*. Frankfurt, Germany, 2012, pp. 4220–4223 (cit. on p. 106).

[50]D. Craciun, V. Helmbrecht, S. Tselepis, et al. *Harmonised Procedures on Photovoltaic Modules Long-Term Energy Yield Measurements and Performance Evaluation under Outdoor Conditions*. 2012 (cit. on p. 106).

[51]I. Konovalov, V. Strikha, and O. Breitenstein. „Activation Energy of Local Currents in Solar Cells Measured by Thermal Methods". In: *Progress in Photovoltaics: Research and Applications* 6 (1998), pp. 151–161 (cit. on p. 106).

[52]Stefan Krauter and Alexander Priess. „Weak Light Performance Analysis". In: *Proceedings of the 25th PVSEC*. Valencia, Spain, 2011, p. 3141 (cit. on p. 106).

[53]Vincent Helmbrecht and Diana Cracium et al. „PV Tech Analysis Report". In: *PVTech.org* (2011), pp. 194–201 (cit. on p. 106).

[54]S. B. Zhang and Howard M. Branz. „Nonradiative Electron-Hole Recombination by a Low-Barrier Pathway in Hydrogenated Silicon Semiconductors". In: *Physical Review Letters* 84 (2000), p. 967 (cit. on p. 106).

[55]Howard M. Branz. „Hydrogen Collision Model: Quantitative Description of Metastability in Amorphous Silicon". In: *Physical Review B* 59 (1999), p. 5498 (cit. on pp. 106, 110).

[56]S. Janski et al. „Spectral Photocurrent Measurement Techniques for Thin Film Modules". In: *Proc. 19th European Photovoltaic Solar Energy Conference and Exhibition*. Paris, 2004, pp. 1595–1596 (cit. on p. 106).

[57]P. Grunow et al. „Weak Light Performance and Annual Energy Yields of PV Modules and Systems as a Result of the Basic Parameter Set of Industrial Solar Cells". In: *Proc. 19th European Photovoltaic Solar Energy Conference and Exhibition*. Paris, 2004, pp. 2190–2193 (cit. on p. 106).

[58]P. Zabierowski, U. Rau, and M. Igalson. „Classification of Metastabilities in the Electrical Characteristics of ZnO/CdS/Cu(In,Ga)Se_2 Solar Cells". In: *Thin Solid Films* 387 (2001), pp. 147–150 (cit. on pp. 106, 116).

[59]Th. Meyer, F. Engelhardt, J. Parisi, and U. Rau. „A Model for the Open Circuit Voltage Relaxation in Cu(In,Ga)Se_2 Heterojunction Solar Cells". In: *European Physical Journal: Applied Physics* 8.1 (1999), pp. 43–52 (cit. on pp. 106, 116).

[60]K. Schroder. *Semiconductor Material and Device Characterization*. John Wiley, 1998 (cit. on p. 106).

[61]P. K. Lim, W. K. Tam, L. F. Yeung, and F. M. Lam. „Effect of Hydrogen on Dangling Bond in a-Si Thin Film". In: *Journal of Physics: Conference Series* 61 (2007), pp. 708–712 (cit. on p. 108).

[62]A. O. Kodolbaş and A. Eray et al. „Thin Film Materials and Devices Development in Science and Technology“. In: *Proceedings of the 10th International School on Condensed Matter Physics*. Varna, 1999, pp. 445–448 (cit. on p. 108).

[63]N. Wyrsch, F. Finger, T. J. McMahon, and M. Vanecek. „How to Reach a More Precise Interpretation of Subgap Absorption Spectra in Terms of Deep Defect Density in a-Si:H“. In: *Journal of Non-Crystalline Solids* 137–138 (1991), p. 347 (cit. on p. 108).

[64]D. E. Carlson and C. R. Wronski. „Amorphous Silicon Solar Cell“. In: *Applied Physics Letters* 31.4 (1977), pp. 292–294 (cit. on p. 108).

[65]T. R. Betts, J. Roy, R. Gottschalg, Mau, et al. „Validation of Proposed Photovoltaic Energy Rating Standard and Sensitivity to Environmental Parameters“. In: *Proceedings of the 23rd European Photovoltaic Solar Energy Conference*. Valencia, Spain, 2008, pp. 2728–2734 (cit. on p. 108).

[66]R. Ruther, J. del Cueto, and G. Tamizh-Mani et al. „Overview from the Field: PV Module Performance“. In: *33rd IEEE Photovoltaic Specialists Conference (PVSEC)*. 2008, pp. 1–5 (cit. on p. 110).

[67]Mark N. Ruberto and Allen Rothwarf. „Time-dependent Open-circuit Voltage in $CuInSe_2$/CdS Solar Cells: Theory and Experiment“. In: *Journal of Applied Physics* 61 (1987), pp. 4662–4669 (cit. on p. 110).

[68]H. Dersch, J. Stuke, and J. Beichler. „Electron Spin Resonance of Doped Glow-Discharge Amorphous Silicon“. In: *Physica Status Solidi (b)* 105.1 (1981), pp. 129–138 (cit. on p. 110).

[69]D. E. Carlson. „Amorphous Silicon Solar Cells“. In: *IEEE Transactions on Electron Devices* 24 (1977), pp. 449–453 (cit. on p. 110).

[70]T. Minemoto, T. Matsui, and H. Takakura et al. „Theoretical Analysis of the Effect of Conduction Band Offset of Windows/CIS Layers on Performance of CIS Solar Cells Using Device Simulation“. In: *Solar Energy Materials and Solar Cells* 67 (2001), pp. 83–88 (cit. on p. 110).

[71]Y. Tawada, K. Tsuge, M. Kondo, H. Okamoto, and Y. Hamakawa. „Properties and Structure of a-SiC:H for High-efficiency a-Si Solar Cells“. In: *Journal of Applied Physics* 53 (1982), p. 5273 (cit. on p. 111).

[72]IEC 61215-1-3. *Design Qualification and Type Approval: Part 1-3 for a-Si and micro c-Si Photovoltaic Modules* (cit. on p. 112).

[73]D. Menz. „Light Soaking of Thin-Film Solar Cells under Colored Light“. MA thesis. Technische Universität Wien, 2015 (cit. on p. 113).

[74]C. S. Ferekides, D. Marinskiy, and Viswanathan et al. „High-efficiency CSS CdTe Solar Cells“. In: *Thin Solid Films* 361–362 (2000), pp. 520–526 (cit. on pp. 113, 115).

[75]S. Siebentritt, M. Igalson, C. Persson, and S. Lany. „The Electronic Structure of Chalcopyrites: Bands, Point Defects and Grain Boundaries“. In: *Progress in Photovoltaics: Research and Applications* 18.6 (2010), pp. 390–410 (cit. on p. 114).

[76]C. T. Sah. „The Equivalent Circuit Model in Solid-State Electronics; Part I: The Single Energy Level Defect Centres“. In: *Proc. IEEE* 55 (1967), pp. 654–659 (cit. on p. 114).

[77]C. T. Sah. „The Equivalent Circuit Model in Solid-State Electronics—III: Conduction and Displacement Currents“. In: *Proc. IEEE* 55 (1970). Also published in Solid-State Electron. 13, 1547–1575, p. 672 (cit. on p. 114).

[78]T.R. Betts, J. Roy, R. Gottschalg, and Mau et al. „Validation of Proposed Photovoltaic Energy Rating standard and sensitivity to environmental parameters“. In: *Proc. of 23nd European Photovoltaic Solar Energy Conference, Valencia, pp. 2728-2734, Spain* (2008) (cit. on p. 114).

[79]Robert P. Kenny, Miglena Nikolaeva-Dimitrova, and Ewan D. Dunlop. „Performance Measurements of CIS Modules: Outdoor and Pulsed Simulator Comparison for Power and Energy Rating“. In: *IEEE Conference Proceedings*. 2006, pp. 2058–2061 (cit. on p. 115).

[80]R. A. Sasala and J. R. Sites. „Time Dependent Voltage in $CuInSe_2$ and CdTe Solar Cells“. In: *IEEE Proceedings*. 1993, pp. 543–548 (cit. on p. 115).

[81]A. Abelenda et al. „Anomalous Persistent Photoconductivity in Cu_2ZnSnS_4 Thin Films and Solar Cells“. In: *Solar Energy Materials and Solar Cells* 137 (2015), pp. 164–168 (cit. on p. 115).

[82]D. L. Losee. „Admittance Spectroscopy of Impurity Levels in Schottky Barriers“. In: *Journal of Applied Physics* 46 (1975), pp. 2204–2214 (cit. on p. 115).

[83]M. Munoz, E. Vera-López, J. A. Gómez-Cuaspud, and Y. Pineda-Triana. „Synthesis and Characterization by Solid-State Impedance Spectroscopy of Semiconductor Cu2ZnSnS4 Material for Photovoltaic Technologies“. In: *Journal of Physics: Conference Series* 786.1 (2017), p. 012028 (cit. on p. 115).

[84]Erkki Kask. *Study of Kesterite Solar Cell Absorbers by Capacitance Spectroscopy Methods*. Master's Thesis, Tallinn University of Technology. 2016 (cit. on p. 116).

[85]K. Tanaka, Y. Miyamoto, H. Uchiki, K. Nakazawa, and H. Araki. „Donor-Acceptor Pair Recombination Luminescence from Cu_2ZnSnS_4 Bulk Single Crystals“. In: *physica status solidi (a)* 203 (2006), pp. 2891–2896 (cit. on p. 116).

[86]K. Hoenes, E. Zscherpel, J. Scragg, and S. Siebentritt. „Shallow Defects in Cu_2ZnSnS_4“. In: *Physica B: Condensed Matter* 404 (2009), pp. 4949–4952 (cit. on p. 116).

[87]K. Oishi, G. Saito, K. Ebina, et al. „Growth of Cu_2ZnSnS_4 Thin Films on Si (100) Substrates by Multisource Evaporation“. In: *Thin Solid Films* 517 (2008), pp. 1449–1452 (cit. on p. 116).

[88]M. Grossberg, J. Krustok, J. Raudoja, et al. „Photoluminescence and Raman Study of $Cu_2ZnSn(Se_xS_{1-x})_4$ Monograins for Photovoltaic Applications“. In: *Thin Solid Films* 519.21 (2011), pp. 7403–7406 (cit. on p. 116).

[89]E. Mellikov and M. Altosaar et al. „Research in Solar Cell Technologies at Tallinn University of Technology“. In: *Thin Solid Films* 516 (2008), pp. 7125–7134 (cit. on p. 116).

[90]M. Altosaar, J. Raudoja, K. Timmo, et al. „$Cu_2Zn_{1-x}Cd_xSn(Se_{1-y}S_y)_4$ Solid Solutions as Absorber Materials for Solar Cells“. In: *physica status solidi (a)* 205 (2008), pp. 167–170 (cit. on p. 116).

[91]I. A. Ezenewa. „Synthesis and Optical Characterization of Zinc Oxide Thin Film“. In: *Research Journal of Chemical Sciences* 2.3 (2012), pp. 26–30 (cit. on p. 116).

[92]Th. Meyer, F. Engelhardt, J. Parisi, and U. Rau. „Spectral Dependence and Hall Effect of Persistent Photoconductivity in Polycrystalline Cu(In,Ga)Se_2 Thin Films“. In: *Journal of Applied Physics* 91 (2002) (cit. on p. 116).

[93]Selma M. H. Al-Jawad, Ali M. Mousa, and Wessal Aead Taha. „Investigation of Optical Properties of Cadmium Sulfide (CdS) Thin Films by Chemical Bath Deposition“. In: *Um-Salama Science Journal* 6.1 (2009), pp. 150–162 (cit. on p. 116).